Biointerfacing Polymers to Overcome Challenges in Vaccine Delivery, Gene Therapy, and Cancer Therapy

A DISSERTATION SUBMITTED TO THE FACULTY OF THE
UNIVERSITY OF MINNESOTA
BY

Samuel M. Hanson

IN PARTIAL FULFILLMENT OF THE REQUIREMENTS
FOR THE DEGREE OF
DOCTOR OF PHILOSOPHY

Advisor: Chun Wang, Ph.D.

March 2021

Acknowledgements

This work was funded by the Minnesota Partnership for Biotechnology and Medical Genomics and the Boston Scientific Corporation. Parts of this work were carried out in the Characterization Facility, University of Minnesota, which receives partial support from NSF through the MRSEC program. First and foremost, I would like to thank my advisor Dr. Chun Wang for his attention, advice, and guidance throughout this journey. From my first day, where I was so nervous that I could barely use the balance, until now, it has been an honor to work in the Wang Lab. I would also like to give special thanks to Dr. Ron Siegel, Dr. Wei Shen, and Dr. Raj Suryanarayanan for their guidance and participation on my thesis committee.

This work was completed with the help of many people. I would like to thank Dr. Michael Barry, Dr. Shailbala Singh, and Dr. Jagannadha Sastry for their collaboration and completion of the in vivo mouse study for the sublingual vaccine project. Thank you to Dr. Paul Grosso, Dr. Heidi Schwanz, Evan Bennet, Jasmin Flowers, and especially Dr. Bruce Forsyth for their support and helpful discussion about embolic microspheres and irreversible electroporation. I thank Dr. Paul Iazzio for providing porcine sublingual tissue and Dr. John Bischof for providing AsPC-1 cells. I would also like to thank Dr. Brenda Ogle, Dr. Victor Barocas, Dr. David Odde, Dr. Wei Shen, and Dr. Bob Tranquillo for allowing me to use various pieces of their equipment to complete this work. Thank you to Allison Siehr for her technical assistance and thoughtful discussion. A very special thank you to my fellow lab mates both past and present, including Dr. Sudipta Panja, Dr. Kevin Ortiz-Rivera, Anthony Tabet, Marcus Flowers, and Tvisha Shah. I would also like to thank all the undergraduate researchers in the Wang Lab, without whom much of this

work would not have been possible. Special thanks to Leah Novik, Nathan Roberts, and Noah Nathan for all their hard work.

A very special thank you to my parents, Mike and Amy, as well as my sister, Maddie, for their encouragement throughout this journey. Finally, I would like to thank my partner, Audrey Hanson. Thank you for your love, patience, and support.

Abstract

Polymers can be designed to interface with biological entities, including biological molecules, cells, and tissues, and to modulate their properties and behaviors. In this dissertation, biointerfacing polymers were used to overcome four key challenges in vaccine delivery, gene therapy, and cancer therapy. First, mucoadhesive wafers composed of binary polymer blends of carboxymethylcellulose and alginate were developed to preserve the activity and improve the sublingual delivery of protein vaccines. Second, polymer wafers composed of polyvinyl alcohol were developed to enhance polyplex-mediated gene transfection in vitro in the presence of serum. Third, a synthetic membranolytic polymer poly(6-amino-1-hexyl methacrylate) (PAHM) was used to disrupt cancer cell membrane, resulting in increased cellular uptake of doxorubicin and synergistic killing of cancer cells. Finally, PAHM was used to sensitize cancer cells to irreversible electroporation (IRE), leading to enhanced killing at electric field strengths lower than IRE alone. These studies have laid the foundation for future development of new and transformative medical technologies.

Table of Contents

List of Tables

List of Figures

Chapter 1 Introduction

The first chapter of this thesis aims to provide a general background of polymer-based drug delivery and to identify four challenges we will be addressing: (1) instability and insufficient mucosal permeation of sublingual protein vaccines; (2) inadequate transfection efficiency of polyplex-mediated gene delivery in the presence of serum; (3) cancer cell resistance to chemotherapy drugs; (4) inability of irreversible electroporation (IRE) to ablate large tumors.

Another purpose of this chapter is to introduce the concept of "biointerfacing" polymers as a unifying theme to how we will overcome these challenges. We define biointerfacing polymers as materials that, due to their physicochemical properties, can interface with biological materials, including biomolecules (e.g., proteins, nucleic acids), cells, and tissues (Figure 1.1). Though this interfacing, these polymers can be used to overcome various challenges in vaccine delivery, gene therapy, and cancer therapy. Polymers can interface with proteins via hydrogen bonding to stabilize protein vaccines during storage and exposure to elevated temperatures. Through mucoadhesion, polymers can interface with sublingual epithelium to enhance permeation of protein vaccines into the mucosal tissue. Due to electrostatic interactions, polymers can interface with plasmid DNA to form and stabilize condensed polyplexes to improve transfection efficiency. Through electrostatic and hydrophobic interactions polymers can interface with cell membranes to induce membrane lysis, increase cellular uptake of chemotherapy drugs, and sensitize cells to IRE.

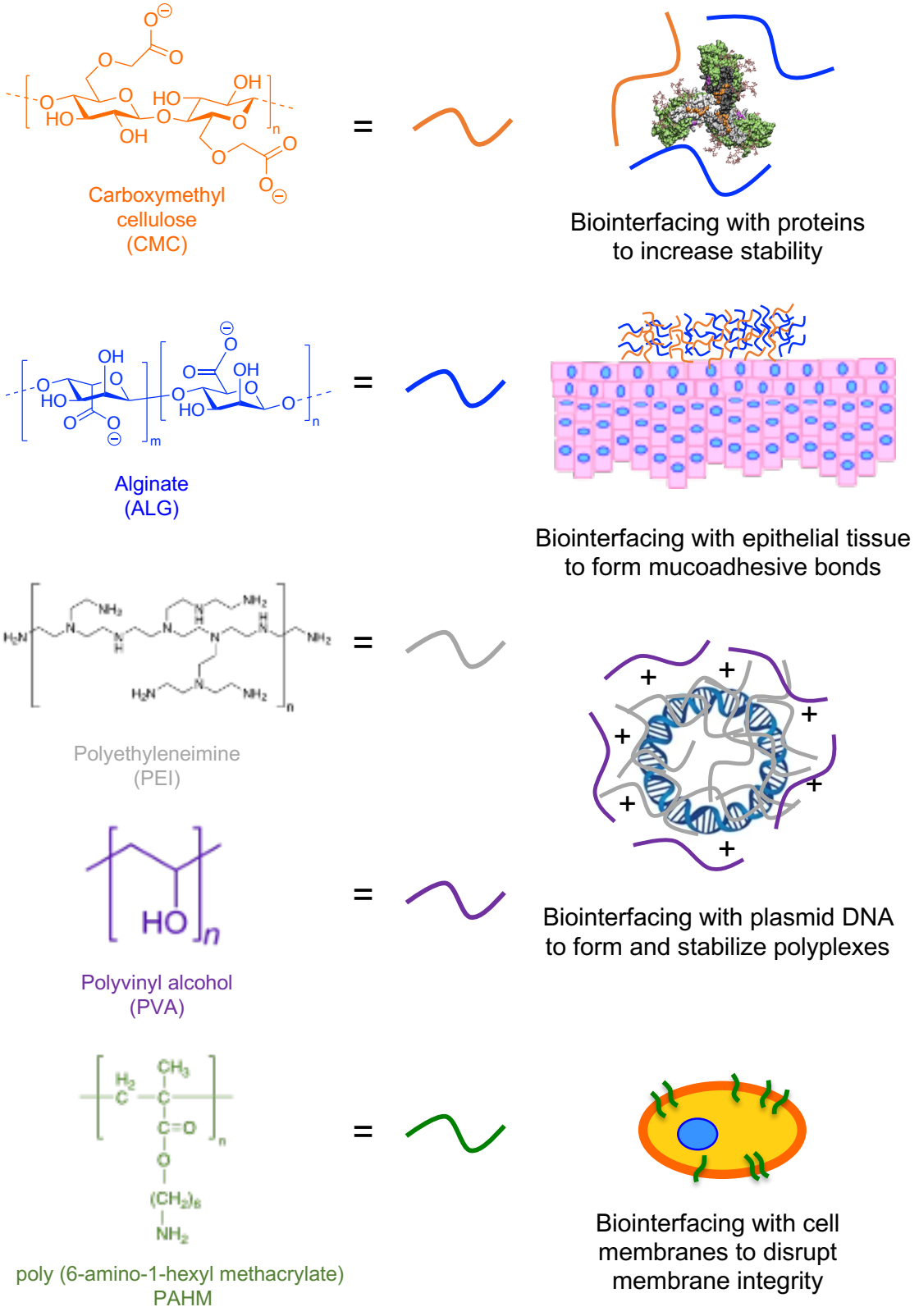

Figure 1.1 Polymers biointerfacing with biomolecules, cells, and tissues.

1.1 Polymer-based Drug Delivery Systems

Polymers have a long history of use in delivering therapeutic agents to treat numerous medical conditions. Typically intended to provide some sort of spatiotemporal control, polymeric delivery systems are designed to deliver drugs to targeted anatomical sites within a therapeutic range for a desired duration. Polymers can also stabilize and provide safe passage for therapeutic agents through inhospitable regions. Many different types of polymeric delivery systems have been developed, including implants, hydrogels, colloidal carriers (e.g., micelles, microparticles, nanoparticles), polymer conjugates (e.g., polymer-drug conjugates, polymer-protein conjugates) [1]. Drugs can be encapsulated in hydrophobic, solvent-free polymer implants, which release drugs either through passive molecular diffusion, polymer erosion/degradation, or a combination of the two [2]. Hydrogels, composed of a crosslinked polymer network and large amount of water, can encapsulate and provided sustained release of hydrophilic drugs. In addition, hydrogels can have similar physical properties to tissues, which can offer excellent biocompatibility [3]. Colloidal carriers can have a high drug loading capacity (of both hydrophilic or hydrophobic drugs), can facilitate cellular uptake, and can be easily conjugated for active targeting [4]. Polymers can be conjugated to pharmaceutical agents to modify transport and circulation half-life characteristics, reduce immunogenicity, and provide passive and active targeting [1].

The selection and design of a polymer can be difficult due to the vast diversity of characteristics required of a particular delivery system. Initially, polymers were intended to be inert carriers of a particular therapeutic; however, the need for polymers to be stimuli-responsive or exhibit bioactivity has been increasingly recognized [1]. Polymers

have been designed to respond to specific physical stimuli (such as temperature, ultrasound, light, and magnetic and electrical fields) or biochemical stimuli (such as pH, redox potential, and ionic strength) to trigger the release of a therapeutic agent [5]. Polymers have been designed to include passive or active targeting mechanisms to improve the distribution of a therapeutic agent within a particular tissue, cellular, or subcellular location [1]. Polymers with bioadhesive properties are especially useful when targeting mucosal tissues. Bioadhesive polymers can maintain sustained contact between a delivery system and mucosal epithelium, providing sufficient residence time for a therapeutic agent to permeate into the tissue [6]. Polymer conjugates have been widely used in anticancer agents due to the ability to passively target tumors via the enhanced permeation and retention (EPR) effect [7]. Once of the most commonly used polymers, polyethylene glycol (PEG), has been conjugated (i.e. PEGylation) to many FDA approved therapeutics [8]. The surface of nanoparticles, and other colloidal carriers, are often functionalized with ligands to actively target delivery to specific cell types [9]. Since many therapeutics are only effective if localized in a particular subcellular site (e.g., nucleus, cytosol, mitochondria), polymer carriers have also been designed to direct these agents to the appropriate site [10]. Polymers can also be designed to be biomimetic. Synthetic polymers designed to emulate the membranolytic abilities of host defense peptides have enormous potential as antimicrobial or anticancer agents [11].

1.2 Instability and Insufficient Mucosal Permeation of Sublingual Protein Vaccines

The large population of antigen presenting cells (APCs) in the sublingual mucosa make it a preferred site for antigen presentation (Figure 1.2) [12].

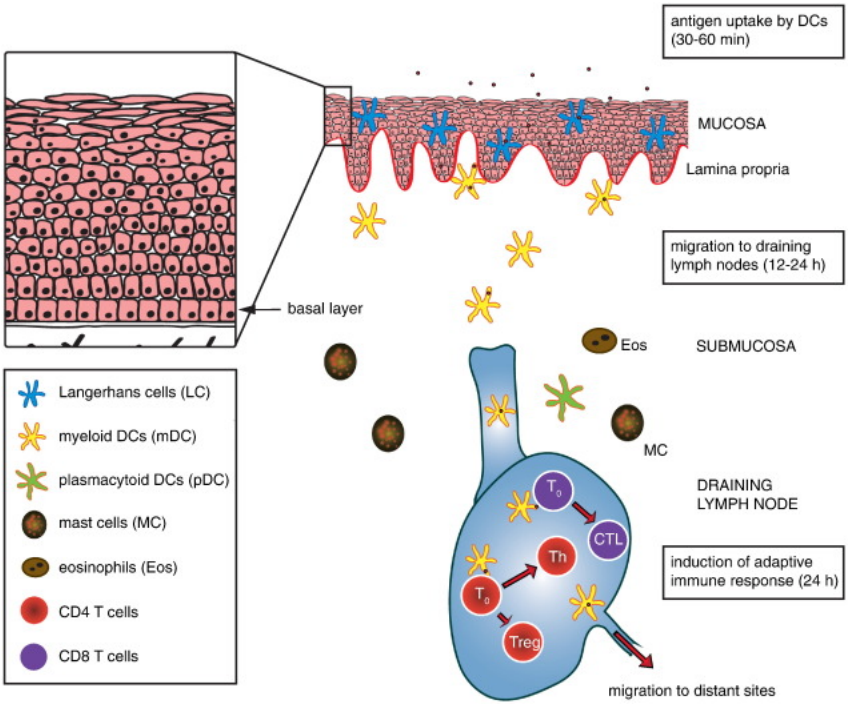

Figure 1.2 Antigen delivery and antigen presentation following sublingual vaccination. Sublingual mucosa contains many antigen presenting cells responsible for antigen uptake and induction of the adaptive immune response. Reprinted from Journal of Controlled Release, v. 190, H. Kraan, H. Vrieling, C. Czerkinsky, W. Jiskoot, G. Kersten, J.-P. Amorij, Buccal and sublingual vaccine delivery, p. 582, Copyright (2014), with permission from Elsevier.

Many viral and bacterial pathogens primarily infect mucosal sites [13]. While most intramuscular (IM) and subcutaneous (SC) injections confer systemic immunity, they induce insufficient mucosal immunity [14]. Sublingual vaccines have been shown to be safe and highly effective in several animal models [12]. Sublingual delivery of a clade C HIV-1 envelope protein gp140 with alpha-galactosylceramide (αGalCer) and CpG-oligodeoxynucleotide (CpG-ODN) as adjuvants has been shown to efficiently induce persistent humoral and cellular immune responses in the systemic and mucosal compartments of mice [15]. Genetic vaccination via the oral mucosa using cDNA for influenza A/WSN/33 (H1N1) hemagglutinin and the malaria *Plasmodium berghei* circumsporozoite protein (PbCSP) has generated antigen-specific CTL and IFN-γ production in hamsters [16]. Sublingual immunization with an adenovirus (Ad5)-based

vaccine for Ebola induced significant ZGP-specific Th1 and Th2 type responses that protected mice and guinea pigs from lethal challenge [17]. Sublingual delivery of an Ad5 SIV-env/rev and SIV-gag vaccine in Rhesus Macaques generated SIV-specific immunity, including cellular responses, serum binding antibody, and mucosal secretory IgA [18].

Despite the success in preclinical studies, sublingual vaccines are rarely used in humans. One factor limiting the success of sublingual vaccines is the way in which they are delivered. Sublingual vaccines are usually delivered as liquid formulations [12]. While these formulations enable convenient and exact dosing, they provide insufficient adhesion and absorption through the sublingual epithelium [19]. As a result, the vaccines can be physically removed from the delivery site (e.g., swallowing, talking, eating, drinking, saliva wash-out), resulting in poor immunogenicity. This is particularly problematic for protein vaccines. Despite the long success of sublingual delivery of small molecule drugs [20], macromolecules have been much harder to deliver by this route. The sublingual epithelium serves as a permeability barrier to macromolecules [12].

A few mucoadhesive dosage forms have been studied for sublingual delivery of protein vaccines. Thiolated chitosan wafers have developed to improve the buccal delivery of insulin. While these wafers demonstrated a 1.7-fold increase of insulin delivery into EpiOral™ buccal tissue and sheep buccal membrane ex vivo, they have not shown efficacy in vivo [21]. Engineered liposomes (phospholipid-PEG liposomes coated with methylglycol chitosan) carrying CRX-601 (a synthetic toll like receptor-4 agonist), have been co-delivered sublingually with influenza antigens. In addition to being mucoadhesive, these liposomes may also act as permeation enhancers by opening epithelial tight junctions. Sublingual administration of this vaccine formulation generated

systemic immune responses and mucosal immune responses that were or comparable to or exceeded those generated IM administration [22]. While the stability of the liposomes was preliminarily tested, the stability of the influenza antigens was not. Combinations of Carbopol®, lactose, microcrystalline cellulose (MCC), hydroxyproply methylcellulose (HPMC), and ethylcellulose (EC) were used to formulate bilayer tablets (composed of a mucoadhesive layer and a controlled release layer) to investigate the effect of the model protein antigen (OVA) release rate on the immune response after sublingual immunization in mice. When compared to OVA in solution, fast protein release tablets (~5 min) elicited comparable antibody titers. However, the extended protein release (~24 h) only induced low immune responses [23]. The immunized mice likely swallowed or spit out the extended release tablets before the full OVA dose was released. The issue of antigen stability was not addressed in this study. Bilayer films have also been investigated for buccal immunization in rabbits. Films composed of Noveon and Eudragit S-100 as the mucoadhesive layer and a pharmaceutical wax as the impermeable backing layer were loaded with β-galactosidase (β-gal) as a model protein antigen. Buccal immunization elicited serum antibody titers equivalent, if not greater, to SC injection. Plasmid DNA (CMV-β-gal) was also loaded into the bilayer films. Buccal immunization with plasmid DNA also elicited comparable antigen-specific IgG titers to SC protein injection; however, only the rabbits immunized with plasmid DNA via the buccal route demonstrated splenocyte proliferative immune responses [19]. While the stability of the released cargo was demonstrated, long-term stability was not investigated.

A few formulations have been studied to improve delivery to oral mucosa while maintaining stability of biomacromolecules. Mucoadhesive electrospun patches have

recently been developed to deliver lysozyme to the oral mucosa for treating and preventing oral infections. Lysozyme was incorporated into poly(vinylpyrrolidone)/Eudragit RS100 nanofibers by electrospinning. Lysozyme released from the nanofibers maintained 96.1% of the enzyme activity and inhibited the growth of the oral bacterium *Streptococcus ratti* [24]. While the biological activity of lysozyme was preserved during preparation of the mucoadhesive patches, the issue of storage temperature or protection from heat denaturation was not investigated. Alginic acid nanoparticles, in combination with nicotinamide as a permeation enhancer, have been used to improve sublingual delivery of insulin. The mucoadhesive nanoparticles were shown to improve the pharmacological availability and bioavailability of insulin in a diabetic rat model. Albumin was added as a cryoprotectant to help preserve insulin. The chemical stability and structural integrity of insulin in nanoparticles was confirmed by HPLC and CD analysis [25]. While insulin stability was maintained after storage at 4ºC for 12 months, storage without refrigeration was not demonstrated. An oral cholera vaccine, Dukoral™ has been stabilized by sucrose during lyophilization; however, storage of the dry cholera vaccine formulation above 4ºC was not demonstrated [26]. An H5N1 flu virus vaccine has been stabilized by sublingual tablets composed of microcrystalline cellulose, crosslinked sodium carboxymethylcellulose, and mannitol. These tablets allow for storage at ambient temperatures, but the vaccines must be reconstituted prior to administration [27]. A commercial H1N1 flu virus vaccine (Fluarix®) has been incorporated into mucoadhesive tablets for delivery to the buccal mucosa of pigs. After three immunizations at 2 weeks interval, animals were challenged by inoculation of the A/H1N1 pandemic virus. While the buccal vaccine tablets showed

signs of priming the pig's immune system, intramuscular injection of the commercial liquid vaccine generated superior immune responses. Antigen immunogenicity was shown to be preserved when tablets were stored at 4ºC or room temperature for up to 6 months [28]. Antigen stability is likely due to the presence of the bulking agent mannitol and the lyoprotectant trehalose, not the mucoadhesive polymers. The flu vaccine was first freeze-dried with mannitol and trehalose before compression with magnesium stearate, fumed silica, and mucoadhesive polymer excipients (HPMC or milk protein concentrate). While these mucoadhesive dosages showed promise for sublingual vaccination, the protection of antigens from heat denaturation has not been addressed in these studies. Ideally, mucoadhesive formulation should protect protein antigens from inactivation due to lyophilization and heat exposure during storage and transport.

1.3 Inadequate Transfection Efficiency of Polyplex-Mediated Gene Delivery in the Presence of Serum

Gene therapy has the potential to treat or vaccinate against many diseases, including cancer, infectious diseases, and genetic disorders. Nucleic acids encoding for specific proteins from pathogens or mutated cancer cells can be delivered in DNA (or RNA) vaccines to instigate cell-mediated and humoral immune responses. Gene therapy can also deliver exogenous transgenes to replace or knockdown endogenous genes [29]. Gene delivery falls into two classes – viral and nonviral. Viral vectors have been genetically altered to prevent viral replication, reduce cytotoxicity, and allow incorporation of a therapeutic transgene. While these viral vectors can be very efficient, they have a limited gene carrying capacity, are unable to transfect nondividing cells, and can be difficult to mass-produce [30]. Moreover, immunogenicity and oncogenicity are significant safety

concerns that have limited their clinical applications [31]. Nonviral gene delivery involves the use of plasmid DNA either alone or, more commonly, complexed to synthetic carrier molecules. Nonviral systems address many of the issues associated with viral vectors, including flexibility in the transgene size, simplified manufacturing, and lower immunogenicity. However, nonviral systems are significantly less efficient than viral vectors [30].

The low efficiency of nonviral gene delivery is primarily due to the numerous barriers (Figure 1.3) between the site of administration and localization in the cell nucleus. DNA (and its delivery vehicle) are first susceptible to extracellular barriers, including enzymatic degradation by nucleases, complement-mediated clearance, and reticuloendothelial system recognition. Next, the DNA must cross the cell membrane. Endocytosis is the primary mechanism responsible for cellular uptake; however, DNA must escape from the endosomal compartments prior trafficking to lysosomes, where DNA is subject to intracellular degradation. Finally, DNA must be transported though the cytoplasm and translocate into the nucleus, where transcription of the transgene takes place [30].

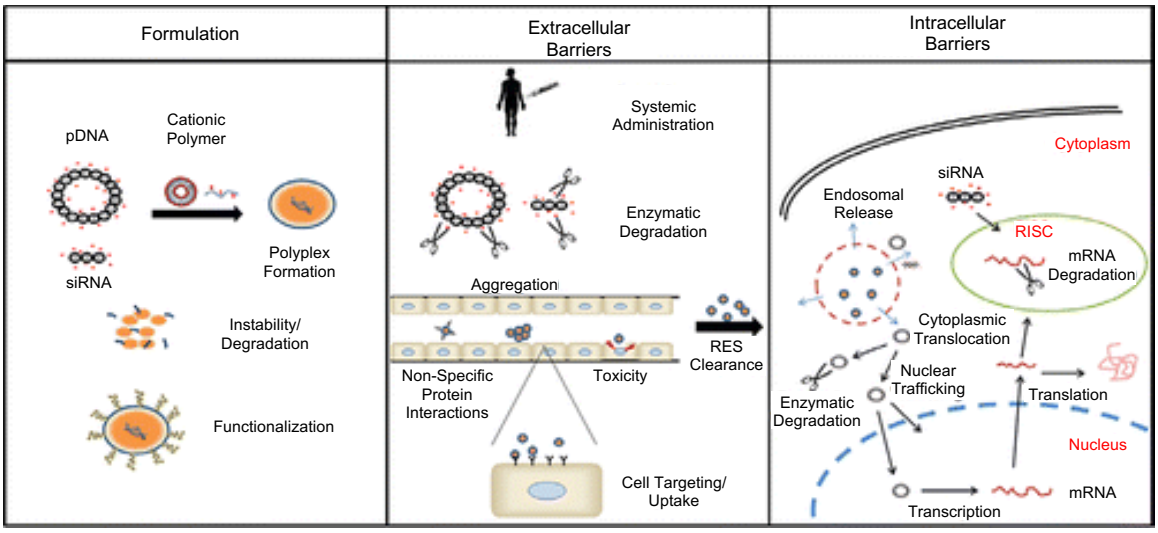

Figure 1.3 Barriers to polyplex-mediated gene delivery. Adapted with permission from Molecular Pharmaceutics, v.10, C.H. Jones, C.-K. Chen, A. Ravikrishnan, S. Rane, B.A. Pfeifer, Overcoming Nonviral Gene Delivery Barriers: Perspective and Future, p. 4082, Copyright (2013) American Chemical Society.

Many synthetic carriers have been developed to overcome these barriers to gene delivery. One of the commonly used type of carrier are cationic polymers, which form complexes with anionic DNA via electrostatic interactions. These condensed sub-micron-size particles are termed polyplexes [29]. Polyplexes can protect DNA from nuclease degradation and enhance cellular uptake, due to the attraction of the net-positively charged polyplexes to negatively charged cell membranes [30]. Many cationic polymers have been used to form polyplexes, including poly-L-lysine (PLL), polyamidoamine (PAMAM), and polyethyleneimine (PEI) [32]. PEI is the most commonly used polymer to form polyplexes for gene delivery [33]. The repeating amine structure not only allows PEI to form compact and tightly bound polyplexes to protect DNA from nuclease degradation and facilitate cellular uptake, but the numerous secondary and tertiary amines in branched PEI are thought to facilitate endosomal escape by the "proton sponge" mechanism. As the polyplex-containing endosome acidifies, the amines become protonated, which promotes the influx of additional H^+ ions and Cl^- counterions. To

account for the increased ion influx, additional water also enters the vesicle. This results in osmotic swelling and eventual rupture, releasing the polyplexes into the cytosol [29].

Despite the improvement over naked DNA, polyplex-mediated gene delivery still struggles in vivo. A primary issue with polyplexes is their colloidal instability. Adsorption of serum albumin and other anionic proteins can cause polyplexes to aggregate, degrade, or unpackage, resulting in poor cellular uptake and ultimately low transfection efficiency [29]. Various strategies have been investigated to improve polyplex colloidal stability and transfection efficiency. Covalent attachment of PEG to polyplexes was hypothesized to provide a steric barrier against aggregation and reduce interaction with blood components. However, PEGylated polyplexes were actually less stable in blood. The PEGylated polyplexes were found to unpackage more easily, likely due to the presence of PEG trapped in the core of the polyplexes, weakening the electrostatic interactions holding them together [34]. Covalent attachment of polyvinyl alcohol (PVA) to PEI has also been explored. The PVA-PEI/DNA polyplexes displayed high in vitro transfection efficiency in the presence of serum. The transfection efficiency of PVA-PEI/DNA polyplexes were also examined in mice. Seven days after intravenous injection, gene expression was high in the spleen; however, transfection efficiency was lower in other major organs (lungs, heart, kidney, liver, brain) [35]. Succinylation of primary and secondary amines of PEI to produce zwitterion-like polyplexes has been shown to decrease aggregation and increase the in vitro transfection efficiency in the presence of serum. A balance between the advantages of succinylation with the required charge density to condense and protect DNA was discovered. Polyplexes with 9 – 25% of the amines modified by succinylation were found to be most effective. Transgene

expression was up to 51-fold greater than unmodified PEI/DNA in the presence of serum; however, these zwitterion-like polyplexes were not tested in vivo [36]. PEI-based polyplexes (and lipopolyplexes) have also been encapsulated into PVA microparticles. This nanoparticles-in-microparticle delivery system (NiMDS) was found to reduce cytotoxicity and enhance the transfection efficiency in the presence of serum in multiple cell lines [37]. The NiMDS was also spray dried into a powder and delivered to mice by an inhalation chamber. Approximately 1% of lung cells expressed the transgene after one administration; however, the transfection efficiency of the NiMDS was not tested in other organs [38]. Ideally, a polymeric delivery system should enhance the transfection efficiency of nonviral gene therapy and be capable of delivering genes to different tissues.

1.4 Cancer Cell Resistance to Chemotherapy Drugs

Cancer remains a leading cause of morbidity and mortality globally. An estimated 13.1 million people will die due to cancer in 2030 [39]. Chemotherapy is a current standard of care for many types of cancer; however, resistance to chemotherapeutics plagues many treatment regimens [40]. Many classes of chemotherapy drugs have been developed, including taxanes, anthracyclines, epipodophyllotoxins, and antimetabolites. Despite the structural and functional differences of these drugs, most anticancer agents have intracellular targets [11]. Cancer cells that develop mechanisms to pump the drugs out of the cells or deactivate the drugs with certain intracellular pathways can become multidrug resistant (Figure 1.4) [41]. While dose escalation can theoretically increase intracellular drug concentration, it can also exacerbate resistance mechanisms and toxic side effects [42].

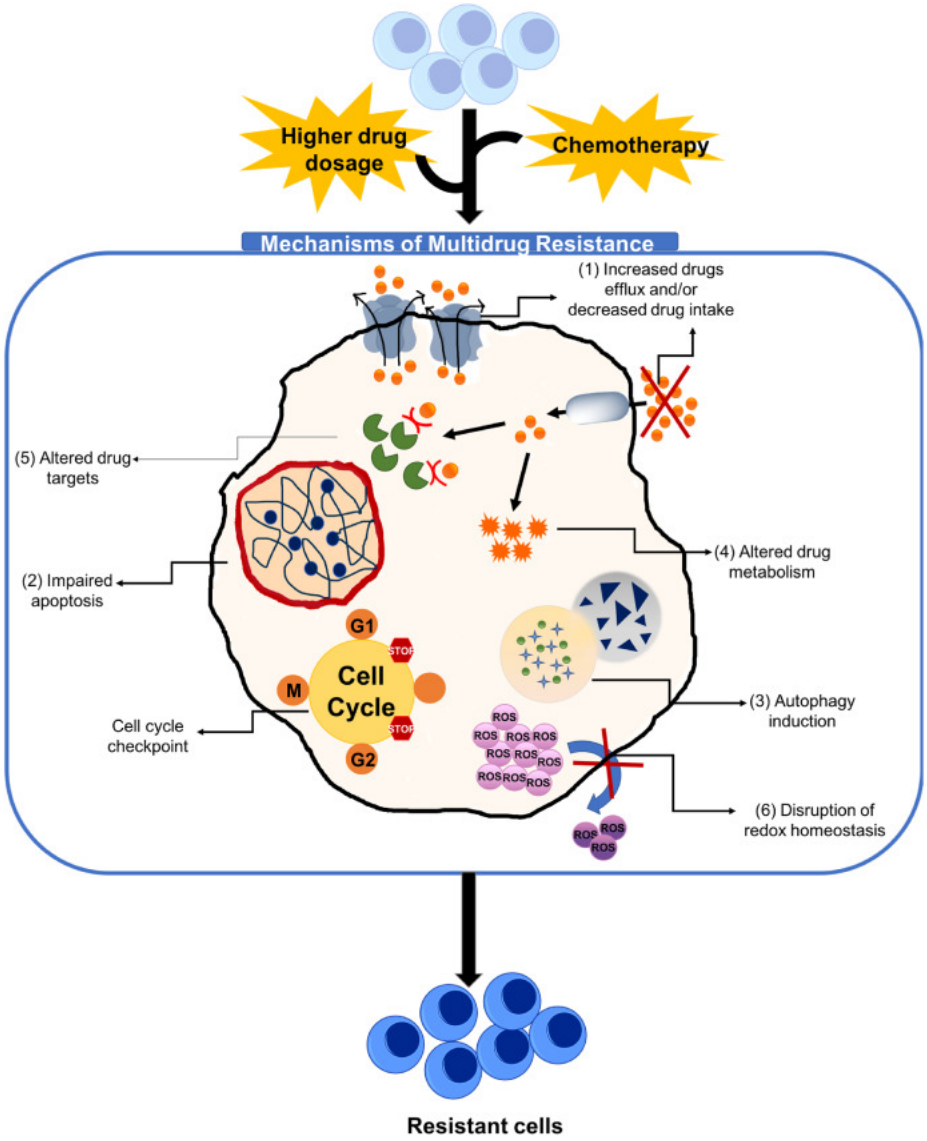

Figure 1.4 Mechanisms leading to multidrug resistance in cancer cells. Mechanisms leading to multidrug resistance in cancer cells. Reprinted from Biomaterials, v. 252, J. Tan, J. Tay, J. Hedrick, Y.Y. Yang, Synthetic macromolecules as therapeutics that overcome resistance in cancer and microbial infection, p. 8, Copyright (2020), with permission from Elsevier.

In addition to multidrug resistance, low accumulation in tumor tissue, poor aqueous solubility, short circulation half-life, and off-target toxicity have limited the efficacy of many chemotherapy drugs [40]. Because many chemotherapeutics target rapidly dividing cells they can also display toxicity against fast-dividing non-malignant cells, resulting in decreased blood cell production, digestive tract inflammation, and hair loss [43]. To

combat some of these issues, thousands of nanoparticle delivery systems have been developed, about a dozen of which have been FDA approved from clinical use [42]. Encapsulation of doxorubicin in liposomes (i.e. Lipodox®) results in the preferential accumulation in tumor tissue while limiting cardiotoxicity. The liposomes are unable to cross vasculature with tight capillary junctions (e.g., in myocardium) but can escape leaky tumor vasculature [39]. PEGylated-liposomal doxorubicin (i.e. Doxil®/Caelyx®) can also prolong the circulation half-life by reducing uptake by the reticuloendothelial system [44]. Despite the advantageous of these nanoparticle delivery systems, they rely on the intracellular action of the drug and are still susceptible to multidrug resistance mechanisms [43]. It may be more difficult for cancer cells to develop resistance to therapies that do not have intracellular targets [45], such as membranolytic polymers or irreversible electroporation. These membrane-targeting approaches could be used as monotherapies or combined with conventional chemotherapy for a potential synergistic effect.

1.5 Inability of Irreversible Electroporation to Ablate Large Tumors

Irreversible electroporation (IRE) involves the use of high-voltage short electrical pulses to create permanent pores within a cell membrane, leading to cell death by permanent membrane lysis or loss of homeostasis (Figure 1.5) [46]. IRE can be used as a focal therapy to ablate tumors, similar to cryoablation, radiofrequency ablation, or microwave ablation [47]. These thermal ablation modalities are minimally invasive treatment options for patients with tumors in various organs, including liver, lungs, and kidneys [48,49]. However, the reliance on heating or cooling to induce cell death carries the risk of damaging healthy tissues, such as blood vessels, bile ducts, and nerves [50].

Additionally, the thermal energy can be dissipated by nearby blood flow, creating a heat sink (or cold sink) effect that limits the ability to ablate tumors that are adjacent to major blood vessels [47].

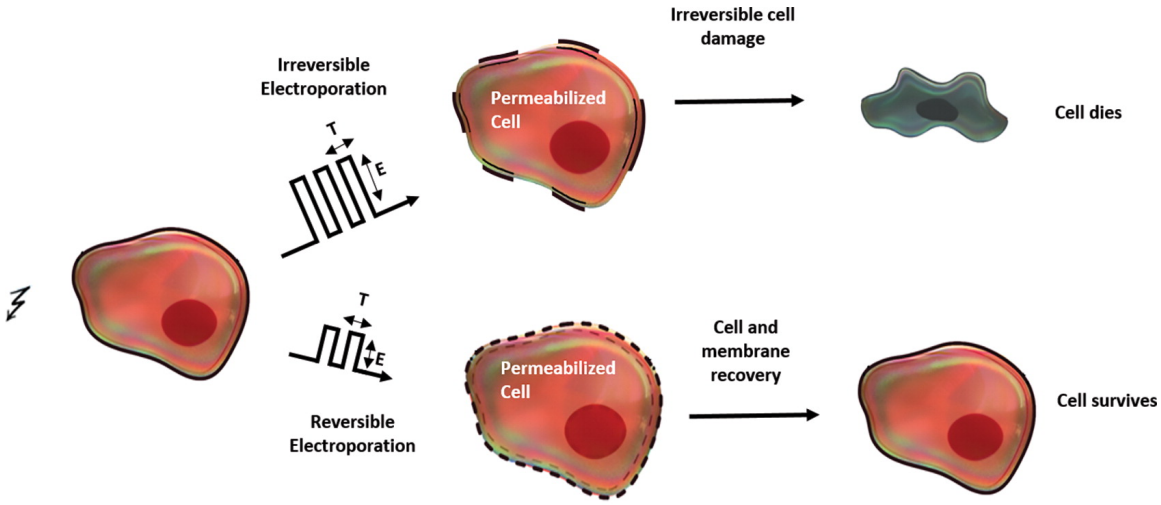

Figure 1.5 Schematic illustration of irreversible electroporation (IRE). IRE uses a series of high-voltage short electrical pulses to permanently disrupt cell membranes, leading to cell death. Reprinted from Radiology, v. 295, B. Geboers, H.J. Scheffer, P.M. Graybill, A.H. Ruarus, S. Nieuwenhuizen, R.S. Puijk, P.M. van den Tol, R. V. Davalos, B. Rubinsky, T.D. de Gruijl, D. Miklavčič, M.R. Meijerink, High-Voltage Electrical Pulses in Oncology: Irreversible Electroporation, Electrochemotherapy, Gene Electrotransfer, Electrofusion, and Electroimmunotherapy, p. 254-272, Copyright (2020), with permission from Radiological Society of North America.

In contrast IRE, a nonthermal therapy, can be used to ablate tumors near large blood vessels or vital structures, such as sensitive vasculature, bile ducts, urethra, or nerves [51]. Due to specificity for the cell membrane, IRE also spares the extracellular matrix, allowing for faster healing of healthy tissue while minimizing scarring [52]. IRE is currently used to treat tumors in the prostate, liver, pancreas, and kidneys [53,54] and may be efficacious for tumors in other organs, such as the lungs, breast, brain, and spinal cord [55,56].

Despite the advantages of IRE, it is usually considered a “last resort” for patients [57]. A critical disadvantage of IRE is the inability to ablate large tumors (e.g. >3 cm in

diameter) under a safe electric field strength [58]. IRE relies on two or more needle electrodes to deliver the high-voltage pulses (Figure 1.6); however, the electric field intensity decreases with distance from an electrode [59]. If the electric field intensity drops below the effective electric field threshold (500–1000 V/cm depending on the cell type [46]), the cancer cells will be able to repair the membrane and remain viable, resulting in incomplete tumor ablation [60].

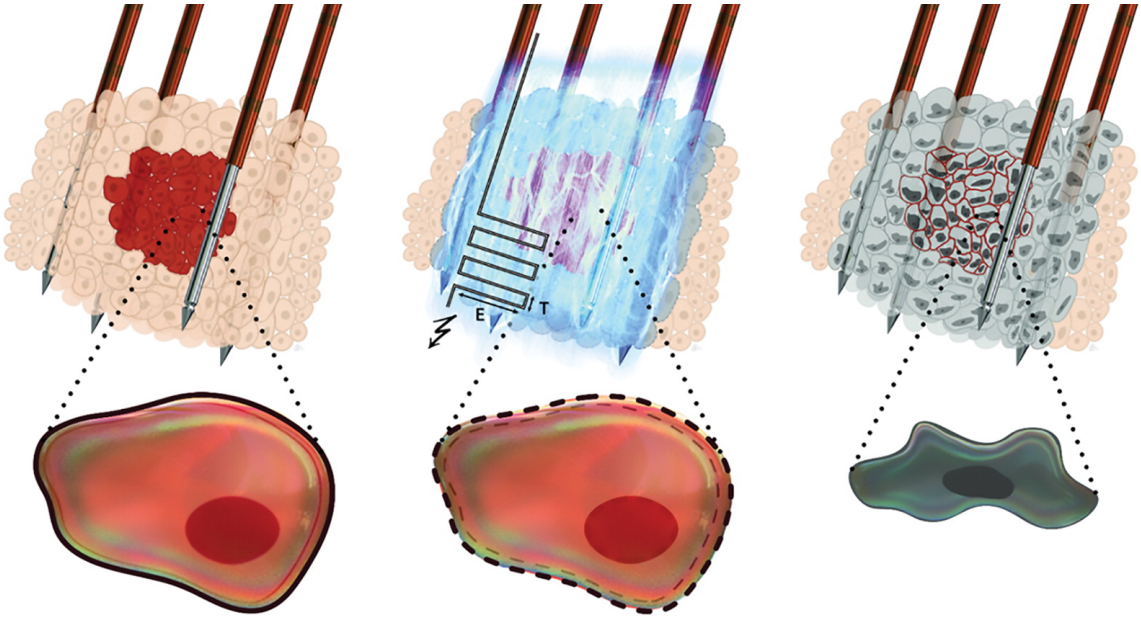

Figure 1.6 Illustration of IRE-mediated tumor ablation. Needle electrodes are inserted into the tumor tissue to deliver the high-voltage pulses. Cells within the ablation volume will be exposed to electric field strengths above the effective threshold, leading to cell death. Reprinted from Radiology, v. 295, B. Geboers, H.J. Scheffer, P.M. Graybill, A.H. Ruarus, S. Nieuwenhuizen, R.S. Puijk, P.M. van den Tol, R. V. Davalos, B. Rubinsky, T.D. de Gruijl, D. Miklavčič, M.R. Meijerink, High-Voltage Electrical Pulses in Oncology: Irreversible Electroporation, Electrochemotherapy, Gene Electrotransfer, Electrofusion, and Electroimmunotherapy, p. 254-272, Copyright (2020), with permission from Radiological Society of North America.

While it is possible to increase the ablation volume by increasing the electrode voltage, extremely high voltage can damage adjacent nerves and cardiac tissue [61,62] and heat can be generated in the proximity of the electrodes (due to Joule heating) [63]. Larger tumors can be treated with IRE by increasing the number of electrodes or

repositioning the electrodes; however, this increases the complexity and invasiveness of the procedure [46,58]. Repeated IRE treatments can be performed to try to fully ablate a tumor, but this is avoided when possible because patients must undergo general anesthesia and receive neuromuscular blocking agents to prevent uncontrolled severe muscle contractions from the electrical pulses. Additionally, cardiac monitoring and synchronized pulsing with heart rhythm is necessary to reduce the risk of inducing cardiac arrhythmias [47,54].

An attractive way to improve IRE is to lower the electric field threshold required to induce cell death. One way to do this is by sensitizing the cell membrane to make it more susceptible to IRE [60]. A number of molecules have been shown to sensitize cells to IRE, including cationic molecules (such as procaine, tetracaine, lidocaine, and polyarginine), sodium dodecyl sulfate (SDS, a small-molecule surfactant) and dimethyl sulfoxide (DMSO, a polar aprotic solvent) [46,58,64–66]. Membranolytic polymers may be able to similarly sensitize cell membranes to IRE to kill cells at moderate electric fields strengths and increase the ablation volume.

1.6 Thesis Overview

In this thesis, we aim to use biointerfacing polymers to overcome four challenges in vaccine delivery, gene therapy, and cancer therapy. Chapter 2 focuses on developing a simple biopolymer platform of mucoadhesive wafers that enables effective sublingual delivery and preservation of protein vaccines. In chapter 3, similar polymer wafers were used to enhance polyplex-mediated transfection in serum free and 10% serum conditions in vitro. Chapter 4 focuses on the use of a membranolytic polymer, poly (6-amino-1-hexyl methacrylate) (PAHM) to disrupt cancer cell membranes to increase cellular uptake

of the chemotherapy drug doxorubicin (DOX) and synergistically kill cancer cells. In chapter 5, PAHM was combined with irreversible electroporation (IRE) to kill cancer cells. Chapter 6 discusses future directions to improve these polymer systems.

Chapter 2 Mucoadhesive Wafers Composed of Binary Polymer Blends for Sublingual Delivery and Preservation of Protein Vaccines

Reprint of: S.M. Hanson, S. Singh, A. Tabet, K.J. Sastry, M. Barry, C. Wang, Mucoadhesive wafers composed of binary polymer blends for sublingual delivery and preservation of protein vaccines, J. Control. Release. 330 (2021) 427–437. https://doi.org/10.1016/j.jconrel.2020.12.029.

2.1 Introduction

The sublingual mucosa is a highly attractive site of vaccination for multiple reasons. Accessibility of the oral cavity allows for self-administration of needle-free vaccine dosage forms. The oral mucosal environment is rather benign. Unlike enteric oral vaccines, sublingual vaccines are not subject to the hostile environment of the gastrointestinal tract and can avoid first-pass clearance by the liver [12,67]. The presence of a large population of antigen presenting cells (APCs) makes the sublingual mucosa an important site for antigen acquisition and presentation [12], since many viral and bacterial pathogens invade mucosal tissues [13]. While most intramuscular and subcutaneous vaccines confer systemic immunity, they often induce insufficient mucosal immunity [14]. Sublingual vaccines have been shown to confer mucosal immune responses and protective immunity against numerous pathogens, including influenza, SARS, RSV, HIV-1, and HPV [68]. Various sublingual vaccines have been shown to be safe and highly effective in several animal models [12]. However, despite the success in preclinical studies, sublingual vaccines are rarely used in humans. While sublingual immunotherapy (SLIT) has been used clinically to treat allergy and hypersensitivity, very few sublingual vaccines for infectious diseases have reached clinical stage [12,69].

One factor limiting the success of sublingual vaccines is that their formulations are less than optimal. Sublingual vaccines are often delivered as liquid formulations [12].

While these formulations enable convenient and exact dosing, they do not provide sufficient adhesion to and absorption through the sublingual epithelium. As a result, the liquid vaccines can be physically removed from the sublingual site (e.g., due to swallowing, talking, eating, drinking, or saliva wash-out) [70], resulting in poor immunogenicity. This is particularly problematic for protein vaccines. Despite the commercial success of sublingual delivery of small molecule drugs [20], macromolecules have been much harder to deliver by this route, presumably due to the sublingual epithelium acting as a low-permeability barrier [12,67]. Mucoadhesive delivery systems can be used to hold macromolecules in place at the delivery site, providing sufficient time for permeation into the sublingual mucosa [71]. Mucoadhesive dosage forms containing a variety of synthetic and biological polymers have been shown to improve the oral mucosal delivery of peptides [72] (such as insulin [73]), proteins [74–79] and DNA [19].

Vaccine formulations generally contain highly sensitive and fragile biological molecules that are susceptible to denaturation and degradation due to exposure to elevated or fluctuating temperatures [80]. A cold chain is necessary to maintain vaccines under refrigerated condition throughout storage and distribution [81]. Considerable amount of work has been done on developing lyophilized vaccine formulations. These formulations generally contain various stabilizing excipients that can protect vaccines and prolong vaccine shelf-life [82,83]; however, the majority of FDA approved freeze-dried vaccines still require storage at 2 – 8 ºC and must be reconstituted in an appropriate buffer before use, which can lead to further loss of activity [81]. Recent reports on mucoadhesive sublingual delivery systems based on nanoparticles [25], patches [24], bilayer tablets [23] and films [19] have shown success in delivering peptides and proteins

such as insulin [25], lysozyme [24], ovalbumin [23], and β-galactosidase [19], but storage stability of the cargos was not adequately addressed and these vaccine formulations still required cold chain.

While a large number of mucoadhesive polymers are available [84], the adoption of particular ingredients to create sublingual formulations seems to be based on trial and error and thus lacking rational design. The compositions of sublingual drug products are often unnecessarily complex. More importantly, very few have investigated stabilization of sublingual protein vaccines and none have demonstrated sufficient protection of the active protein components from environmental damage due to excess heat and lyophilization. On the other hand, although there is a large body of literature dedicated to protein stabilization and preservation without needing the cold chain, such systems have not been integrated with mucoadhesive materials and hence are not yet conducive to sublingual administration [82,85,86].

The objective of the present study is to develop a simple biopolymer platform of mucoadhesive wafers that enables effective sublingual delivery and preservation of lyophilized protein vaccines. The wafers were composed of a series of binary polymer blends of carboxymethylcellulose (CMC) and alginate (ALG) (Figure 2.1). The influence of polymer composition on the microstructure, mechanical properties, disintegration time, release kinetics of model compounds, and mucoadhesive strength of the wafers was investigated. Ex vivo experiments were conducted to assess quantitatively the depth of permeation of a model protein (bovine serum albumin) into the sublingual submucosa and resistance to wash-out. β-galactosidase was used as a model for assessing the ability of the wafers to protect against inactivation during lyophilization and heat

challenge. Finally, wafers with the optimal composition were loaded with HIV gp140 protein and used to vaccinate mice sublingually in combination with an adjuvant (αGalSer). The induction of antigen-specific mucosal and systemic immune responses was evaluated and compared with freshly prepared aqueous protein antigen.

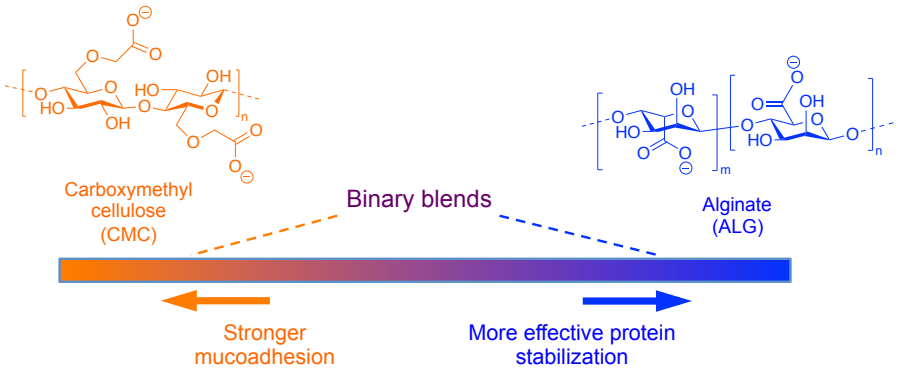

Figure 2.1 Rationale of design of mucoadhesive wafers consisting of binary polymer blends for sublingual delivery and stabilization of protein vaccines.

2.2 Materials and Methods

2.2.1 Chemicals and reagents

ALG (sodium alginate from brown algae, viscosity of 1% aqueous solution at 20 ºC: 100 – 200 cP), CMC (sodium salt, MW ~ 90 kDa, degree of substitution: 0.65 – 0.90, viscosity of 4% aqueous solution at 25 ºC: 50 – 200 cP), bovine serum albumin (BSA), fluorescein (sodium salt), rhodamine B isothiocyanate (RBITC), 2-mercaptoethanol (2-ME), 2-nitrophenyl β-D-galactopyranoside (ONPG), and β-galactosidase (β-Gal) from *E. coli* (grade VII, lyophilized powder, ≥ 500 units/mg protein) were from Sigma Aldrich (St. Louis, MO). Rhodamine B-labeled BSA (Rh-BSA) was prepared by reacting RBITC (50 µg in 50 µL DMSO) with BSA (1 mg in 1 mL PBS) for 2 h at room temperature followed by dialysis against phosphate buffered saline (PBS, 20 mM, pH 7) for 3 days. Dried Rh-BSA was obtained by lyophilization. Bovine submaxillary mucin (MW: 4 ~ 40 × 10^5 Da) was from Worthington Biochemical (Lakewood, NJ). Simulated saliva was

freshly prepared before use and contained KH_2PO_4 (0.19 mg/mL), Na_2HPO_4 (2.38 mg/mL), NaCl (8 mg/mL), mucin (1 mg/mL), with pH adjusted to 6.8 [87]. The HIV/Clade C gp140 protein was obtained from AIDS Research and Reference Reagent Program (Germantown, MD). α-Galactosylceramide (αGalCer) was purchased from Diagnocine LLC (Hackensack, NJ).

2.2.2 Preparation of blank and cargo-loaded polymer wafers

Five aqueous stock solutions were prepared comprising the following CMC:ALG ratios (wt:wt): 0:1, 1:2, 1:1, 2:1, and 1:0 by dissolving appropriate amounts of the polymers as well as NaCl in deionized water at a final combined polymer concentration of 2.25% (w/v) and salt concentration of 150 mM. After brief heating at 70 ºC to facilitate complete dissolution of the polymers, 1 N NaOH was used to adjust the pH of the polymer solutions to 7. To prepare blank wafers, aliquots of 100 µL of the polymer solutions were dispensed in 96-well flat-bottom plates, frozen at -80 ºC overnight and lyophilized under 0.020 mBar for 72 h in a FreeZone ® Freeze Dry System (Labconco, Kansas City, MO) equipped with a Maxima™ C Plus Vacuum Pump (Model M8c, Fisher Scientific). After drying, the wafers were carefully removed from the wells and compressed to ~0.5 mm thick by applying a constant force of 30 pounds for 5 sec. Hundreds of wafers were prepared using this method. The wafers were weighed and the diameter and thickness were measured using a digital caliper. The same protocol was used to prepare polymer wafers containing various cargos, including fluorescein (0.3 mg/wafer, for measuring in vitro release rate), Rh-BSA (0.3 mg/wafer, for measuring in vitro release rate and tissue penetration), β-Gal (0.3 Units/wafer, for evaluating stabilization against lyophilization and heat), HIV gp140 (5 µg/wafer, for testing

immunogenicity in mice). The cargos were added to and mixed with the polymer solutions before lyophilization. All the wafers were stored under ambient condition without desiccation.

2.2.3 Scanning electron microscopy (SEM)

To examine the surface morphology of the polymer wafers, SEM was performed using a Hitachi S-4700 Cold Field Emission Gun Scanning Electron Microscope (FEG-SEM) operated at an accelerating voltage of 1.5 kV and an emission current of 10 μA. Prior to imaging, polymer wafers were adhered to SEM specimen stubs by double-sided carbon tape.

2.2.4 Mechanical testing

To perform tensile tests, each wafer was secured by a custom-made clamp, mounted on a Q Series Mechanical Test Machine (TestResources Inc., Shakopee, MN) and pulled at a constant speed of 1 mm/min until fracture. Data collection and analysis were performed using the XY Software package provided with the instrument. Tensile strength, Young's modulus, and elongation at break were obtained from the recorded stress-displacement curves.

2.2.5 Disintegration time and in vitro release kinetics

Polymer wafers were submerged in 1 mL of fresh simulated saliva in 24-well plates at 25 ºC. The disintegration time was determined as the time at which the wafers disintegrated and no residual material was visible to the naked eye. When wafers containing fluorescein or Rh-BSA underwent disintegration, 100 μL of the supernatant was sampled and replaced with fresh simulated saliva at particular time points. The amount of fluorescein or Rh-BSA in the supernatant was quantified by measuring

fluorescence emission intensity at 528 nm (fluorescein, excitation at 485 nm) and 590 nm (Rh-BSA, excitation at 530 nm) using a Synergy HT plate reader (BioTek Instruments, Winooski, VT). Release kinetic profiles were expressed as the cumulative percentage released over time.

2.2.6 Ex vivo characterization of wafer adhesion to porcine sublingual mucosa

Fresh sublingual mucosal tissue was harvested from Mongrel swine (average body weight: 30 – 40 kg), donated by the Iaizzo Visible Heart® Laboratory (Department of Physiology, University of Minnesota). The entire tongue of the pig with intact sublingual tissue on the ventral side was removed, cut into cubes (2.5 × 2.5 × 1.0 cm) and mounted onto a Q Series Mechanical Test Machine (TestResources Inc., Shakopee, MN) with a custom clamp. Prior to each measurement, 100 μL of freshly prepared simulated saliva was applied evenly to the mucosal tissue. Each polymer wafer was mounted onto a probe and slowly brought into contact with the mucosal tissue. A contact force of 50 mN was applied and held for 1 min to initiate adhesion between the wafer and the mucosal tissue. The probe was then pulled at a constant speed of 1 mm/min until the wafer was detached from the mucosal surface. Data collection and analysis were performed using the XY Software package provided with the instrument. The resulting stress-displacement plot was used to determine (1) maximum detachment stress (σ_{max}), defined as the peak stress, and (2) work of adhesion per unit area (W_{ad}), calculated as the area under the curve.

2.2.7 Ex vivo permeation of Rh-BSA through porcine sublingual mucosa

Fresh porcine tongue was cut into cubes (1.5 × 1.5 × 0.5 cm) and 50 μL of simulated saliva was applied evenly to the surface of the sublingual mucosal tissue. Wafers containing Rh-BSA were pressed to the wet sublingual tissue. For comparison, an

equivalent amount of free Rh-BSA in 10 µL of buffer was applied to a different piece of tissue. After two minutes, both mucosal surfaces were rinsed with 10 mL of deionized water for 20 sec to mimic saliva washout. Two hours later the tissues were examined for residual Rh-BSA on the mucosal surfaces, photographed, and embedded in Tissue-Tek® O.C.T (Sakura Finnetek USA, Torrance, CA), flash-frozen with liquid nitrogen and stored at -80 ºC overnight. Any residual wafer material was carefully removed from tissue surface before embedding in O.C.T. The frozen tissues were sectioned with a Leica CM1990 Cryostat (North Central Instruments, Plymouth, MN) to the thickness of 15 µm. Fluorescent and bright-field images of the tissue sections were acquired with an Olympus IX70 inverted fluorescence microscope equipped with an Olympus DP72 camera and X-Cite 120 Wide-Field Fluorescence Microscope Excitation Light Source (Excelitas Technologies). Rh-BSA was visualized using an excitation wavelength of 535 ± 50 nm and emission wavelength of 610 ± 75 nm. An exposure time of 20 ms was selected for image capture to minimize tissue autofluorescence. The fluorescence intensity of the Rh-BSA was quantified up to a permeation depth of 250 µm using a custom MATLAB script and averaging six different images for each sample. Total amount of Rh-BSA in the sublingual tissue was quantified by calculating the area under the fluorescence intensity-permeation depth curves using GraphPad Prism version 8.2.1 (Graphpad software Inc., San Diego, California, USA).

2.2.8 Assessment of β-Gal activity after lyophilization and heat challenge

Polymer wafers containing β-Gal were reconstituted in phosphate buffer (93 mM Na phosphate, 1 mM $MgCl_2$ and 112 mM 2-ME, pH 7.3). The substrate ONPG was added to a final concentration of 2.3 mM and incubated at 37 ºC for 6 min. The absorbance at 410

nm corrected for blank buffer background was recorded using a Synergy HT plate reader (BioTek Instruments, Winooski, VT). β-Gal activity was reported as Unit/mg enzyme, where one Unit of β-Gal will hydrolyze 1.0 μmol of ONPG per minute at pH 7.3 at 37 ºC [88]. Using this method β-Gal activity of the following samples was determined: (1) aqueous solutions of free β-Gal and polymers; (2) lyophilized free β-Gal and β-Gal-containing polymer wafers; (3) lyophilized free β-Gal and β-Gal-containing polymer wafers after heating at 75 ºC for 30 min in a Dry Bath Incubator (Fisher Scientific).

2.2.9 Animals

Female CB6F1 (C57BL/6 X BALB/c) mice aged 6 – 10 weeks were purchased from the National Cancer Institute (Frederick, MD) and maintained in specific pathogen-free environment at the institutional animal facility at The University of Texas MD Anderson Cancer Center (Houston, TX). The animal facility is fully accredited by the Association for Assessment and Accreditation of Laboratory Animals Care International and all animal procedures were conducted in compliance with institutional approval (IACUC protocol number: 00000858-RN00).

2.2.10 Sublingual immunization

All wafers containing HIV gp140 were prepared at the University of Minnesota (Minneapolis, MN) and stored at room temperature without desiccation. They were packaged in zip-lock bags, shipped to the MD Anderson Cancer Center (Houston, Texas) with no refrigeration or desiccation, and stored on the bench under ambient condition for five days before in vivo testing. Mice in groups of five were first anesthetized by intraperitoneal injection of cocktail containing ketamine and xylazine hydrochloride (100 mg/kg and 10 mg/kg, respectively). For administration of vaccine as liquid solution, 5 μg

(in 10 µL of PBS) of freshly thawed gp140 protein with 2 µg (in 2 µL of DMSO) of αGalCer, a natural killer T (NKT) cell agonist and adjuvant, was deposited under the tongue of each animal using a previously described procedure [15]. For administration of the vaccine formulated in polymer wafers, mice were placed in dorsal recumbency and a single wafer containing 5 µg of gp140 was folded using a pair of forceps and then positioned under the tongue of each anaesthetized mouse. αGalCer (2 µg) was co-administered by depositing it sublingually on the wafer. To avoid swallowing, the animals were maintained with their heads in ante-flexion until they regained consciousness. All animals received two immunizations at 7-day intervals and both cell-mediated and antibody-mediated adaptive immune responses in different tissues were determined on day 14 after the first immunization.

2.2.11 Interferon-γ ELISpot assay

IFN-γ ELISpot assay was used to determine the antigen-specific responses of T lymphocytes isolated from cervical lymph nodes (CLNs) and the lungs of the immunized animals at day 14 after the first immunization according to a previously described protocol [89,90]. The T cells were stimulated by incubating with either medium alone or gp140 protein (1 µM) or Concanavalin A (5 µg/mL) for 48 h before secondary antibody treatment and color development of IFN-γ spot forming cells (SFC) using the commercial reagent kit (BD Biosciences, San Jose, CA). Enumeration of spots representing individual cells producing IFN-γ was performed by Zellnet Consulting Inc., (Fort Lee, NJ) using KS-ELISPOT automatic system (Carl Zeiss Inc., Thornwood, NY). Responses were considered positive only when they were above 10 SFC/2 x10^5 input cells and at least twice the number obtained in cells cultured with medium alone.

2.2.12 Antigen-specific antibody responses

Anti-gp140 antibody responses were evaluated in the blood, saliva and vaginal washes of immunized animals. Retro-orbital sinuses were used to collect blood samples. For collection of saliva, animals were first anaesthetized with ketamine and xylazine cocktail followed by induction of secretion of saliva by i.p. administration of pilocarpine (200 mg/kg). Saliva was collected using a micropipette. Vaginal washes were collected by repeated flushing with PBS. Serum (diluted 1:100) and mucosal secretions (diluted 1:5) were assayed for gp140 specific antibody levels by ELISA using standard protocols [91]. Horseradish Peroxidase (HRP)-conjugated goat antibodies to mouse IgG or IgA (KPL Inc., Gaithersburg, MD) were used for detection. The gp140 specific antibody concentration in the sample was determined by subtracting the optical absorbance at 450 nm of the pre-immunization samples from post-immunization sample for individual animals. For each group of five immunized mice, results were expressed as average absorbance ± SD.

2.2.13 Statistical analysis

ANOVA with Tukey's multiple comparisons test was used to determine the significance between different wafer compositions. Holm-Sidak t-test for multiple comparisons with $\alpha = 0.05$ was used to test Rh-BSA fluorescence intensity at each permeation depth. One-way ANOVA and Tukey HSD test for multiple comparisons were used to analyze the total amount of Rh-BSA present in the sublingual tissue. Paired two-tailed Student's t-test was used to determine the significance of difference between different immunization groups. All analyses were performed using GraphPad prism, version 8.2.1 (GraphPad software Inc., San Diego, California, USA).

2.3 Results

2.3.1 Appearance, microstructure, and mechanical properties of wafers

The average diameter, thickness, and weight of 80 to 100 wafers of various polymer compositions were measured and results summarized in Table 2.1. All the CMC:ALG ratios formed wafers with highly consistent average weight (3.3-3.4 mg) and average dimensions (diameter: 6.51-6.53 mm; thickness: 0.54-0.56 mm) with the exception of the pure CMC wafers, which were smaller (average diameter: 5.37 mm) and thinner (average thickness: 0.50 mm). Visual inspection of the wafers clearly showed such differences (Figure 2.2A). The pure CMC wafers had significant shrinkage with irregular shape and large heterogeneous pores. In contrast, wafers containing various amounts of ALG were round with minimal shrinkage after lyophilization and were macroscopically homogeneous.

In accordance with visual inspection, closer examination of the wafers by SEM revealed that different CMC:ALG ratio produced different microstructures. Pure CMC wafers had large pores and thick granular strands in the meshwork, whereas pure ALG wafers had much smaller pores and rather smooth polymer strands. Wafers with intermediate CMC:ALG ratios (such as 1:1) had intermediate pore sizes and morphology (Figure 2.2B).

Table 2.1 Average size and weight of mucoadhesive wafers prepared via a simple and robust process. Data shown are mean ± SD (n = 81-105).

Wafer composition (CMC:ALG)	Diameter (mm)	Thickness (mm)	Dry weight (mg)
CMC	5.37 ± 0.75	0.50 ± 0.08	3.4 ± 0.2
2:1	6.51 ± 0.18	0.54 ± 0.11	3.3 ± 0.2
1:1	6.53 ± 0.18	0.56 ± 0.08	3.3 ± 0.2
1:2	6.52 ± 0.16	0.54 ± 0.08	3.4 ± 0.2
ALG	6.51 ± 0.16	0.56 ± 0.07	3.3 ± 0.2

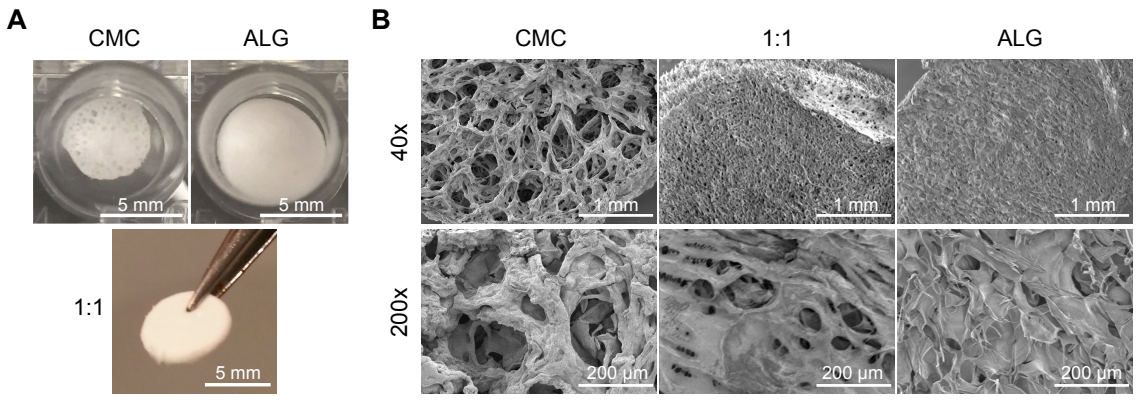

Figure 2.2 Macroscopic appearance (A) and microstructure (B) of the mucoadhesive wafers revealed by SEM.

Mechanical properties of the wafers were characterized by tensile test. The pure CMC wafers were rather stiff and brittle with the highest tensile strength and Young's modulus and the lowest elongation at break among all compositions (Table 2.2). Wafers containing ALG were more elastic and much easier to handle. With increasing ALG content, the wafers showed a general trend of reduced strength and increased elasticity.

Table 2.2 Mechanical properties of the mucoadhesive wafers. Data shown are mean ± SD (n=5).

Wafer composition (CMC:ALG)	Tensile strength (kPa)	Young's modulus (kPa)	Elongation at break (%)
CMC	314.8 ± 151.5	589.2 ± 152.2	65.5 ± 22.6
2:1	66.6 ± 10.5	304.2 ± 69.5	91.7 ± 33.2
1:1	78.6 ± 14.9	240.8 ± 91.5	111.2 ± 49.9
1:2	70.6 ± 9.8	248.8 ± 99.2	113.4 ± 23.0
ALG	80.7 ± 12.6	132.7 ± 97.6	151.6 ± 77.8

2.3.2 Disintegration time and release kinetics

The polymer wafers were submerged in simulated saliva to determine how wafer composition would affect disintegration time. The pure CMC wafers disintegrated completely in 45 min, significantly faster than all other compositions, which disintegrated in 70-80 min (Figure 2.3A). Fluorescein (MW 376.28 g/mol) was released from the

wafers with approximately first-order kinetics (Figure 2.3B). All compositions reached 100% release after approximately 40 min, prior to the complete disintegration of the wafers. On the other hand, BSA (MW 66 kDa) was released more slowly than fluorescein, following approximately zero-order kinetics for 1 h before slightly leveling off (Figure 2.3C). BSA was released completely after approximately 75-90 min, coinciding with wafer disintegration.

The results of fluorescein and BSA release kinetics from pure CMC, 1:1, and pure ALG wafers were fit using four models for drug release – first order, Higuchi, Hixson-Crowell, and Korsmeyer-Peppas [92]. Fluorescein release data were best fit by the first order model (Table 2.3, Figure 2.4), whereas BSA release kinetics data were best fit by the Hixson-Crowell model (Table 2.4, Figure 2.5).

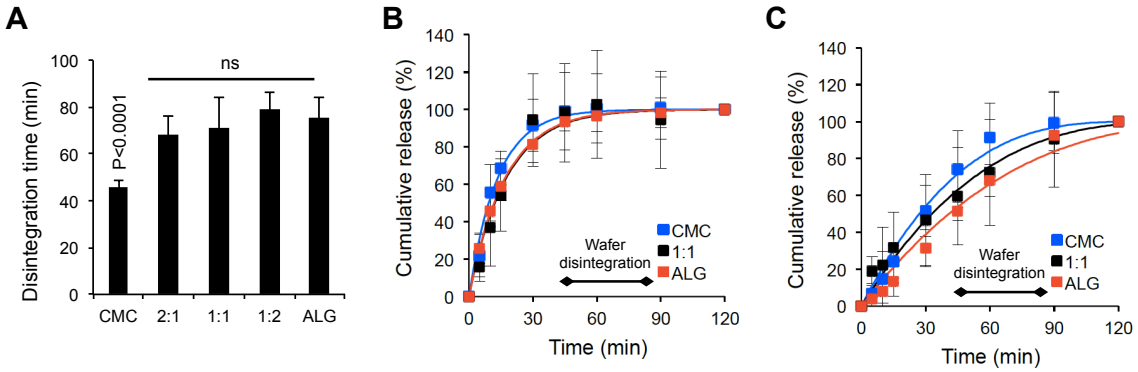

Figure 2.3 Disintegration time of mucoadhesive wafers and release kinetics of model compounds. (A) Average time of wafer disintegration in simulated saliva. (B) Release kinetics of fluorescein and (C) BSA in simulated saliva at 25 ºC. Data are shown as mean ± SD. (A) ANOVA and Tukey HSD test, n=14-18, ns: no significant difference among wafers containing ALG. (B) n=16, data fit with a first-order kinetic model. (C) n=8, data fit with the Hixson-Crowell model [92].

Table 2.3 Release kinetics of fluorescein fit with four mathematical models (First-Order, Higuchi, Hixson-Crowell, Korsmeyer-Peppas). Highlighted column indicates the model that best fits the data.

	First-Order $F = 100(1 - e^{-K_1 t})$		Higuchi $F = 100K_H t^{1/2}$		Hixson-Crowell $F = 100[1 - (1 - K_{HC}t)^3]$		Korsmeyer-Peppas $F = 100K_{KP}t^n$		
Wafer Composition (CMC:ALG)	K_1 (95% CI)	R^2	K_H (95% CI)	R^2	K_{HC} (95% CI)	R^2	K_{KP} (95% CI)	n (95% CI)	R^2
CMC	0.07458 (0.06543 – 0.08520)	0.9903	0.1196 (0.09637 – 0.1428)	0.7355	0.01291 (0.01044 – 0.01454)	0.8742	0.2920 (0.1515 – 0.4992)	0.2846 (0.1465 – 0.4417)	0.8903
1:1	0.05744 (0.04604 – 0.07204)	0.9706	0.1154 (0.09349 – 0.1372)	0.7925	0.01252 (0.01071 – 0.01384)	0.9473	0.2158 (0.08494 – 0.4404)	0.3494 (0.1680 – 0.5673)	0.8528
ALG	0.05895 (0.05719 – 0.06078)	0.9994	0.1141 (0.09648 – 0.1316)	0.8348	0.01242 (0.01064 – 0.01371)	0.9449	0.2418 (0.1434 – 0.3772)	0.3188 (0.2066 – 0.4439)	0.9360

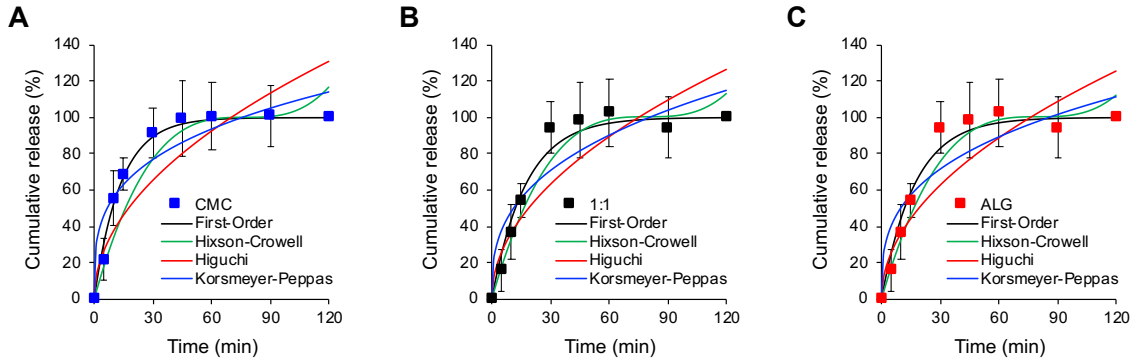

Figure 2.4 Release kinetics of fluorescein fit with four mathematical models (First-Order, Higuchi, Hixson-Crowell, Korsmeyer-Peppas). Data are shown as mean±SD (n=16). Wafer composition: (A) pure CMC, (B) CMC:ALG = 1:1, (C) pure ALG.

Table 2.4 Release kinetics of BSA fit with four mathematical models (First-Order, Higuchi, Hixson-Crowell, Korsmeyer-Peppas). Highlighted column indicates the model that best fits the data.

	First-Order $F = 100(1 - e^{-K_1 t})$		Higuchi $F = 100K_H t^{1/2}$		Hixson-Crowell $F = 100[1 - (1 - K_{HC}t)^3]$		Korsmeyer-Peppas $F = 100K_{KP}t^n$		
Wafer Composition (CMC:ALG)	K_1 (95% CI)	R^2	K_H (95% CI)	R^2	K_{HC} (95% CI)	R^2	K_{KP} (95% CI)	n (95% CI)	R^2
CMC	0.02728 (0.02212 – 0.03380)	0.9676	0.09809 (0.08410 – 0.1121)	0.9183	0.00763 (0.00674 – 0.00864)	0.9869	0.06288 (0.02267 – 0.1389)	0.6057 (0.4177 – 0.8357)	0.9338
1:1	0.02298 (0.02010 – 0.02633)	0.9827	0.09083 (0.08678 – 0.09489)	0.9901	0.00627 (0.00552 – 0.00714)	0.9810	0.07012 (0.05657 – 0.08578)	0.5616 (0.5143 – 0.6113)	0.9958
ALG	0.01776 (0.01394 – 0.02259)	0.9488	0.08274 (0.06693 – 0.09854)	0.8825	0.00505 (0.00435 – 0.00587)	0.9754	0.02004 (0.00863 – 0.04043)	0.8336 (0.6737 – 1.021)	0.9768

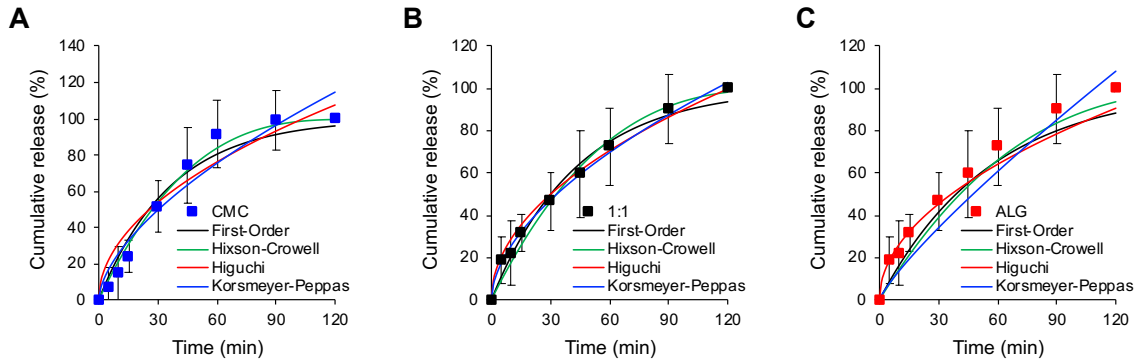

Figure 2.5 Release kinetics of BSA fit with four mathematical models (First-Order, Higuchi, Hixson-Crowell, Korsmeyer-Peppas). Data are shown as mean±SD (n=8). Wafer composition: (A) pure CMC, (B) CMC:ALG = 1:1, (C) pure ALG.

2.3.3 Strength and energetics of mucoadhesion

Fresh porcine sublingual mucosal tissue was used to evaluate the mucoadhesive strength of polymer wafers with various compositions. A typical stress-displacement curve (Figure 2.6A) shows an initial increase in stress due to elastic stretching of the mucosal tissue to which the wafer remained attached. As the wafer started to be peeled off the mucosal surface, stress eventually decreased to zero when the wafer detached completely from the mucosal surface. Wafers of higher CMC content showed higher σ_{max} (Figure 2.6B), whereas mixed CMC/ALG content tend to have higher W_{ad} (Figure 2.6C). The brittle pure CMC wafers fractured prior to separation from the mucosal tissue; however, the other wafer compositions elongated elastically before peeling away from the tissue and did not fracture.

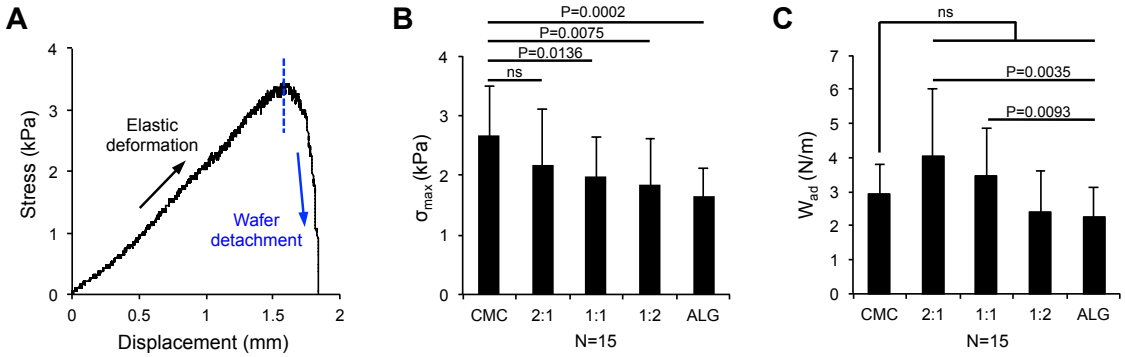

Figure 2.6 Mucoadhesive properties of the wafers. The wafers were attached to the surface of porcine sublingual mucosa wet by simulated saliva and tensile tests were performed at room temperature. (A) Representative stress-displacement of wafer detaching from mucosal surface. (B) Maximum detachment stress (σ_{max}). (C) Work of adhesion per unit area (W_{ad}), calculated as area under the stress-displacement curve. Data are shown as mean ± SD (n=15). ANOVA with Tukey HSD test, ns: not significant.

2.3.4 Permeation into sublingual mucosa

Porcine sublingual mucosa tissue was used to assess the permeation of fluorescently labeled BSA (Rh-BSA, 0.3 mg per wafer) delivered either via mucoadhesive wafers or as

aqueous buffered solution (0.3 mg per dose). First, the free protein solution created a localized, somewhat diffusive stain on the mucosal surface, but later it was completely washed away by water (Figure 2.7A).

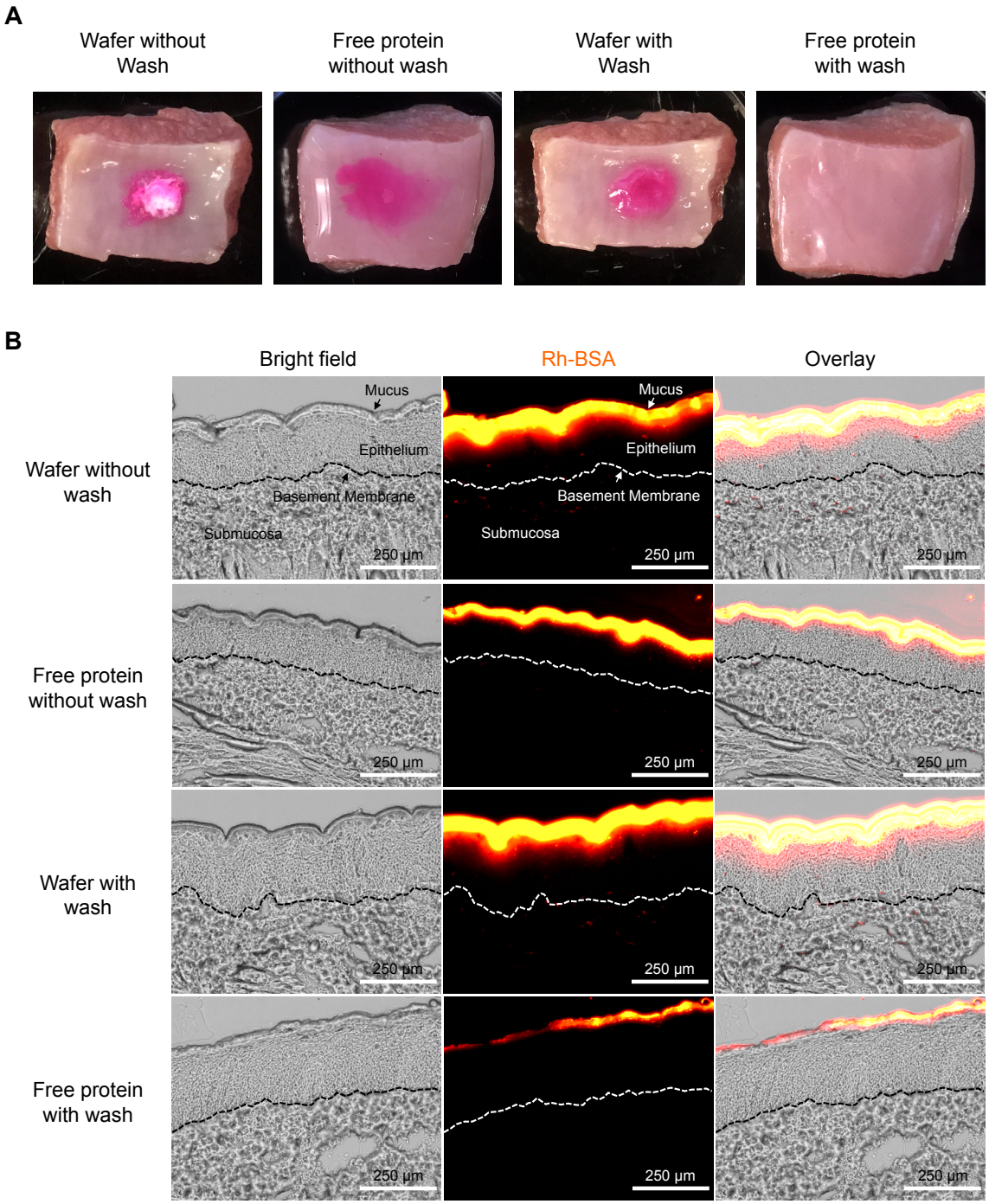

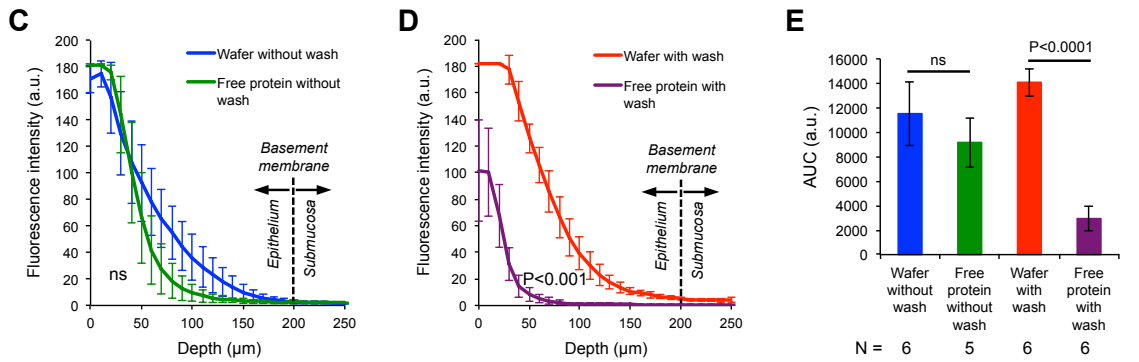

Figure 2.7 Mucoadhesive wafers prevent saliva wash-out and enhance permeation of model protein into porcine sublingual mucosa. (A) Surface of sublingual mucosa after washing with 10 mL of deionized water for 20 sec. (B) Representative fluorescence microscopy images of Rh-BSA permeation into sublingual mucosa. (C, D) Fluorescence intensity of Rh-BSA at various depths beneath the tissue surface. (E) Total amount of Rh-BSA present in the sublingual mucosa. Data are shown as mean ± SD (n=5-6 tissue slices). (C-D) Holm-Sidak t-test, α=0.05, (E) One-way ANOVA and Tukey HSD test, ns: not significant.

In contrast, the wafer adhered strongly to the mucosal surface and maintained high local protein concentration despite water wash. Next, the Rh-BSA was allowed to permeate into the sublingual mucosa for 2 h, at which time the tissue was sectioned and imaged. Representative fluorescent micrographs revealed that the 1:1 wafers yielded much greater depth of Rh-BSA permeation into the sublingual mucosa in comparison with free protein solution (Figure 2.7B). As expected, wafers with higher ALG concentration (1:2 and pure ALG) could not remain adhered to the mucosal tissue during washing. Quantification of the fluorescence intensity (Figure 2.7C-E) reveals that wafer-delivered Rh-BSA permeated to depths greater than 200 μm, beyond the 100-200 μm thick epithelium, even under the condition mimicking wash-out [93].

2.3.5 Preservation of protein activity

To assess the protein stabilization capabilities, β-galactosidase (β-gal) was loaded into the polymer wafers and the enzyme activity was quantified and compared with that of the free β-gal dissolved in buffer. Fresh fully active β-gal had an activity of 484 units/mg

solid (Figure 2.8A). One unit will hydrolyze 1.0 µmol of the substrate ONPG per minute at pH 7.3 and 37 ºC. First, fresh β-gal was dissolved in various polymer aqueous solutions and the enzyme activity was measured. There was minimal but statistically significant effect on β-gal activity by CMC and ALG in aqueous solutions (Figure 2.8A). Next, β-gal activity was determined after lyophilization of the enzyme in the presence or absence of various polymer blends. As expected, lyophilization of free β-gal resulted in a 22.5% reduction in activity (Figure 2.8B). Surprisingly, β-gal in pure CMC wafers had a ~80% reduction in activity. In contrast, β-gal in wafers containing various amounts of ALG (especially 1:1 and 1:2 CMC:ALG ratios) appeared to remain fully active (Figure 2.8B). Finally, the various wafer formulations and free protein solids were treated at 75 ºC for 30 min. As expected, free unprotected β-gal lost 60% of the initial activity due to heat challenge (Figure 2.8C). Again, the pure CMC wafers caused β-gal to lose nearly 95% of its initial activity. In contrast, the 1:1 and pure ALG wafers preserved nearly 70% of the initial β-gal activity.

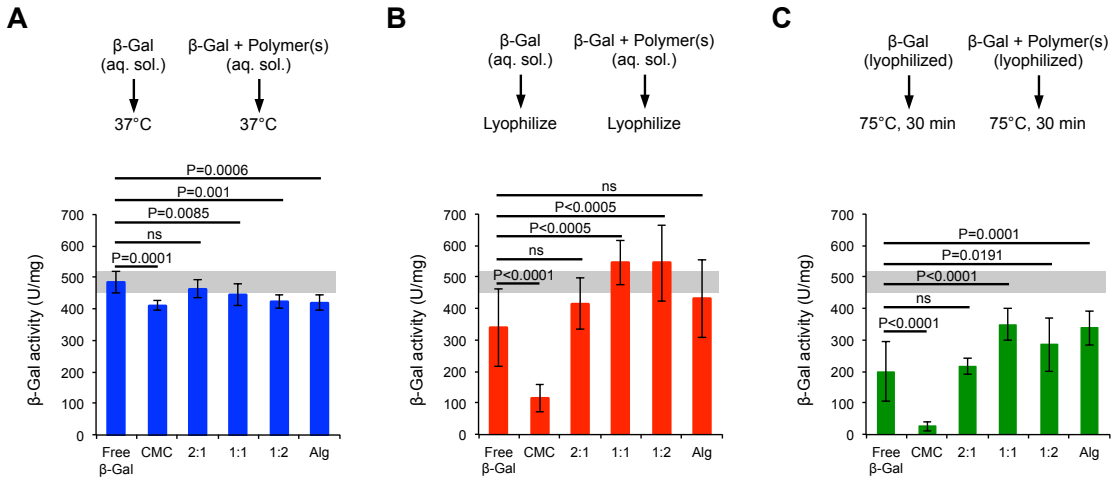

Figure 2.8 Mucoadhesive wafers protect β-Galactosidase (β-gal) from deactivation due to lyophilization and heat challenge. Enzyme activity was measured (A) prior to lyophilization, (B) after lyophilization (reconstitution in 100 mM PBS, pH 7.3), and (C) after lyophilization and heat challenge (75 ºC for 30 min). Data are shown as mean ± SD (n=6-18). ANOVA with Tukey HSD test, ns: not significant. Grey shaded area indicates the range of activity of free enzyme in buffer without lyophilization or heat challenge.

2.3.6 Vaccine efficacy in vivo

Mice were immunized by the sublingual route with HIV gp140 protein, which was formulated as freshly thawed aqueous solution or in polymer wafers of 1:1 CMC:ALG ratio. In the lungs, polymer wafer delivery of gp140 appeared to generate greater T cell response (136 SFU/2 × 10^5 cells) to the fresh gp140 liquid solution (57 SFU/2 × 10^5 cells), although the difference was not statistically significant (Figure 2.9A).

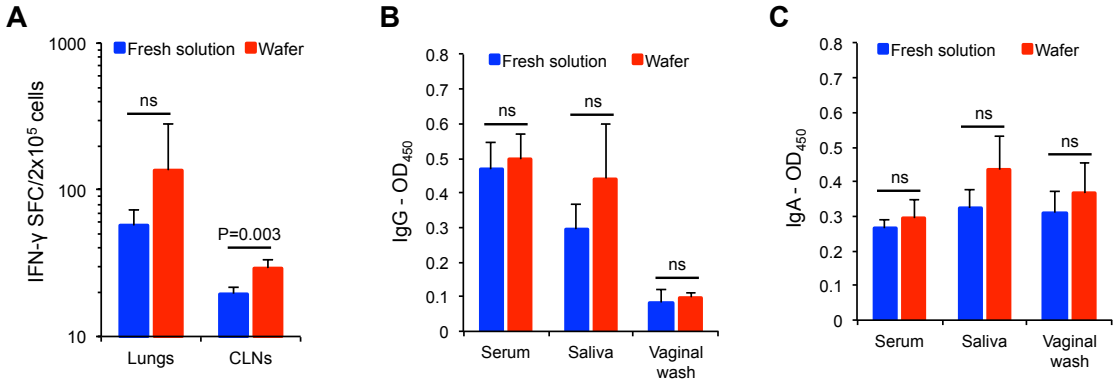

Figure 2.9 Mucoadhesive wafers achieve equal or better immune responses to an HIV gp140 vaccine after sublingual delivery in mice. (A) IFN-γ (by ELISPOT). (B) IgG and (C) IgA (by ELISA, serum samples diluted 1:100; mucosal secretions diluted 1:5). Mice were vaccinated sublingually with 5 µg of gp140 protein either as fresh solution in buffer or as wafer after storage at room temperature for one week. All mice were also given 2 µg of αGalCer sublingually as adjuvant. Two immunizations were given on days 0 and 7. Mice were sacrificed on day 14. Data shown are mean ± SD (n=5). Two-tailed t-test, ns: not significant.

In the CLNs, polymer wafers generated greater T cell response (29 SFU/2 × 10^5 cells) than the fresh liquid solution (20 SFU/2 × 10^5 cells). Antibody responses were evaluated by measuring anti-gp140 IgG and IgA in the blood, saliva, and vaginal washes of immunized animals. Polymer wafers and fresh liquid solution were equally potent in inducing systemic antibody responses, as IgG antibody levels in serum, saliva, and vaginal washes were comparable for both formulations (Figure 2.9B). Similar results were seen in the mucosal antibody response, as IgA antibody levels in serum, saliva, and

vaginal washes were comparable between groups immunized by polymer wafers and fresh liquid solution (Figure 2.9C).

2.4 Discussion

The sublingual mucosa is an attractive site of vaccination for the development of robust mucosal immunity against many pathogens [94–96]. Mucoadhesive formulations have been used widely to deliver small molecules across the oral mucosa, including in some commercial products [97,98]. In contrast, the oral mucosal delivery of macromolecules (including protein and nucleic acid-based antigens and adjuvants) has been much less successful. A wide variety of mucoadhesive polymers, such as chitosan, cellulose derivatives, poly(acrylic acid), guar or other gums, polyvinyl alcohol, and polyvinylpyrrolidone, are available for use in sublingual drug formulations [84]. However, the compositions of sublingual drug products are often complex. The selection of appropriate mucoadhesive polymers is largely based on trial and error and thus lacking of rational design. Furthermore, most mucoadhesive formulations of proteins do not address the important issue of preserving protein stability against excess heat and lyophilization.

The motivation of this study is to address the unmet need for a simple sublingual vaccine delivery system capable of both enhancing vaccine delivery efficiency through mucoadhesion and protecting bioactive protein antigens from environmental damage without the cold chain. We focused on binary blends of CMC and ALG, two biopolymers with excellent record of safety in human use. Our rationale is that each polymer would have a primary function, providing either strong mucoadhesion or protein stabilization,

and that adjusting the ratio of the two would allow optimization of the overall performance of the delivery system (Figure 2.1).

CMC is an anionic derivative of cellulose and highly soluble in water [99]. Similar to cellulose, CMC is primarily a crystalline polymer (crystallinity index ~80%) [100]. At low degrees of substitution (DS < 1.0), molecular association between the unsubstituted regions of the CMC chains form crystalline regions with a similar structure to cellulose [101]. CMC is a widely used excipient for oral drug formulation and has been shown to exhibit good mucoadhesive properties [102,103] resulting from extensive physical entanglement and hydrogen bonding between the CMC chains and mucin [104], a main component of the mucosal surfaces [105]. ALG is another natural anionic polysaccharide and has been used in a range of drug delivery applications. A linear copolymer, ALG consists of homopolymeric regions of 1,4′-linked β-D-mannuronic and α-L-guluronic acid blocks [106]. Unlike CMC, ALG is a semi-crystalline with a typical crystallinity index of 30% [107]. While ALG was reported to be somewhat mucoadhesive [84], its primary purpose here is to stabilize proteins through a number of mechanisms [82] and to form mechanically robust films [108].

We developed a simple yet robust process of lyophilizing binary blends of CMC and ALG with a range of mass ratios to form porous wafers. Hundreds of wafers were prepared using this method to achieve high consistency with regard to wafer diameter, thickness and weight (Table 2.1). The only outliers were wafers made of pure CMC; they were smaller in diameter and appeared shrunken with large pores (Figure 2.2A). Microstructural analysis shows that pure CMC wafers had large pores with thick strands, whereas increasing ALG content made the pores smaller and strands smoother (Figure

2.2B). Formation of these microstructures is likely due to the different degrees of crystallinity between CMC and ALG. During freezing the highly crystalline CMC may have phase-separated from water, allowing large ice crystals to form [109]. The subsequent sublimation of the ice crystals would leave behind the large pores seen in the CMC wafers. In contrast, the amorphous ALG chains are more flexible and mobile, allowing them to entangle and form more extensive networks [110]. These networks may have prevented ice crystal growth, resulting in much smaller pores after lyophilization. The network-forming capacity and low crystallinity of ALG can also explain the observation that wafers with increasing ALG content were less strong but more elastic (Table 2.2) and that the pure CMC wafers were brittle and difficult to handle.

Interestingly, the pure CMC wafers did not display the optimal mucoadhesive behavior, although it was chosen primarily for its mucoadhesive properties. While pure CMC wafers adhered most strongly, as shown by the highest σ_{max} (Figure 2.6B), wafers with moderate ALG content (2:1 and 1:1) had the largest W_{ad} (Figure 2.6C). The elasticity of the ALG-containing wafers enabled them to deform and peel away from the porcine mucosal tissue under tension (Figure 2.6A), contributing to the greater W_{ad}, whereas the pure CMC wafers fractured prior to detachment. While 1:1 wafers remained adhered to the sublingual mucosal tissue during extensive washing, wafers with higher ALG content (1:2 and pure ALG) could not withstand the wash and detached from the tissue. This is likely due to the lower work of adhesion (W_{ad}) of wafers with high ALG content (Figure 2.6C). These results clearly demonstrate that a proper balance of mucoadhesive strength and mechanical cohesiveness, exemplified in wafers of

intermediate CMC:ALG ratios (such as the 1:1), is necessary for achieving the optimal performance in sublingual administration and the resistance to saliva wash-out.

Microstructural differences between CMC and ALG also affected the disintegration time of the wafers and the release kinetics of model compounds. The larger pores found in the CMC wafers may allow water to more quickly hydrate the polymer matrix, resulting in significantly faster disintegration of the wafers (Figure 2.3A). The release mechanisms of fluorescein and BSA are notably different. A first-order model best fit the fluorescein release kinetics (Table 2.3, Figure 2.4). This suggests that fluorescein release was primarily diffusion dependent. The observation that fluorescein was 100% released from all wafer compositions prior to complete disintegration of the wafers can be explained by the fact that fluorescein, a highly soluble small molecule, may diffuse quickly upon hydration in the simulated saliva. On the other hand, the release kinetics of BSA was best fit by the Hixson-Crowell cube root law (Table 2.4, Figure 2.5), suggesting that BSA release is more dependent on wafer disintegration and less on diffusion. This mechanism is also consistent with the observation that complete release of BSA was achieved only after the wafers had completely disintegrated. The reliance on wafer disintegration may also explain the greater differences in BSA release kinetics among various wafer compositions (Figure 2.3C) as compared to the less significant differences in fluorescein release kinetics (Figure 2.3B).

The effective pore radius of the sublingual mucosal membrane has been estimated at 30–53 Å [111]. Therefore, many proteins, such as BSA (R_g ~ 30 Å) [112] and HIV gp140 (R_g ~ 42 Å) [113], can likely diffuse through the sublingual epithelium, albeit very slowly. Mucoadhesive formulations may improve sublingual delivery of proteins by

providing sufficient time for these large molecules to diffuse into the tissue [67,71] as we have demonstrated here (Figure 2.7). Even during extensive washing with a large volume of water, the wafers of 1:1 CMC:ALG ratio remained adhered to the mucosal tissue. Over the course of 2 h, BSA delivered via the wafers was found inside the tissue at depths greater than 200 μm, within and beyond the 100 – 200 μm thick epithelium, whereas BSA delivered as aqueous solution never reached beyond 100 μm (Figure 2.7C,D). Therefore, with the help of these wafers, it is expected that protein antigens of similar size would reach the APCs within the epithelium and the underlying submucosa, eliciting antigen-specific immune responses.

To preserve vaccine potency during lyophilization and storage, numerous excipients have been investigated to stabilize proteins against heating, freezing and dehydration [114]. Here we have shown that although both CMC and ALG are highly hydrophilic and have similar chemical features capable of hydrogen bonding, ALG was much effective than CMC in maintaining β-gal activity after lyophilization and heat challenge (Figure 2.8). Due to its high crystallinity, the CMC chains may be too sterically hindered to form sufficient hydrogen bonds with β-gal to maintain its native structure. In contrast, the amorphous ALG chains are more flexible and thus able to hydrogen bond with β-gal. Surprisingly, pure CMC wafers compromised β-gal activity beyond that of the unprotected free protein after lyophilization. Perhaps phase separation of the highly crystalline CMC domains during freezing may have caused β-gal to aggregate and lose activity.

We selected the 1:1 CMC:ALG blend as the optimal wafer composition after a balanced consideration of wafer mechanical robustness, mucoadhesive properties, and the

effectiveness of protein stabilization. This wafer composition was used to formulate a protein antigen, HIV gp140 protein. Wafer preparation was conducted at the University of Minnesota (Minneapolis, Minnesota) and shipped by air to MD Anderson Cancer Center (Houston, Texas) without refrigeration or desiccation. The wafers were then stored under ambient conditions for 5 days prior to sublingual immunization of mice. When compared to a freshly thawed liquid gp140 solution, the wafer vaccine generated comparable cell-mediated and antibody-mediated responses (Figure 2.9). T-cell response in the lungs were equally generated by the wafers and fresh liquid solutions. In the CLNs, greater T-cell response was seen when gp140 was given via the mucoadhesive wafers. Equally potent antibody responses were seen in mice immunized by wafers or liquid solution, as anti-gp140 IgG and IgA levels in the blood, saliva, and vaginal washes of both groups were comparable. Taken together, these results demonstrate that the mucoadhesive wafers of 1:1 binary composition is an effective sublingual protein vaccine formulation, capable of eliminating the need for cold-chain during storage and transportation and eliciting antigen-specific immune responses equal to or better than liquid protein formulation. Future studies on these binary polymer wafers will involve sublingual testing in larger animal models without anesthesia, in which case the anticipated advantage of mucoadhesive wafers over liquid formulation is expected to be more prominent considering saliva wash-out and swallowing. Another future opportunity is the co-encapsulation and controlled release of both antigen and immunostimulatory adjuvant using the same wafer formulation.

2.5 Conclusions

We have prepared and characterized porous wafers consisting of blends of two biocompatible polymers – CMC and ALG – through a simple and robust process. Wafers with high CMC content was highly mucoadhesive to sublingual mucosal tissue and could withstand extensive washing, leading to improved protein permeation into the tissue. Wafers with high ALG content were not only mechanically robust, but also able to preserve the activity of a model enzyme from potential damage due to lyophilization and excessive heat. HIV gp140 protein encapsulated in wafers of the optimal composition (CMC:ALG ratio = 1:1) could be stored and transported without cold chain and maintained antigen-specific immunogenicity after sublingual vaccination in mice. These findings established that the CMC:ALG binary blend polymer wafers have the potential to improve the delivery and storage stability of sublingual protein-based vaccines.

Chapter 3 Enhancing Polyplex-Mediated Gene Delivery in vitro by Polyvinyl Alcohol Wafers

3.1 Introduction

Nucleic acid-based therapeutics, or "gene therapy", has the potential to treat numerous diseases, such as cancer, neurodegenerative diseases, infectious diseases, and genetic disorders [115]. Gene therapy involves delivering DNA or RNA to replace or knockdown genes in target cells [37]. For gene therapy to be effective, an efficient carrier for the delivery of the genetic material is required [35]. While viral vectors have been shown to be efficient gene delivery systems, they have a limited genetic payload and can be difficult to produce in commercially relevant quantities [116,117]. Additionally, their potential safety concerns, such as immunogenicity and oncogenicity, have limited their clinical applications [36]. Consequently, the development of nonviral gene delivery systems has gained significant interest [118].

While intramuscular injection of naked plasmid DNA (pDNA) can produce detectable amounts of proteins in skeletal muscle, naked pDNA-based gene therapy has a low delivery efficiency, and as a result, low therapeutic effect [119]. Over 98% of injected pDNA has been shown to be degraded by extracellular nucleases or removed from the muscle within minutes after administration [120]. Numerous synthetic carriers have been developed to improve the delivery efficiency of pDNA. Many are based on cationic polymers which condense the negatively charged pDNA via electrostatic interactions to form "polyplexes." Polyplexes can protect pDNA from nuclease degradation and facilitate cellular uptake [35]. Among the cationic polymers, polyethyleneimine (PEI) is the most commonly used polymer to form polyplexes for gene delivery [33]. The

repeating amine structure gives PEI a large positive charge density, which allows it to produce compact and tightly bound complexes with pDNA and electrostatically interact with negative charged cell membranes [36]. In addition, the substantial secondary and tertiary amines in branched PEI are thought to facilitate escape from endocytic vesicle via the "proton-sponge" mechanism [121], a crucial step in efficient gene delivery.

Despite the high transfection efficiency of PEI polyplex-mediated gene delivery demonstrated in serum-free in vitro conditions, PEI polyplexes perform poorly in the presence of serum, limiting their efficacy in vivo [36]. Serum contains various negatively charged proteins that adsorb onto polyplexes, which can lead to polyplex aggregation, polyplex unpackaging, and reduced uptake by endocytosis [35]. In addition, various components of the extracellular matrix have been shown to bind to or unpackage polyplexes [34]. Many approaches have been investigated to reduce serum protein adsorption onto polyplexes to improve transfection efficiency in the presence of serum, including PEGylation [34], succinylation of PEI to form zwitterion-like polyplexes [36], covalently attaching polyvinyl alcohol (PVA) to PEI [35], and embedding polyplexes into PVA hydrogels [37,38].

The objective of the present study is use polymer wafers to enhance polyplex-mediated transfection in serum free and 10% serum conditions in vitro. The wafers were composed of different water-soluble polymers – carboxymethylcellulose (CMC), alginate (ALG), polyvinyl alcohol (PVA), hydroxypropyl cellulose (HPC), polyethylene oxide (PEO), or polyvinylpyrrolidone (PVP). Polyplexes encoding for green fluorescent protein (GFP) were loaded into the polymer wafers by a simple and robust process. Transfection efficiency of mouse fibroblast cells (NIH/3T3) was visualized with fluorescence

microscopy and quantified by flow cytometry. Lastly, the importance of the physical form of PVA in facilitating high transfection efficiency, especially in 10% serum containing medium, was investigated.

3.2 Materials and Methods

3.2.1 Chemicals and reagents

Polyvinyl alcohol (PVA, 88 mol% hydrolyzed, MW 25 kDa, Polydispersity ~1.9) was purchased from Polysciences (Warrington, PA). Hydroxypropyl cellulose (HPC, average M_w ~100 kDa), polyvinylpyrrolidone (PVP, average M_w 360 kDa), polyethylene oxide (PEO, average M_v 600 kDa), polyethyleinime (PEI, branched, average M_w ~25 kDa by LS, average M_n ~10 kDa by GPC), paraformaldehyde, and bovine serum albumin (BSA) were purchased from Millipore Sigma (Burlington, MA). Green fluorescent protein (GFP) plasmid DNA (pEGFP-N1, 1 mg/mL in water) and Luciferase (Luc) luciferase (pCMV-Luc, 1 mg/mL in water) were purchased from Elim Biopharm (Hayward, CA). Dulbecco's modified eagle medium (DMEM), fetal bovine serum (FBS), Penicillin-Streptomycin (10,000 U/mL; 10,000 μg/mL), L-glutamine (200 mM), phosphate buffered saline (PBS, pH 7.4), sodium pyruvate (100 mM), trypsin-EDTA (0.25%), trypan blue (0.4% solution, 0.85% NaCl), HEPES buffer (1 M), Live Cell Imaging Solution (LCIS), NucBlue Live ReadyProbes Reagent (Hoechst 33342), sodium azide, MTT (3-(4,5-dimethylthiazol- 2-yl)-2,5-diphenyltetrazolium bromide) (MTT), and dimethyl sulfoxide (DMSO) were purchased from Thermo Fisher Scientific (Waltham, MA).

3.2.2 Preparation of PEI/DNA polyplexes

PEI/DNA polyplexes with N/P ratio 8 or 11 were prepared by adding 1 mL of PEI solution (N/P: 8, 82.5 μg/mL in 20 mM HEPES buffer; N/P: 11, 112 μg/mL in 20 mM

HEPES buffer) to 1 mL of DNA plasmid solution (80 μg/mL in 20 mM HEPES buffer). Solutions were vortexed for 10 sec and incubated at room temperature (protected from light) for 30 minutes.

3.2.3 Preparation of blank and polyplex-loaded polymer wafers

Aqueous stock solutions of CMC, ALG, CMC:ALG (1:1 wt:wt), PVA, HPC, PEO, or PVP were prepared by dissolving the appropriate amounts of the polymers in deionized water at a concentration of 2.5% (w/v). The solutions were briefly heated at 60ºC to facilitate complete dissolution of the polymers. To prepare blank wafers, aliquots of 100 μL of the polymer solutions were dispensed in 96-well flat-bottom plates, frozen at -80ºC overnight and lyophilized under 0.020 mBar for 72 h in a FreeZone® Freeze Dry System (Labconco, Kansas City, MO) equipped with a Maxima™ C Plus Vacuum Pump (Model M8c, Fisher Scientific). After drying, the wafers were carefully removed from the wells and compressed to ~0.5 mm thick by applying a constant force of 30 pounds for 5 sec. The same protocol was used to prepare polymer wafers containing naked plasmid DNA (2 μg DNA) or PEI/DNA polyplexes (2 μg DNA, N/P: 8 or 11). The cargo solutions (50 μL) were added to and mixed with the polymer solutions (100 μL) before lyophilization. All the wafers were stored under ambient conditions (protected from light) without desiccation.

3.2.4 Cell culture

Mouse fibroblast cell line NIH/3T3 was obtained from ATCC. NIH/3T3 cells were cultured in a medium consisting of DMEM with 4.5 g/L glucose, 4 mM L-glutamine, 110 mg/L sodium pyruvate, 3.7 g/L sodium bicarbonate, 10% heat inactivated fetal bovine serum (FBS), 100 U/mL penicillin, and 100 μg/mL streptomycin. NIH/3T3 cells were

cultured in tissue culture flasks and incubated in a humidified environment at 37ºC with 5% CO_2. When cells reached ~80% confluency the culture medium was removed, cells were rinsed with PBS, and 0.25% trypsin-EDTA was added for 5 min to detach cells from the flasks. Harvested cells were centrifuged at 200 x *g* for 5 min and supernatant was discarded. Cell pellets were resuspended in cell culture medium and a 100 µL aliquot was stained 1:1 with trypan blue 0.4% solution and counted using a hemocytometer and inverted microscope. Cell suspensions were split 1:3 to 1:6 to continue culture or diluted to the appropriate seeding density for subsequent experiments.

3.2.5 Transfection efficiency of NIH/3T3 cells

Harvested NIH/3T3 cells were diluted to density of 50,000 cells/mL and plated in 12-well plates (50,000 cells/well). Cells were incubated in a humidified environment at 37ºC with 5% CO_2 overnight (~18-24 h). Prior to transfection, the culture medium was removed, the cells were washed twice with 1 mL PBS, and the culture medium was replaced with 1 mL serum free or 10% serum containing media. Cells were transfected PEI/DNA polyplexes (2 µg DNA, N/P: 8 or 11). Polyplexes were given to cells in different delivery vehicles – polyplexes alone (in 50 µL HEPES buffer, 20 mM), polyplex-loaded polymer wafers, polyplex mixed in polymer solutions (without lyophilization), or polyplex-loaded polymer wafers reconstituted in 1 mL serum free or 10% serum containing media (prior to transfection). After 4 h incubation in a humidified environment at 37ºC with 5% CO_2, transfection media was removed, the cells were washed twice with 1 mL PBS, and the transfection media was replaced with 1 mL fresh cell culture medium. Cells were incubated in a humidified environment at 37ºC with 5%

CO_2 overnight for 24 h or 48 h, after which transfection efficiency was analyzed with fluorescence microscopy and flow cytometry.

Prior to fluorescence imaging, culture medium was removed, cells were washed twice with 1 mL PBS, and the medium was replaced with 1 mL LCIS. Cell nuclei were stained with Hoechst 33342 by adding 2 drops of NucBlue Live ReadyProbes Reagent to each dish followed by incubation in a humidified environment at 37ºC with 5% CO_2 for 20 min. Phase contrast and fluorescent images of NIH/3T3 cells were acquired with an Olympus IX70 inverted microscope equipped with an Olympus plan fluorite 20XPH/0.45 NA objective, an Olympus DP72 camera, and an X-Cite 120 Wide-Field Fluorescence Microscope Excitation Light Source (Excelitas Technologies, Waltham, MA). Hoechst 33342-stained cell nuclei were visualized using an excitation wavelength of 350 ± 50 nm and emission wavelength of 460 ± 50 nm. GFP+ cells were visualized using an excitation wavelength of 480 ± 40 nm and emission wavelength of 535 ± 50 nm. Exposure times were chosen to minimize autofluorescence. Images were analyzed in ImageJ.

Prior to quantifying transfection efficiency with flow cytometry, culture medium was removed and cells were detached from the wells with 200 µL 0.25% trypsin-EDTA. After 5 min incubation, cells were washed with 1 mL FACS buffer (PBS pH 7.4, 1% BSA, 0.05% sodium azide), collected in FACS tubes (12 x 75 plastic culture tubes; Thermo Fisher Scientific, Waltham, MA), and fixed with 2% paraformaldehyde for 20 min. After fixation, cells were centrifuged to pellet, washed with 1 mL FACS buffer, and resuspended in 0.5 mL FACS buffer. Cells were stored at 4ºC (protected from light) until use. Analysis of 30,000 cells was done using a BD Accuri C6 flow cytometer (BD Biosciences, San Jose, CA). Data was analyzed FlowJo, version 10.7.1 (Ashland, OR).

Transfection efficiency was determined by quantifying the percentage of GFP+ cells and the mean fluorescence intensity (MFI) of GFP+ cells. The GFP+ gate was drawn based on cells transfected with Luc polyplexes delivered by equivalent vehicle (i.e., Luc polyplex alone, Luc polyplex-loaded wafer, Luc polyplex mixed in polymer solution, reconstituted Luc polyplex-loaded wafer). The false positive frequency was restricted to 0.2%.

3.2.6 Biocompatibility of PEI/DNA polyplexes

Harvested NIH/3T3 cells were diluted to density of 50,000 cells/mL and plated in 12-well plates (50,000 cells/well). Cells were incubated in a humidified environment at 37ºC with 5% CO_2 overnight (~18-24 h). Cells were transfected with PEI/DNA polyplexes as described above in serum free or 10% serum containing media for 4 h. Transfection media was removed, cells were washed twice with 1 mL PBS, and the transfection media was replaced with 1 mL fresh cell culture medium (without phenol red). After 24 h incubation in a humidified environment at 37ºC with 5% CO_2, cell viability was evaluated using an MTT (3-(4,5-dimethyl-thiazol-2-yl)-2,5-diphenyl tetrazolium bromide) assay [122]. To each well, 100 µL MTT solution (5 mg/mL in PBS) was added. After 4 h incubation in a humidified environment at 37ºC with 5% CO_2, 850 µL medium was removed from each well. Formazan crystals were dissolved in 500 µL DMSO and absorbance was measured at 540 nm and corrected for blank media background using a BioTek Cytation 3 Cell Imaging Multi-Mode Reader BioTek Instruments, Winooski, VT). Cell viability was determined by normalizing by the absorbance of untreated cells.

3.2.7 Measurement of PEI/DNA polyplex diameter by dynamic light scattering (DLS)

PEI/DNA polyplexes (4 μg DNA, N/P: 8 or 11) were added to 2 mL serum free or 10% serum containing media in 12 well plates and incubated in a humidified environment at 37ºC with 5% CO_2 for 4 h. At particular time points, 1.5 mL was sampled and transferred to semi-micro cuvettes (Thermo Fisher Scientific, Waltham, MA). The effective diameter and half width of the polyplexes were measured using a Brookhaven 90Plus Particle Size Analyzer (15 mW laser, 658 nm incident beam, 90% scattering angle; Brookhaven Instruments, Holtsville, NY).

3.2.8 Statistical analysis

ANOVA and Tukey HSD test for multiple comparisons were used to determine the significance of difference in GFP+, MFI, and cell viability between different treatment groups. All analyses were performed using GraphPad prism, version 9.0.0 (GraphPad software Inc., San Diego, California, USA).

3.3 Results

3.3.1 Transfection by polyplexes loaded into anionic polymer wafers

Polyplexes (N/P: 11) were loaded into polymer wafers composed of the anionic polymers CMC, ALG, or 1:1 CMC:ALG ratio. The transfection of NIH/3T3 cells in serum free medium by polyplex-loaded anionic polymer wafers was visualized with fluorescence microscopy 24 h or 48 h post transfection (Figure 3.1). While a moderate amount of cells fluoresced green after transfection by polyplexes alone, none of the cells that were transfected with polyplex-loaded CMC, polyplex-loaded ALG wafers, or polyplex-loaded 1:1 CMC:ALG wafers displayed any green fluorescence.

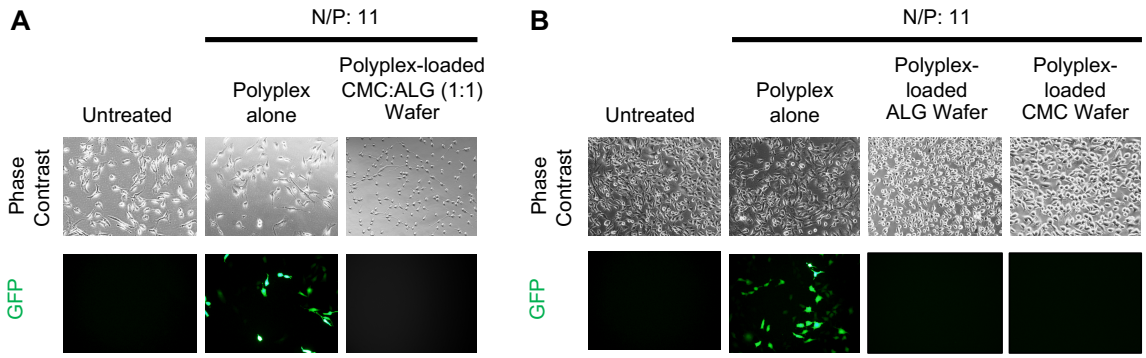

Figure 3.1 Representative fluorescence microscopy images of NIH/3T3 cells transfected by polyplex-loaded anionic polymer wafers in serum free medium. Polyplexes were prepared with N/P: 11. Cells were transfected for 4 h and fluorescently imaged after (A) 24 h or (B) 48 h incubation.

3.3.2 Transfection by polyplexes loaded into nonionic polymer wafers

Polyplexes (N/P: 8) were loaded into polymer wafers composed of the nonionic polymers PVA, HPC, PEO, or PVP. The transfection efficiency of NIH/3T3 cells in serum free or 10% serum containing media by these polyplex-loaded wafers was quantified by flow cytometry 24 h post transfection (Figure 3.2). In serum free medium, there was an overall shift of the cell populations into the GFP+ gate, especially when cells were transfected by polyplexes alone or polyplex-loaded PVA wafers (Figure 3.2A).

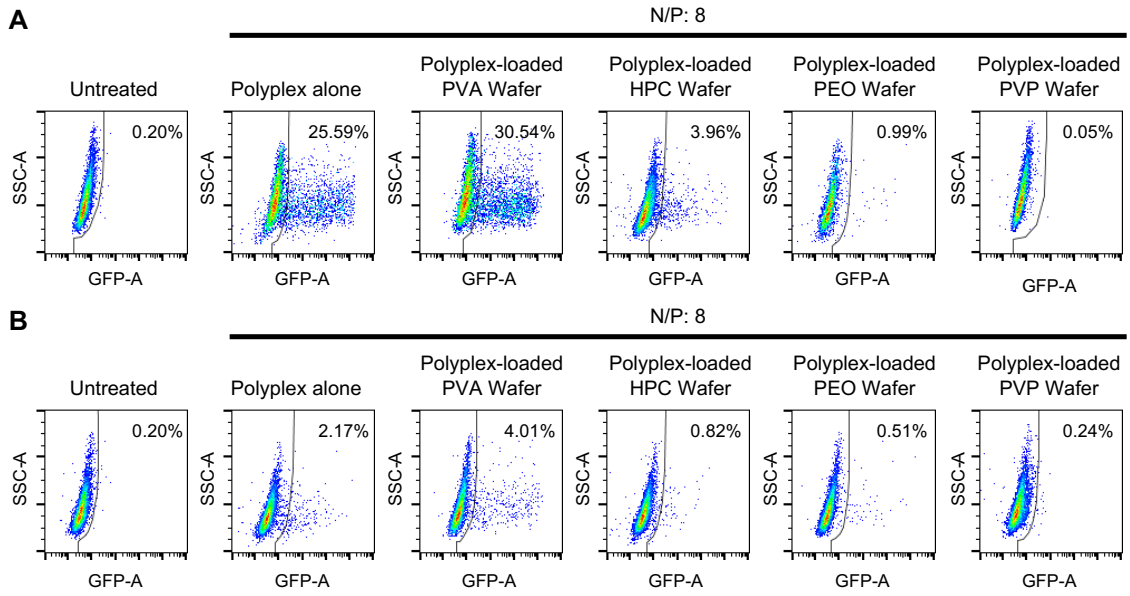

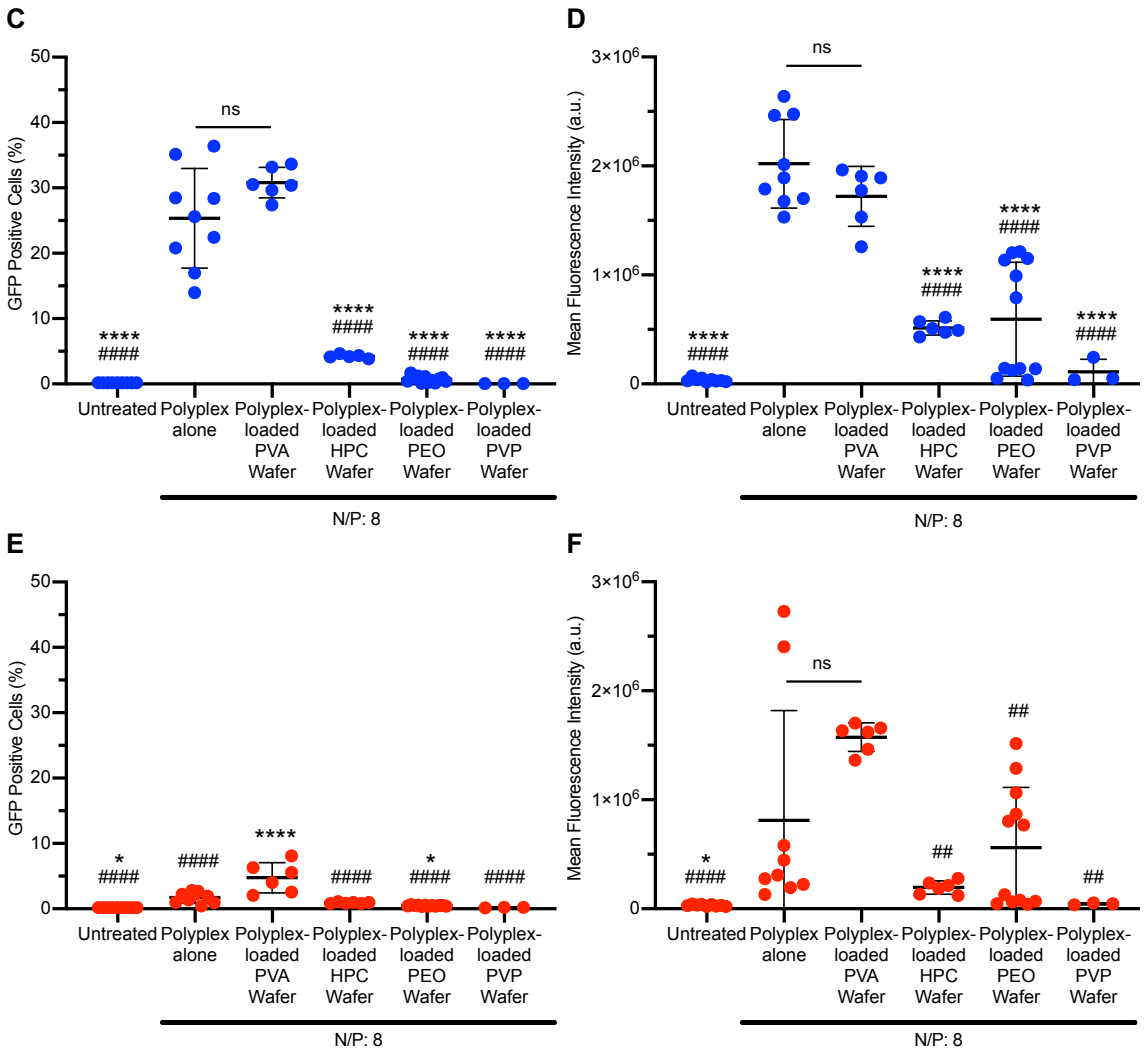

Figure 3.2 Transfection efficiency of polyplex-loaded wafers in NIH/3T3 cells. Polyplexes were prepared with N/P: 8. Cells were transfected for 4 h and fixed after 24 h incubation with 2% paraformaldehyde. Representative flow cytometry dot plots of cells transfected in (A) serum free or (B) 10% serum containing media. (C) Percentage of GFP+ cells and (D) MFI of GFP+ cells after transfection in serum free medium. (E) Percentage of GFP+ cells and (F) MFI of GFP+ cells after transfection in 10% serum containing medium. Data are shown as mean ± SD (dots represent individual replicates) (n = 3 – 12). ANOVA with Tukey HSD test (* $p < 0.05$, **** $p < 0.0001$ vs polyplex alone; # $p < 0.05$, ## $p < 0.01$, #### $p < 0.0001$ vs polyplex-loaded PVA wafer).

While it appeared that a slightly greater percentage of cells were GFP+ after transfection by polyplex-loaded PVA wafers (30.8% GFP+) as compared to cells transfected by polyplexes alone (25.4% GFP+), this result was not statistically significant ($p = 0.0628$) (Figure 3.2C). The MFI of GFP+ cells transfected by polyplexes alone or

polyplex-loaded PVA wafers were also not statistically significantly different ($p = 0.5876$) (Figure 3.2D). However, transfection by the other polyplex-loaded wafers was significantly worse. Only 4.2%, 0.7%, and 0.1% of cells were GFP+ after transfection by polyplex-loaded HPC, PEO, and PVP wafers, respectively (Figure 3.2C). In addition, the MFI of the few GFP+ cells transfected by these polyplex-loaded wafers was also quite low (Figure 3.2D).

As expected, transfection efficiency was much worse in 10% serum containing medium. There was a much less dramatic shift of the cell populations into the GFP+ gate (Figure 3.2B). Only 1.7% of cells were GFP+ after transfection by polyplexes alone; however, 4.8% of the cells were GFP+ after transfection polyplex-loaded PVA wafers (Figure 3.2E). While this is still a low transfection efficiency, this increase was statistically significant ($p < 0.0001$). For cells transfected by the other polyplex-loaded wafers, less than 1% of cells were GFP+. While it appears that the MFI of GFP+ cells transfected by polyplex-loaded PVA wafers is greater than the MFI of GFP+ cells transfected by polyplexes alone, the large variability in the MFI of cells transfected by polyplexes alone renders this difference statistically insignificant ($p = 0.1067$) (Figure 3.2F).

Trying to increase the transfection efficiency, polyplexes were prepared with a higher N/P ratio (N/P: 11) and loaded into polymer wafers composed of PVA, HPC, PEO, or PVP. The transfection of NIH/3T3 cells in serum free medium by these polyplex-loaded wafers visualized with fluorescence microscopy 48 h post transfection (Figure 3.3). A moderate fraction of cells fluoresced green after transfection by polyplexes alone; however, it appeared that transfection by polyplex-loaded PVA wafers resulted in a

greater amount of green fluorescing cells. While some cells transfected by polyplex-loaded HPC wafers expressed green fluorescence, transfection by polyplex-loaded PEO or PVP wafers resulted in little to no green fluorescing cells.

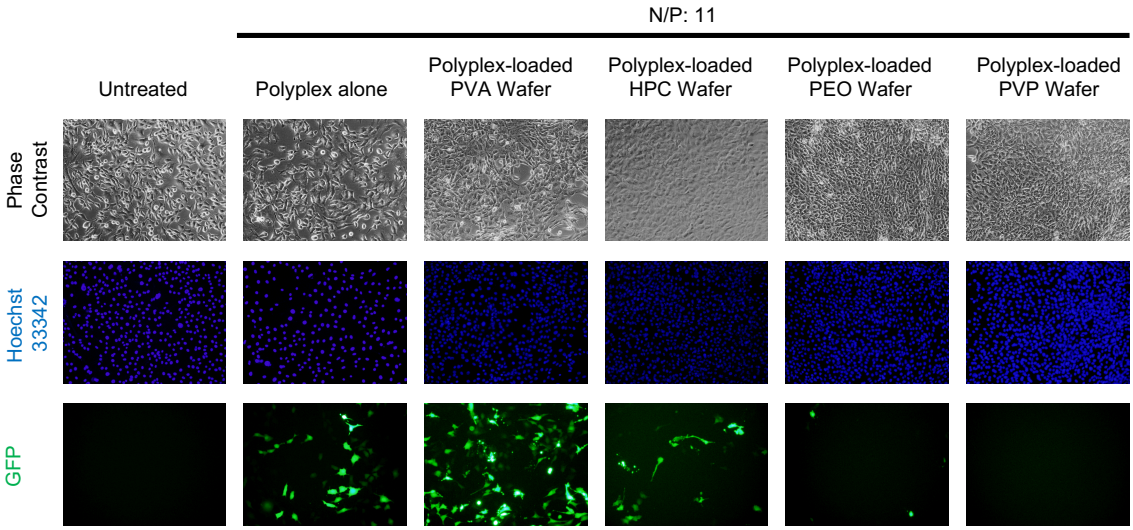

Figure 3.3 Representative fluorescence microscopy images of NIH/3T3 cells transfected by polyplex-loaded wafers in serum free medium. Polyplexes were prepared with N/P: 11. Cells were transfected for 4 h and fluorescently imaged after 48 h incubation.

3.3.3 Transfection by polyplexes mixed in aqueous polymer solutions

To examine how the physical form of the nonionic polymers effects the polyplex-mediated transfection, polyplexes (N/P: 11) were mixed into aqueous solutions (2.5% w/v) of PVA, HPC, PEO, or PVP. The transfection of NIH/3T3 cells in serum free or 10% serum containing media by polyplexes mixed in these solutions was visualized with fluorescence microscopy 48 h post transfection (Figure 3.4). In serum free medium, a similar trend was seen as cells transfected by polyplex-loaded wafers; however, for all of the polymers, fewer cells fluoresced green after transfection by polyplexes mixed in the polymer solutions (Figure 3.4A). In 10% serum containing medium, transfection by polyplexes mixed in the polymer solutions was poor (Figure 3.4B). While a few cells expressed green fluorescence after transfection by polyplexes mixed in PVA solution,

transfection by polyplexes mixed in HPC, PEO, or PVP solution resulted in little to no green fluorescing cells.

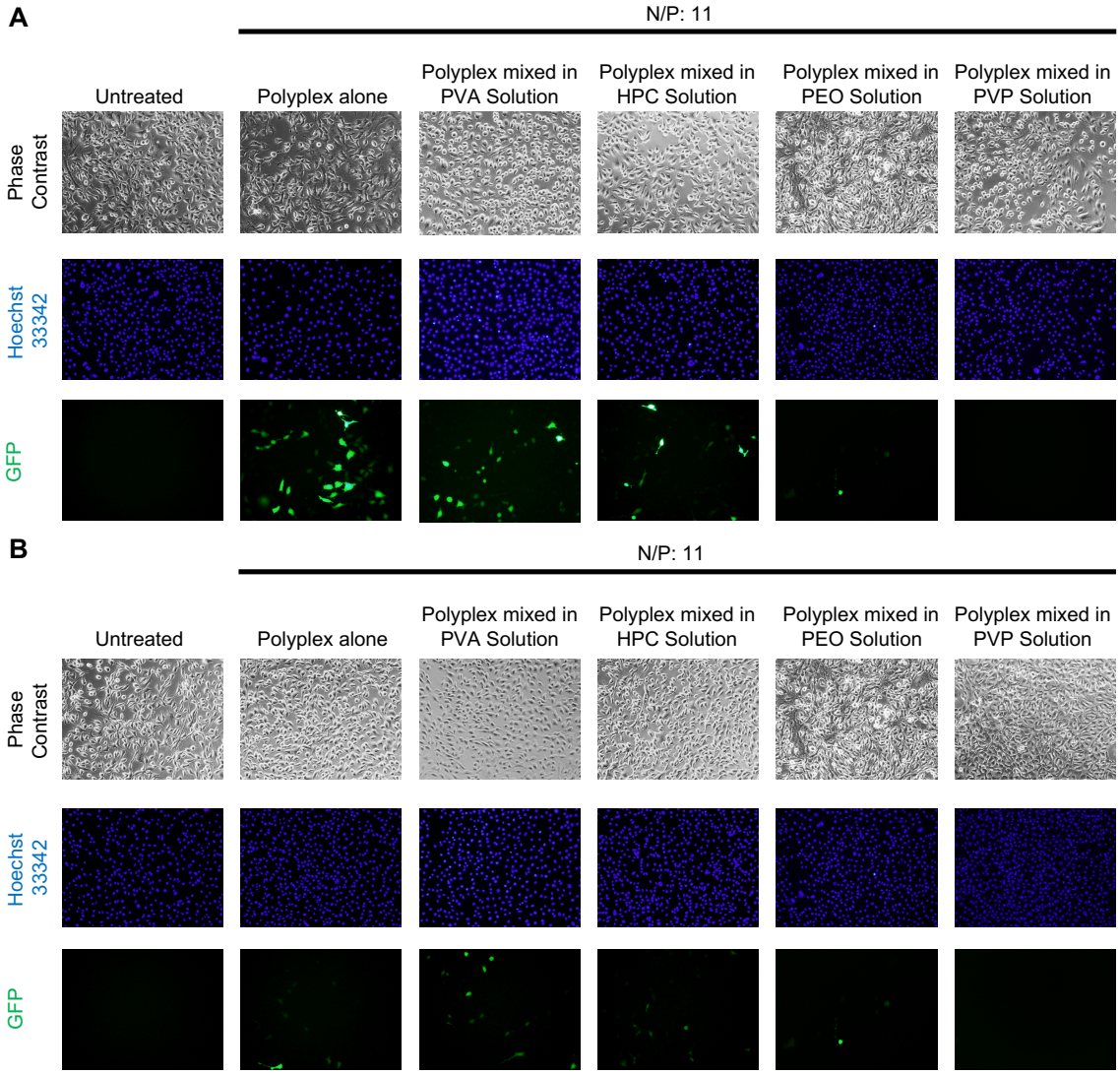

Figure 3.4 Representative fluorescence microscopy images of NIH/3T3 cells transfected by polyplexes mixed in polymer solutions in (A) serum free or (B) 10% serum containing media. Polyplexes were prepared with N/P: 11. Cells were transfected for 4 h and fluorescently imaged after 48 h incubation.

3.3.4 Polyplexes delivered by different physical forms of PVA

To examine how the physical form of PVA effects the polyplex-mediated transfection, polyplexes (N/P: 11) were delivered to NIH/3T3 cells in serum free or 10% serum containing media by different physical forms of PVA. Transfection was visualized

with fluorescence microscopy 48 h post transfection (Figure 3.5). In serum free medium, many cells expressed green fluorescence after transfection by polyplex-loaded PVA wafers; however, fewer cells appeared to express green fluorescence after transfection by polyplexes mixed in PVA solution (Figure 3.5A). Adding polyplexes alone alongside a blank PVA wafer also transfected fewer cells than polyplex-loaded PVA wafers.

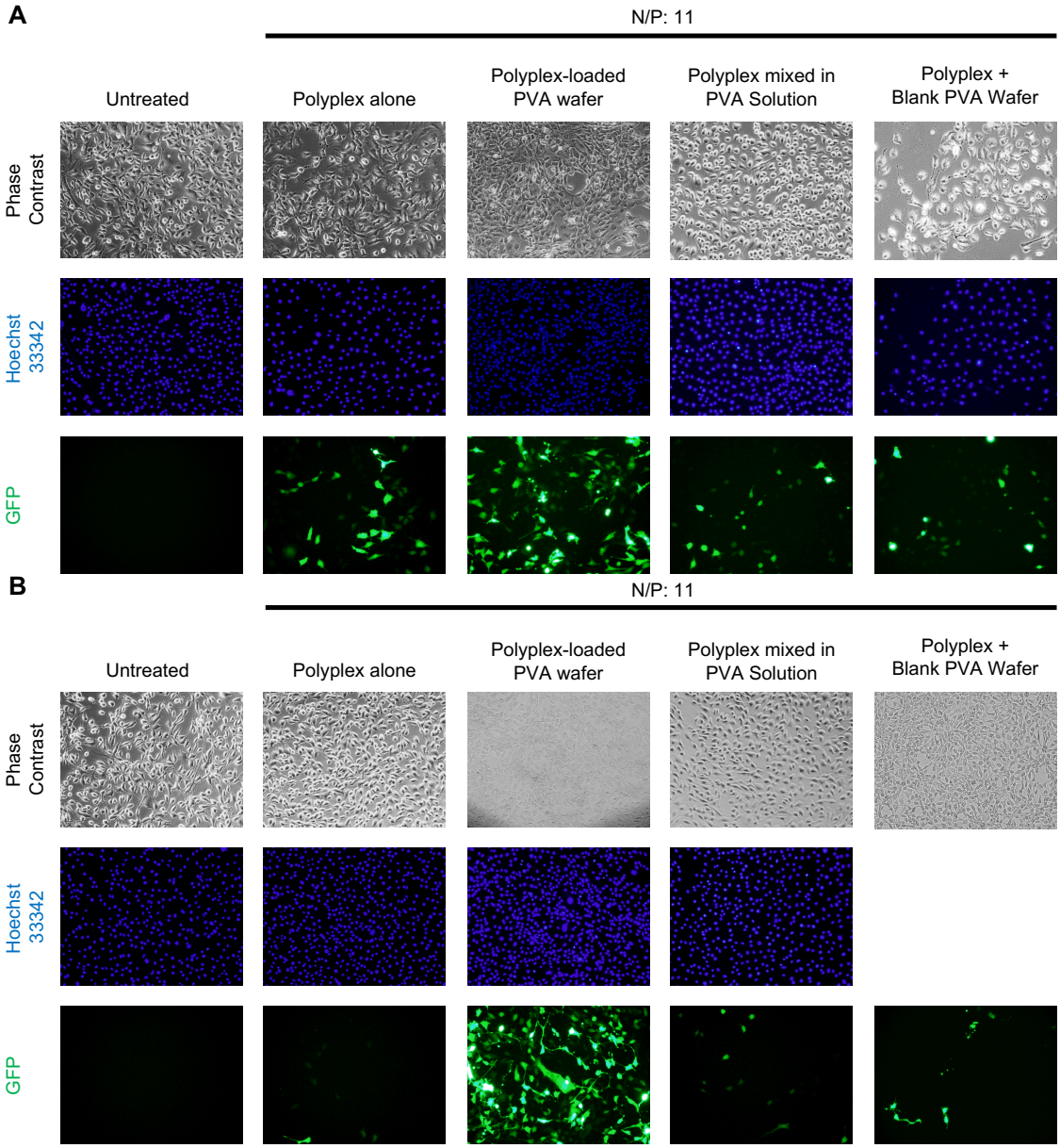

Figure 3.5 Representative fluorescence microscopy images of NIH/3T3 cells transfected by polyplexes in different physical forms of PVA in (A) serum free or (B) 10% serum containing media. Polyplexes were prepared with N/P: 11. Cells were transfected for 4 h and fluorescently imaged after 48 h incubation.

In 10% serum containing medium, the differences in transfection by polyplexes in different physical forms of PVA is even more obvious. Many cells brightly fluoresced green after transfection by polyplex-loaded PVA wafers (Figure 3.5B). In contrast, very few cells expressed green fluorescence after transfection by polyplexes alone, polyplexes mixed in PVA solution, or polyplexes alone alongside a blank PVA wafer.

The quantification of transfection efficiency by flow cytometry (Figure 3.6) was in agreement with the fluorescence microscopy images. In addition to polyplex-loaded PVA wafers and polyplexes mixed in PVA solution, polyplex-loaded PVA wafers were reconstituted in serum free or 10% serum containing media prior to transfection. In serum free medium, there was an overall shift of the cell populations into the GFP+ gate; however, this shift was greater in cells transfected by polyplexes alone or polyplex-loaded PVA wafers (Figure 3.6A).

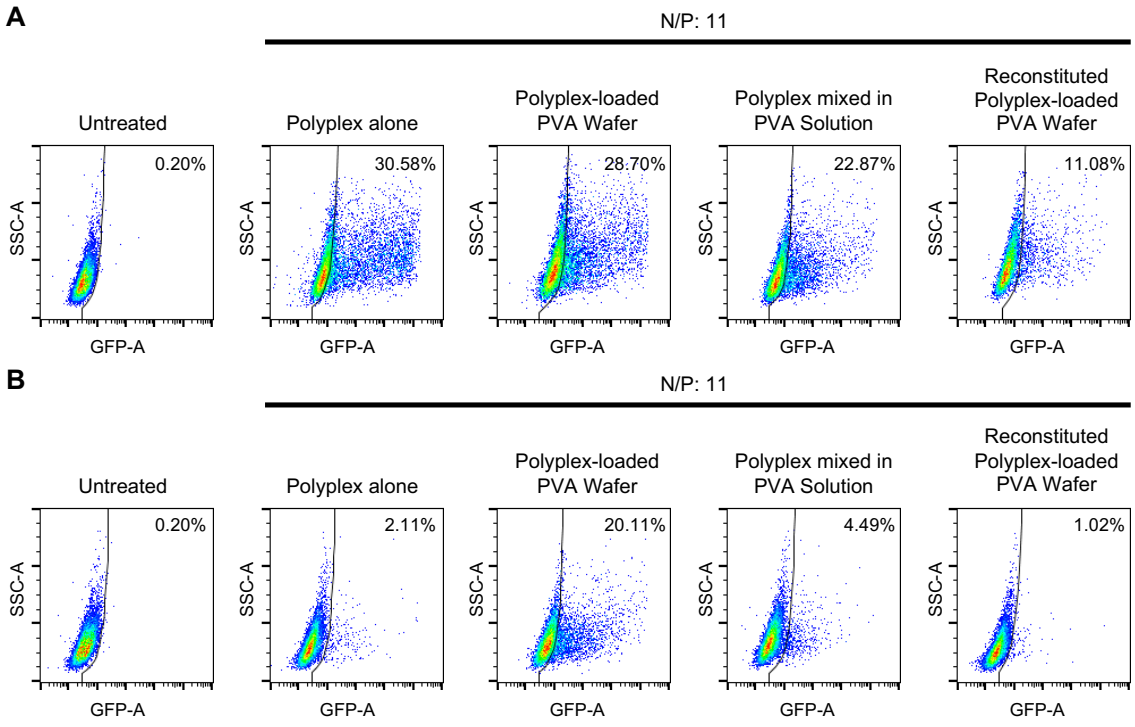

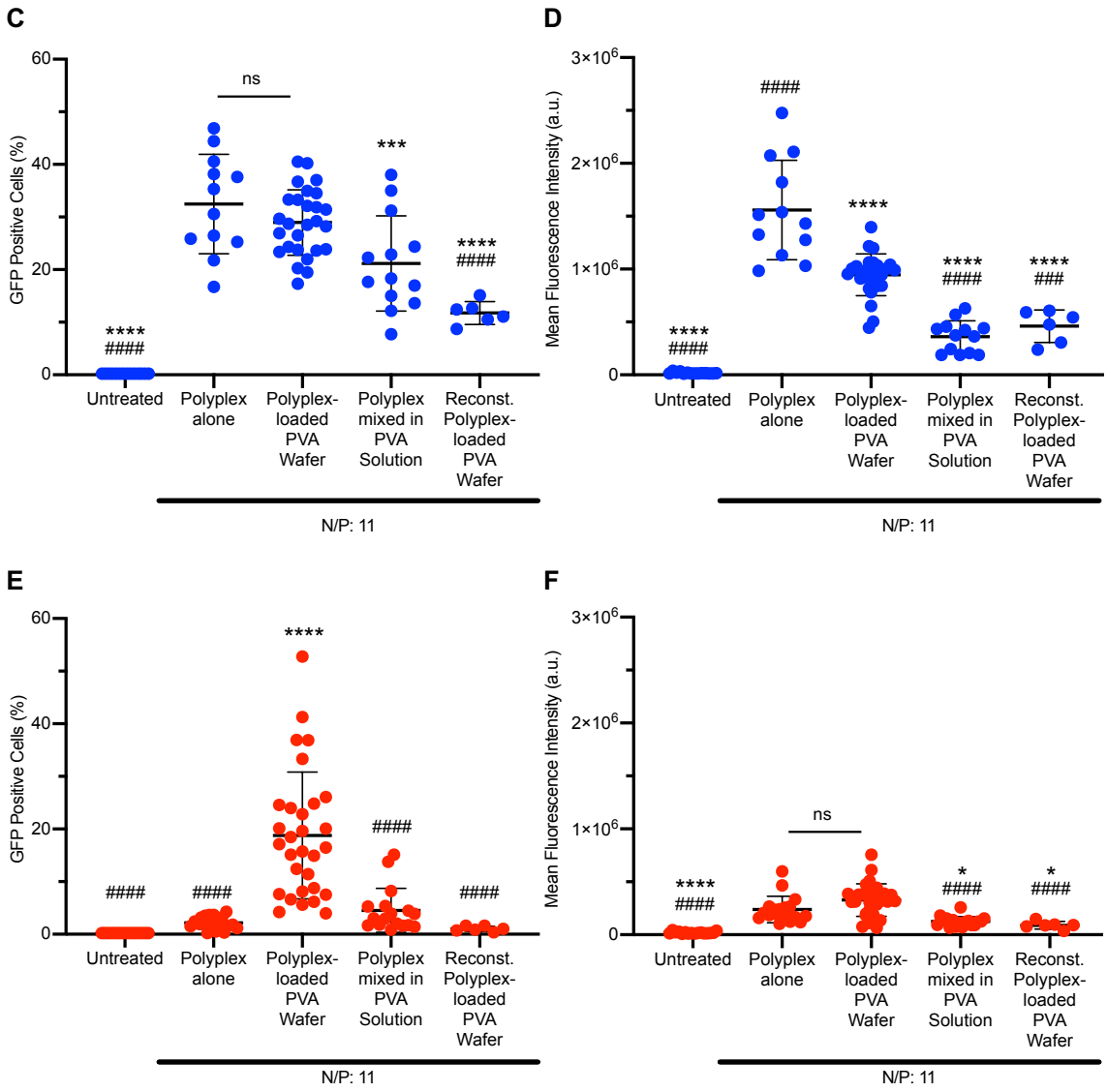

Figure 3.6 Transfection efficiency of polyplexes delivered by different physical forms of PVA in NIH/3T3 cells. Polyplexes were prepared with N/P: 11. Cells were transfected for 4 h and fixed after 48 h incubation with 2% paraformaldehyde. Representative flow cytometry dot plots of cells transfected in (A) serum free of (B) 10% serum containing media. (C) Percentage of GFP+ cells and (D) MFI of GFP+ cells after transfection in serum free medium. (E) Percentage of GFP+ cells and (F) MFI of GFP+ cells after transfection in 10% serum containing medium. Data are shown as mean ± SD (dots represent individual replicates) (n = 6 – 30). ANOVA with Tukey HSD test (* $p < 0.05$, *** $p < 0.001$, **** $p < 0.0001$ vs polyplex alone; ### $p < 0.001$, #### $p < 0.0001$ vs polyplex-loaded PVA wafer).

Approximately 30% of cells were GFP+ after transfection by polyplexes alone or polyplex-loaded PVA wafers; however, only 21.2% and 11.8% of cells were GFP+ after transfection by polyplexes mixed in PVA solution and reconstituted polyplex-loaded

PVA wafers, respectively (Figure 3.6C). Although the percentage of GFP+ cells transfected was similar, the MFI was lower in GFP+ cells transfected by polyplex-loaded PVA wafers was lower than GFP+ cells transfected by polyplexes alone ($p < 0.0001$) (Figure 3.6D).

In 10% serum, transfection efficiency was significantly higher in cells transfected by polyplex-loaded PVA wafers. A very low percentage of cells transfected by polyplexes alone, polyplexes mixed in PVA solution, or reconstituted polyplex-loaded PVA wafers shifted into the GFP+ gate (Figure 3.6B). Strikingly, nearly 20% of cells were GFP+ after transfection by polyplex-loaded PVA wafers, as compared to only 2.2% GFP+ cells after transfection by polyplexes alone (Figure 3.6E). For a few experimental replicates, between 37-53% of the cells were GFP+ when transfected by polyplex-loaded PVA wafers. Interestingly, the high transfection efficiency was completely lost if the polyplex-loaded PVA wafers were reconstituted in 10% serum containing medium prior to transfection. Only 1.1% of cells were GFP+ after transfection by reconstituted polyplex-loaded PVA wafers. While there was a small increase in MFI of the GFP+ cells transfected by polyplex-loaded PVA wafers as compared to GFP+ cells transfected by polyplexes alone, this result was not statistically significant ($p = 0.0582$) (Figure 3.6F).

3.3.5 Biocompatibility of polyplex-loaded polymer wafers

The biocompatibility of blank wafers and polyplex-loaded wafers was evaluated by exposing NIH/3T3 cells to the wafers for 4 h in serum free or 10% serum containing media. Cell viability was measured after 24 h incubation by an MTT assay (Figure 3.7). In serum free medium, blank HPC, PEO, and PVP wafers displayed no cytotoxicity (Figure 3.7A). When polyplexes (N/P: 8) alone were given, cell viability decreased

31.4%. Polyplex-loaded HPC and polyplex-loaded PVP wafers were also relatively cytotoxic, as 48% and 67.3% of cells were killed, respectively. While exposure to blank PVA wafers resulted in a 22.5% reduction in cell viability, loading polyplexes (N/P: 8) into PVA wafers did not generate any additional toxicity. Polyplex-loaded PEO wafers were similarly nontoxic as the blank PEO wafers. Similar trends were seen in 10% serum medium with the exception of polyplexes (N/P: 8) alone, which did not display any cytotoxicity (Figure 3.7B). While there was an approximately 27% decrease in cell viabilities, there was again no difference between cells exposed to blank PVA and polyplex-loaded PVA wafers.

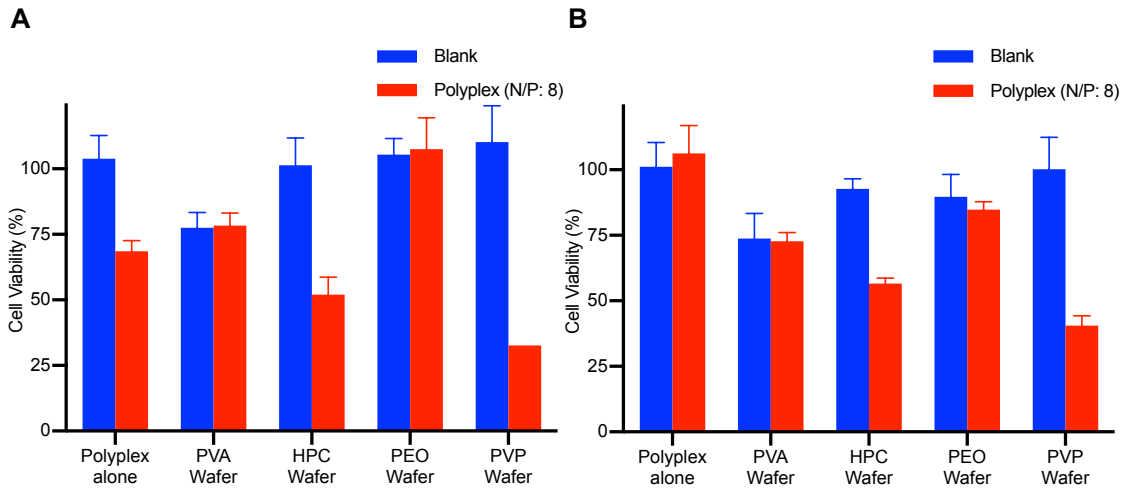

Figure 3.7 NIH/3T3 cell viability after exposure to blank or polyplex-loaded wafers in (A) serum free or (B) 10% serum containing media. Polyplexes were prepared with N/P: 8. Cells were exposed for 4 h and cell viability was measured by MTT assay after 24 h incubation. Data are shown as mean ± SD (n = 4 – 8).

The biocompatibility of different physical forms of PVA was also evaluated. NIH/3T3 cells were exposed to the physical forms of PVA for 4 h in serum free or 10% serum containing media. Cell viability was measured after 24 h incubation by an MTT assay (Figure 3.8). In serum free medium, it was interesting to note that although blank PVA wafers elicited a 22.5% reduction in cell viability, blank PVA solution and

reconstituted blank PVA wafers exhibited no toxicity (Figure 3.8A). While loading naked DNA into any of the physical forms of PVA did not increase toxicity, polyplex (N/P: 11)-loaded PVA was more toxic than the different physical forms of blank PVA. This was especially true in polyplex-loaded PVA wafers, where only 22.2% of cells remained viable. In 10% serum, PVA solution and reconstituted PVA wafers were mostly nontoxic. Regardless of the cargo, over 90% of cells remained viable after exposure to these physical forms of PVA (Figure 3.8B). PVA wafers were less toxic in 10% serum, as 73.8% and 63.0% of cells remained viable after exposure to blank PVA wafers and polyplex (N/P: 11)-loaded PVA wafers, respectively.

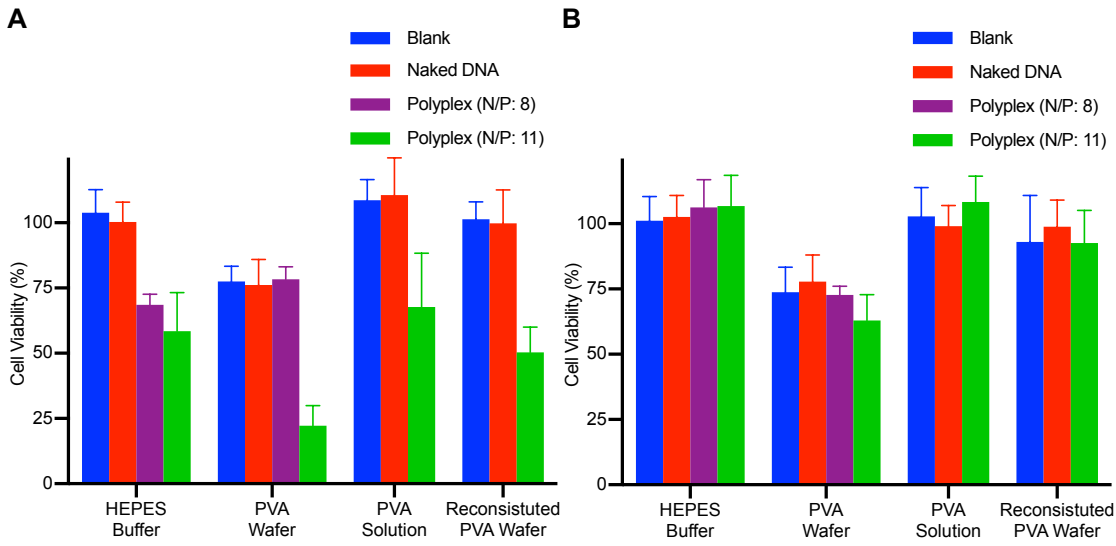

Figure 3.8 NIH/3T3 cell viability after exposure to blank or polyplexes in different physical forms of PVA in (A) serum free or (B) 10% serum containing media. Polyplexes were prepared with N/P: 11. Cells were exposed for 4 h and cell viability was measured by MTT assay after 24 h incubation. Data are shown as mean ± SD (n = 4 – 12).

3.3.6 Particle size of polyplexes released from nonionic polymer wafers

The effective diameter of polyplexes (N/P: 8 or 11) alone or polyplexes released from PVA, HPC, PEO, or PVP wafers in serum free or 10% serum containing media was measured by DLS (Figure 3.9). As it was not possible to measure the effective diameter of polyplexes in the wafers at time 0 because they had not yet been released, the

polyplexes released from the wafers were first measured at the 15 min timepoint. In serum free medium, polyplexes (N/P: 8) alone in buffer had initial effective diameter of 285.5 nm and aggregated to 792.8 nm after 4 h (Fig. 9A). Polyplexes (N/P: 8) released from PEO wafers also aggregated over time, up to 1067.5 nm after 4 h. In contrast, polyplexes (N/P: 8) released from PVA wafers were more colloidally stable with an effective diameter of approximately 150 nm throughout the entire 4 h. There was a slight decrease in effective diameter of polyplexes (N/P: 8) released from HPC wafers (297.8 nm at 15 min to 219.9 nm at 4 h) or PVP wafers (98.0 nm at 15 min to 78.5 nm at 4 h). Nearly identical trends were seen for polyplexes with N/P: 11 (Figure 3.9B).

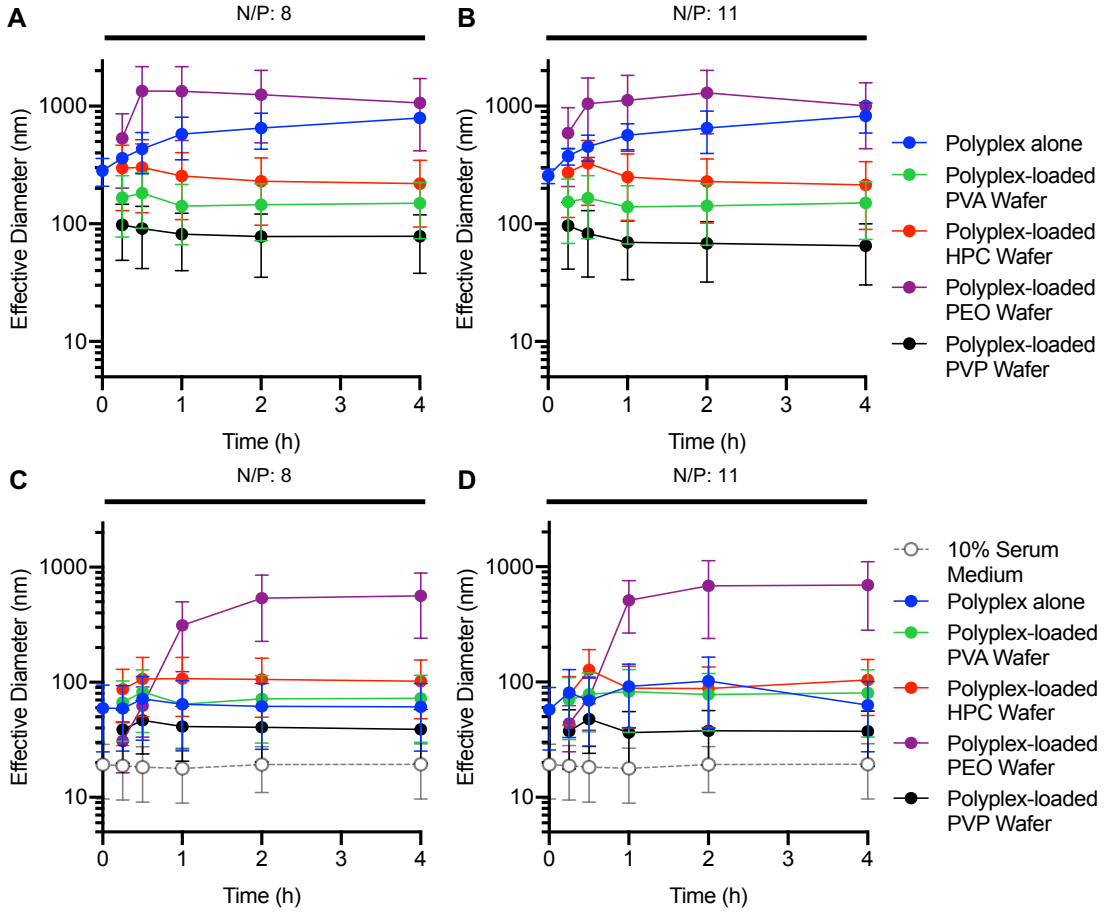

Figure 3.9 Size of polyplexes released from wafers in serum free medium with (A) N/P: 8 or (B) N/P: 11. Size of polyplexes released from wafers in 10% serum containing medium with (C) N/P: 8 or (D) N/P: 11. Data are shown as effective diameter ± half width as measured by DLS.

In general, smaller effective diameters were measured in 10% serum (Figure 3.9C,D). This is partially due to the presence of the serum proteins forming particles approximately 19 nm in diameter, which skews the data smaller. Unlike in serum free medium, polyplexes (N/P: 8) alone in buffer were relatively colloidally stable, with an effective diameter of approximately 60-70 nm over the 4 h (Figure 3.9C). Polyplexes (N/P: 8) released from PVA wafers were similarly sized, with an effective diameter of approximately 65-80 nm over the 4 h. While colloidally stable, polyplexes (N/P: 8) released from HPC wafers were slightly larger (~105 nm) whereas polyplexes (N/P: 8) released from PVP wafers were slightly smaller (~20 nm) than polyplexes (N/P: 8) alone in buffer. Again, nearly identical trends were seen for polyplexes with N/P: 11 in 10% serum (Figure 3.9D).

3.3.7 Particle size of polyplexes released from different physical forms of PVA

The effective diameter of polyplexes (N/P: 11) alone or released from different physical forms of PVA in serum free or 10% serum containing media was measured by DLS (Figure 3.10). In serum free medium, there was little difference in effective diameter of polyplexes released from the PVA forms (Figure 3.10A). Polyplexes released from PVA wafers or reconstituted PVA wafers were approximately 150 nm at all time points. Polyplexes mixed with PVA solution initially had an effective diameter of 101.3 nm, but after 4 h had grown to 169.5 nm. In 10% serum, polyplexes alone and polyplexes released from PVA wafers were similar in size, approximately 80 nm at all time points (Figure 3.10B). Polyplexes released from reconstituted PVA wafers were slightly larger (~140 nm) whereas polyplexes mixed with PVA solution were slightly smaller (~40 nm).

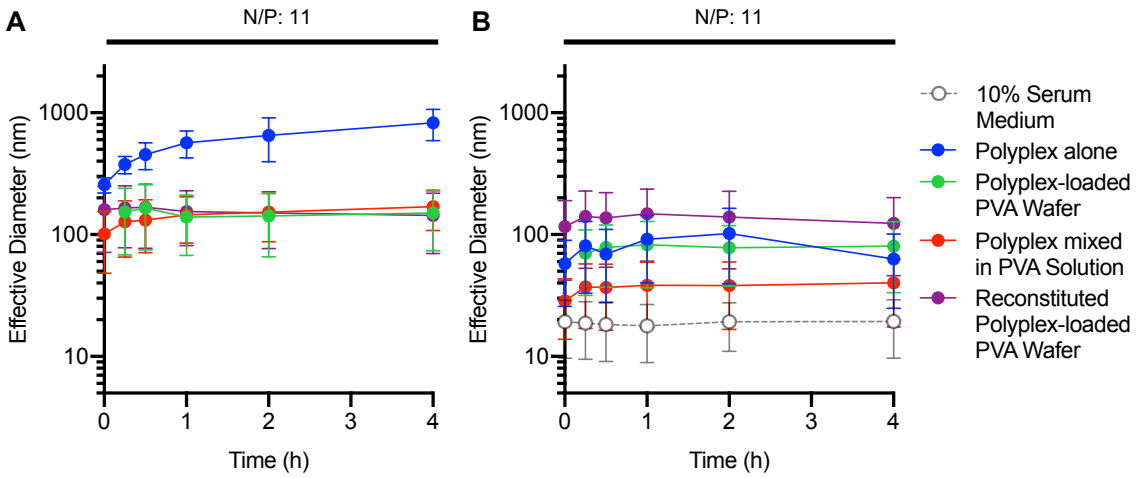

Figure 3.10 Size of polyplexes released from different physical forms of PVA in (A) serum free or (B) 10% serum containing media. Polyplexes were prepared with N/P: 11. Data are shown as effective diameter ± half width as measured by DLS.

3.4 Discussion

In order for a nonviral gene delivery system to be a viable therapeutic agent, it must be able to transfect cells in the presence of serum [30]. The goal of this study is to use polymer wafers to improve efficiency of polyplex-mediated gene delivery in serum containing medium. We have previously demonstrated the ability of wafers composed of binary blends of CMC and ALG to preserve and improve the delivery of sublingual protein vaccines; however, it was quickly determined that these would be unsuitable for nonviral gene delivery. Even in serum-free medium, polyplexes loaded into CMC, ALG, or CMC:ALG (1:1) wafers were unable to transfect NIH/3T3 cells (Figure 3.1). CMC and ALG are both anionic polymers [99,106] and likely adsorbed onto the polyplexes, inhibiting their electrostatic attraction to the cell membrane. Therefore, we sought to prepare wafers comprised of nonionic polymers. Four nonionic polymers were chosen, PVA, HPC, PEO, and PVP, due their good water solubility and history of use as pharmaceutical excipients [84].

The in vitro transfection experiments indicated PVA was vastly superior to HPC, PEO, or PVP for preparing wafers to improve polyplex-mediated gene delivery. In serum free medium, although polyplex-loaded PVA wafers elicited comparable transfection efficiency to polyplexes alone, they performed significantly better than polyplex-loaded HPC, PEO, or PVP wafers (Figure 3.2, Figure 3.3). The most outstanding benefit of PVA wafers was seen when cells were transfected in 10% serum containing medium. The transfection efficiency of polyplexes alone (and polyplex-loaded HPC, PEO, or PVP wafers) in 10% serum containing medium was very low (Figure 3.2E); however, transfection by PVA wafers loaded with polyplexes (N/P: 11) resulted in many GFP+ cells (Figure 3.5B, Figure 3.6E).

A critical component of developing polyplex-loaded polymer wafers was to determine was the effect on the polyplex size following release from the wafers into serum free and 10% serum containing medium. As expected, polyplexes alone aggregated in serum free medium (Figure 3.9A,B). However, aggregation of polyplexes alone was not observed in 10% serum containing medium. Polyplexes released from PEO wafers in serum free medium aggregated even faster than polyplexes alone. Additionally, only polyplexes released from PEO wafers aggregated in 10% serum containing medium. PEGylated polyplexes have previously been shown to unpackage more easily than unmodified polyplexes. Incorporation of PEG into the core likely weakened the electrostatic interactions holding the polyplexes together [34]. Perhaps PEO, which is chemically identical to PEG but has a higher molecular weight, also disrupted the electrostatic interactions of our polyplexes. Polyplexes released from PVA, HPC, and

PVP wafers did not aggregate in serum free (Figure 3.9A,B) or 10% serum containing medium (Figure 3.9C,D).

Taken together, these results suggest that polyplex size does not seem to correlate with transfection efficiency. In 10% serum, the size of polyplexes alone and polyplexes released from PVA wafers are nearly identical. However, the transfection efficiency by polyplex-loaded PVA wafers is much higher (Figure 3.5B, Figure 3.6E). Likewise, the size of polyplexes released from the different physical forms of PVA could not explain the observed differences in transfection efficiency (Figure 3.10). In serum free medium, the polyplexes released from the different physical forms of PVA were nearly identical at all time points. None of the released polyplexes from the different physical forms of PVA aggregated in 10% serum. Additionally, the differences in polyplex size did not correlate with transfection efficiency.

When polyplexes were mixed into an aqueous solution of PVA, the transfection efficiency was diminished in both serum free and 10% serum containing medium (Figure 3.5), revealing that the physical form of PVA is a critical factor in the enhancement of polyplex-mediated gene delivery. PVA is a linear, synthetic polymer that is frequently used in pharmaceutical sciences. The ability to form films, stabilize suspensions by increasing viscosity, bioadhesiveness, and high biocompatibility have made PVA one of the best known and commonly used excipients [123]. PEI-based polyplexes (and lipopolyplexes) released from microparticles were found to be colloidally stable and transfect cells with good efficiency in the presence of serum. Schulze et al. attributed this to the formation of a PVA ‘corona’ coating the polyplexes, shielding the positive surface charges, preventing aggregation and protein adsorption [37,38]. We speculate that a

similar mechanism can explain why polyplex-loaded PVA wafers displayed high transfection efficiency in NIH/3T3 cells (Figure 3.5, Figure 3.6). However, the different physical forms may differ in the amount of PVA coating the polyplexes. When polyplex-loaded PVA wafers are placed in media to transfect cells, they disintegrate over the course of 15-30 min. During this time, the polyplexes are released into media, likely with a relatively thin PVA coating because the bulk of the PVA remains in the disintegrating wafer. The thin coating may be enough to shield the polyplexes enough to prevent aggregation and protein adsorption but thin enough that the electrostatic attraction to cell membranes is still maintained. Mixing polyplexes into an aqueous PVA solution; however, might result in a much thicker PVA coating. This thicker coating may inhibit the polyplex attraction to cell membranes, resulting in reduced cellular uptake. The 30 min incubation and vigorous vortex mixing that was done to reconstitute polyplex-loaded PVA wafers likely generated a similar PVA coating to polyplexes mixed in aqueous PVA solution.

Although the different amounts of PVA coating did not have much effect on the polyplex size (Figure 3.10), it may have profound effects on the zeta potential. Schulze et al. also noted that the PVA corona greatly reduced the zeta potential of polyplexes. While freshly prepared polyplexes displayed positive zeta potential (approximately +20 to +25 mV), polyplexes released from PVA microparticles showed negative zeta potential (approximately -10 to -20 mV) [37]. The zeta potential of our PEI/DNA polyplexes may have been similarly affected, with polyplexes mixed into PVA solution or released from reconstituted PVA wafers experiencing the greatest decrease in zeta potential. Zeta potential reduction may also explain why polyplex (N/P:11)-loaded PVA wafers

transfected cells with high efficiency in 10% serum containing medium (Figure 3.5B, Figure 3.6E), whereas polyplex (N/P: 8)-loaded PVA wafers did not (Figure 3.2E). In the absence of a PVA coating, polyplexes with the lower N/P ratio have a lower zeta potential. Even a minimal PVA coating may inhibit the electrostatic attraction of polyplexes (N/P: 8) to cell membranes.

In addition to high transfection efficiency, biocompatibility of nonviral gene delivery systems is crucial. While the high cationic charge density of PEI is responsible for the electrostatically favorable interactions between PEI-based polyplexes and anionic cell membranes, the charge density can also irreversibly damage the cell membrane, inducing lysis or necrotic death [124]. Surprisingly, even blank PVA wafers were somewhat cytotoxic. Even though PVA is considered to have good biocompatibility [123], approximately 25% of cells were killed after 4 h exposure to blank PVA wafers in both serum free and 10% serum containing medium (Figure 3.7). In contrast, blank HPC, PEO, and PVP wafers display almost no toxicity. Even more confounding, blank PVA solution and blank reconstituted PVA wafers do not exhibit cytotoxicity (Figure 3.8). It appears that is not is not PVA itself, nor any potential contamination during the preparation of PVA wafers, but something about the physical form of the PVA wafers is responsible for the cytotoxicity. When PVA wafers are placed in media, they disintegrate over the course of 15-30 min, but the PVA does not completely dissolve. At the end of the 4 h transfection protocol, the media was removed by vacuum aspiration and the cells were washed with PBS. Perhaps during the aspiration, undissolved PVA particulates mechanically damaged the cells, resulting in toxicity. Although polyplexes alone and polyplex-loaded HPC and PVP wafers were more toxic than their blank counterparts, the

observation that polyplex-loaded PVA wafers are not more cytotoxic than blank PVA wafers in 10% serum containing medium is encouraging (Figure 3.8). If the aspiration-induced mechanical cell damage is an artifact of the in vitro protocol, perhaps the polyplex-loaded PVA wafers would more biocompatible when tested in vivo.

Taken together, these results demonstrate that PVA wafers are an effective delivery system to improve the in vitro transfection efficiency of polyplex-mediated gene delivery in the presence of serum. As PVA is known to have mucoadhesive properties [84], these wafers may be exceptionally suited for mucosal delivery of gene therapy. While we demonstrated high transfection efficiency using GFP as a reporter gene, future studies using these PVA wafers will deliver DNA vaccines. These vaccines could be delivered to the sublingual mucosa, or other targeted mucosal tissue, to generate robust cell-mediated and humoral immune responses.

3.5 Conclusions

We have prepared and loaded PEI/DNA polyplexes into polymer wafers consisting of various water-soluble polymers – CMC, ALG, PVA, HPC, PEO, and PVP – through a simple process. Polyplex-loaded PVA wafers transfected NIH/3T3 cells in vitro with high efficiency. While the transfection efficiency by polyplex-loaded PVA wafers was similar to polyplexes alone in serum free medium, the PVA wafers greatly enhanced the polyplex-mediated transfection efficiency in 10% serum containing medium. We also observed that the physical form of the PVA wafer is crucial for this enhancement. These findings established that the polyplex-loaded PVA wafers have the potential to improve the efficiency of polyplex-mediated gene delivery in vivo.

Chapter 4 Synergistic Cancer Cell Killing by a Synthetic Membranolytic Polymer and Doxorubicin

4.1 Introduction

Cancer is the second leading cause of mortality globally and was responsible for 9.6 million deaths in 2018 [125]. Doxorubicin (DOX) is one of the most effective chemotherapeutic agents and is used to treat many types of cancer, including cancers of the bladder, breast, stomach, lung, ovaries, thyroid, soft tissue sarcoma, multiple myeloma, and Hodgkin's lymphoma [39]. DOX is an anthracycline that intercalates between nucleic acid base pairs, blocking the transcription and replication processes by inhibiting the synthesis of DNA and RNA in rapidly dividing cells [126]. DOX also inhibits the enzyme topoisomerase II, which prevents the resealing of DNA double helices and stops replication [127]. DOX can also generate free radicals that induce DNA and cell membrane damage, triggering apoptosis [39].

Despite the potency of DOX, many cancer cells develop multidrug resistance to DOX and other chemotherapeutic drugs. A number of mechanisms may elicit multidrug resistance, including the overexpression of membrane transporters such as P-glycoprotein and Multidrug Resistance-Associated Protein 1 (MRP1) which act as efflux pumps that pump chemotherapeutic drugs out of cancer cells [41]. To overcome the reduced drug uptake, higher drug dosage must be used. However, high DOX doses presents severe side effects such as cardiotoxicity and myelosuppression [128]. A number of nanocarriers have been developed to target DOX accumulation within tumors to reduce off target

toxicity, such as PEGylated liposomes (e.g. Doxil®) [128]; however, the issue of poor drug uptake remains.

One class of anti-cancer agents that may overcome multidrug resistance are cationic macromolecules [11]. Inspired by naturally occurring antimicrobial peptides, such as defensins and cecropins [129], a number of amphipathic cationic peptides have been shown to effectively kill cancer cells [11]. These anticancer peptides are electrostatically attracted to negatively charged cancer cell membranes and disrupt the membranes by hydrophobic interactions, leading to increased membrane permeability and eventual cell lysis. Since the cytotoxic activity is directed to the cell membrane, these peptides can evade multidrug resistance mechanisms [11]. In addition, the increased membrane permeability can facilitate the uptake of traditional chemotherapeutic drugs. Anticancer peptides have been shown to increase cancer cell uptake of 5-fluorouracil, cytarabine, paclitaxel, epirubicin, and DOX [130–132].

Despite their promise, the high production cost and susceptibility to enzymatic degradation by serum proteases has limited the clinical application of these anticancer peptides [11]. In contrast, synthetic polymers can be designed to mimic the cationic amphipathic structure of anticancer peptides, while being easier to synthesize on a large scale and more resistant to proteolytic degradation. In addition, synthetic polymers are more chemically tunable and offer greater flexibility in terms of structure [11,133]. Several classes of polymers have been reported to induce membrane lysis, including polymethacrylates, polyacrylamides, polyethyleneimines (PEI), and polyamides [11,124]. Similar to anticancer peptides, these polymers can be used alone to kill cancer cells by membrane lysis or used in combination with chemotherapeutic agents to increase drug

uptake. A few synthetic polymers have been shown to enhance uptake of DOX by cancer cells, including branched PEI dendrimers [42], and poly(amido amine)-2,3-dimethylmaleic monoamide (PAMAM-DMA) dendrimers [134].

The objective of the present study is to use a synthetic membranolytic polymer, poly (6-amino-1-hexyl methacrylate) (PAHM) to disrupt cancer cell membranes and to use PAHM in combination with DOX to kill cancer cells synergistically. Membrane disruption by PAHM and the increased uptake of DOX was examined using mouse breast cancer cells (EMT6) and human pancreatic cancer cells (AsPC-1). The cytotoxicity of PAHM and DOX to EMT6 and AsPC-1 was measured and the combination index (CI) and dose reduction index (DRI) of each of the PAHM and DOX combinations were quantified using the Chou-Talalay method [135]. Lastly, PAHM and DOX were used to kill EMT6 multicellular tumor spheroids.

4.2 Materials and Methods

4.2.1 Chemicals and reagents

Roswell Park Memorial Institute (RPMI) 1640 medium, fetal bovine serum (FBS), Penicillin-Streptomycin (10,000 U/mL; 10,000 μg/mL), Dulbecco's phosphate buffered saline (DPBS), phosphate buffered saline (PBS, pH 7.4), trypsin-EDTA (0.25%), trypan blue (0.4% solution, 0.85% NaCl), MTT (3-(4,5-dimethylthiazol- 2-yl)-2,5-diphenyltetrazolium bromide) (MTT), dimethyl sulfoxide (DMSO), Live Cell Imaging Solution (LCIS), agarose, NucBlue Live ReadyProbes Reagent (Hoechst 33342), and NucGreen Dead 488 ReadyProbes Reagent (SYTOX Green) were purchased from Thermo Fisher Scientific (Waltham, MA). Propidium iodide (PI, 0.5 mg/mL in PBS) was purchased from BioLegend (San Diego, CA). Doxorubicin hydrochloride (European

Pharmacopoeia Reference Standard) was purchased from Sigma Aldrich (St. Louis, MO). Glass bottom microwell dishes were purchased from MatTek (Ashland, MA).

4.2.2 Synthesis of poly (6-amino-1-hexyl methacrylate) (PAHM)

N-(tert-butoxycarbonyl) aminohexyl methacrylate (tBocAHM) was synthesized as described by Zhu et al [136]. PAHM was synthesized via atom transfer radical polymerization (ATRP) of tBocAHM followed by deprotection of the tBoc side chains based on a method reported by Ji et al [137]. The polymer was characterized using ^{1}H NMR and gel permeation chromatography (GPC) as described by Ji [138]. The PAHM used in the subsequent experiments had a number-average molecular weight (M_n) of 2.08 $\times 10^4$, Dispersity (Đ) of 1.26, and average degree of polymerization (DP) of 100.

4.2.3 Cell culture

Mouse mammary carcinoma cell line EMT6 and human pancreatic adenocarcinoma cell line AsPC-1 were obtained from ATCC. EMT6 or AsPC-1 cells were cultured in media consisting of RPMI 1640 medium with 2 g/L glucose, 2 mM L-glutamine, 2 g/L sodium bicarbonate, 10% heat inactivated fetal bovine serum (FBS), 100 U/mL penicillin, and 100 µg/mL streptomycin. EMT6 or AsPC-1 cells were cultured in tissue culture flasks and incubated in a humidified environment at 37ºC with 5% CO_2. When cells reached ~80% confluency the culture medium was removed, cells were rinsed with DPBS, and 0.25% trypsin-EDTA was added for 5 min to detach cells from the flasks. Harvested cells were centrifuged at 200 x *g* for 5 min and supernatant was discarded. Cell pellets were resuspended in cell culture medium and a 100 µL aliquot was stained 1:1 with trypan blue 0.4% solution and counted using a hemocytometer (Sigma-Aldrich, St. Louis, MO) and inverted microscope (Thermo Fisher Scientific, Waltham, MA). Cell

suspensions were split 1:3 to 1:6 to continue culture or diluted to the appropriate seeding density for subsequent experiments.

4.2.4 Propidium iodide (PI) staining

Cell membrane disruption by PAHM was visualized by staining cells with PI. EMT6 or AsPC-1 cell suspensions were diluted to density of 50,000 cells/mL in cell culture media and were plated in glass bottom microwell dishes (50,000 cells/dish). Cells were incubated in a humidified environment at 37ºC with 5% CO_2 overnight (~20 h). Culture media was removed, cells were washed twice with 1 mL PBS, and replaced with 1 mL live cell imaging solution (LCIS). PI stain was prepared by diluting PI stock solution (0.5 mg/mL) to 40 μM in LCIS. Cells were stained with 4 μM PI by adding 110 μL PI stain (40 μM) to each dish. PAHM was dissolved in LCIS at varying concentration and 100 μL was added to each dish to give final concentrations of 0, 10, 20, 30, 40, 50, or 75 μg/mL.

Phase contrast and fluorescent images of EMT6 cells were acquired with a Nikon Eclipse Ti-E inverted microscope equipped with a Nikon CFI Plan Apochromat Lambda 40XC/0.95 NA objective and an Andor Zyla sCMOS camera. PI was visualized using an excitation wavelength of 515 ± 30 nm and emission wavelength of 590 ± 45 nm. An exposure time of 27 ms was chosen to minimize autofluorescence. EMT6 cells were kept in an environmental chamber at 37ºC with 5% CO_2 and imaged continuously for 30 min. Images were analyzed in ImageJ.

Phase contrast and fluorescent images of AsPC-1 cells were acquired with an Olympus IX70 inverted microscope equipped with an Olympus plan fluorite 20XPH/0.45 NA objective, an Olympus DP72 camera, and an X-Cite 120 Wide-Field Fluorescence Microscope Excitation Light Source (Excelitas Technologies, Waltham, MA). PI was

visualized using an excitation wavelength of 535 ± 50 nm and emission wavelength of 610 ± 75 nm. An exposure time of 20 ms was chosen to minimize autofluorescnce. AsPC-1 cells were kept under ambient conditions and imaged after 30 min exposure to PAHM.

4.2.5 Cellular uptake of DOX

EMT6 or AsPC-1 cell suspensions were diluted to density of 50,000 cells/mL in cell culture media and were plated in glass bottom microwell dishes (100,000 cells/dish). Cells were incubated in a humidified environment at 37ºC with 5% CO_2 overnight (~20 h). Culture media was removed, cells were washed twice with 1 mL PBS, and replaced with 2 mL live cell imaging solution (LCIS). Cell nuclei were stained with Hoechst 33342 by adding 2 drops of NucBlue Live ReadyProbes Reagent to each dish followed by incubation in a humidified environment at 37ºC with 5% CO_2 for 20 min. DOX was dissolved in deoinized water at concentration of 5 mg/mL, diluted in LCIS, and 100 µL was added to each dish to give final concentrations of 0, 5, or 10 µg/mL DOX. PAHM was dissolved in LCIS at varying concentrations and 100 µL was added to each dish to give final concentrations of 0, 5, or 10 µg/mL PAHM. After incubating in humidified environment at 37ºC with 5% CO_2 for 15 min, media containing DOX and PAHM were removed, cells were washed twice with 1 mL DPBS, and replaced with 2 mL fresh LCIS.

Phase contrast and fluorescent images of EMT6 or AsPC-1 cells were acquired with an Olympus IX70 inverted microscope equipped with an Olympus plan fluorite 20XPH/0.45 NA objective, an Olympus DP72 camera, and an X-Cite 120 Wide-Field Fluorescence Microscope Excitation Light Source (Excelitas Technologies, Waltham, MA). Hoechst 33342-stained cell nuclei were visualized using an excitation wavelength

of 350 ± 50 nm and emission wavelength of 460 ± 50 nm. Exposure times of 2 ms (EMT6 cells) or 10 ms (AsPC-1 cells) were chosen to minimize autofluorescence. DOX was visualized using an excitation wavelength of 535 ± 50 nm and emission wavelength of 610 ± 75 nm. Exposure times of 20 ms (EMT6 cells) or 100 ms (AsPC-1) cells was chosen to minimize autofluorescence. Images were analyzed in ImageJ.

4.2.6 Cytotoxicity of DOX and PAHM in 2D monolayer culture

EMT6 or AsPC-1 cell suspensions were diluted to 50,000 cells/mL in phenol red free cell culture media and were plated in 96-well plates (5,000 cells/well). Cells were incubated in a humidified environment at 37ºC with 5% CO_2 overnight (~20 h). DOX was dissolved in deionized water at concentration of 5 mg/mL and diluted in phenol red free cell culture media at varying concentrations. PAHM was dissolved directly in phenol red free cell culture media at varying concentrations. Cell culture media was removed from EMT6 or AsPC-1 cells and replaced with 100 µL media containing DOX, PAHM, or combinations of DOX and PAHM at varying concentrations. After incubation in a humidified environment at 37ºC with 5% CO_2 for 24 or 48 h, media containing DOX and PAHM were removed and replaced with 100 µL fresh phenol red free cell culture media. Cell viability was evaluated using an MTT (3-(4,5-dimethyl-thiazol-2-yl)-2,5-diphenyl tetrazolium bromide) assay [122]. To each well, 10 µL MTT solution (5 mg/mL in DPBS) was added. After 4 h incubation in a humidified environment at 37ºC with 5% CO_2, 85 µL medium was removed from each well. Formazan crystals were dissolved in 50 µL DMSO and absorbance was measured at 540 nm and corrected for blank media background using a BioTek Cytation 3 Cell Imaging Multi-Mode Reader BioTek

Instruments, Winooski, VT). Cell viability was determined by normalizing by the absorbance of untreated cells.

4.2.7 COMPUSYN modeling of drug synergy

For each combination of DOX and PAHM, the combination index (CI) and dose reduction index (DRI) were calculated by the Chou-Talalay method with the CompuSyn software program (ComboSyn Inc., Paramus, NJ) [135]. Input parameters were the dose of each treatment (alone or in combination) and the corresponding fractional affect (Fa) – the fraction of cell growth inhibited by a particular dose, calculated as Fa = (100% - cell viability / 100%). The dose-effect relationship for DOX or PAHM and their combinations are described by the Median-Effect Equation $Fa/Fu = (D/D_m)^m$, where Fu is the unaffected fraction of cell growth (Fu = 1 – Fa), D is the dose required to produce Fa, D_m is the median-effect dose (i.e. IC_{50}), and m is the dynamic order of the curve. Using these parameters, the CI and DRI can be calculated. The CI value is dimensionless quantification of drug interaction, calculated as $CI = (D)_1/(D_x)_1 + (D)_2/(D_x)_2$, where $(D_x)_1$ is the dose of single drug D_1 (i.e. DOX concentration) "alone" that inhibits cell growth by x%, $(D_x)_2$ is the dose of a second drug D_2 (i.e. PAHM concentration) "alone" that inhibits cell growth by x%, and $(D)_1$ and $(D)_2$ are the doses "in combination" that also inhibit cell growth by x%. CI = 1 indicates an additive effect; CI < 1 indicates a synergistic effect; CI > 1 indicates an antagonistic effect. The DRI is a measure of how much the dose of each drug can be reduced if used in combination at a given Fa as compared to the dose of each drug alone, calculated as $(DRI)_1 = (D_x)_1/(D)_1$ and $(DRI)_2 = (D_x)_2/(D)_2$. DRI = 1 indicates no dose reduction; DRI > 1 indicates favorable dose reduction, DRI < 1 indicates unfavorable dose reduction.

4.2.8 Formation of EMT6 tumor spheroids

Multicellular 3D tumor spheroids were formed as described previously [139]. Agarose was dissolved in phenol red free RPMI 1640 (15 mg/mL) and sterilized by autoclaving (121ºC, 15 psi) for 20 min. Sterile agarose solution was placed in an 85ºC water bath inside a tissue culture hood. The bottom of 96-well plates was coated with 60 µL/well warm agarose solution. After allowing the agarose solutions to solidify, the coated plates were wrapped in aluminum foil and stored in a tissue culture hood overnight. EMT6 cell suspensions were diluted to 15,000 cells/mL in phenol red free cell culture medium and were plated in agarose-coated 96-well plates (3,000 cells/well). Cells were incubated in a humidified environment at 37ºC with 5% CO_2 to allow spheroids to form. Phase contrast images of the spheroids were acquired with an Olympus IX70 inverted microscope equipped with an Olympus plan 10X/0.25 NA objective and an Olympus DP72 camera. Images were analyzed and the initial spheroid area was quantified using ImageJ.

4.2.9 Cytotoxicity of DOX and PAHM in 3D tumor spheroids

DOX was dissolved in deionized water at concentration of 5 mg/mL and diluted in phenol red free cell culture media at varying concentrations. PAHM was dissolved directly in phenol red free cell culture media at varying concentrations. From each spheroid, 100 µL cell culture medium was removed and replaced with 100 µL media containing DOX, PAHM, or combinations of DOX and PAHM at varying concentrations. Spheroids were incubated for 3 days in an environment at 37ºC with 5% CO_2. Each day, phase contrast images of the spheroids were acquired and quantified as described above. Spheroid growth was determined by normalizing by the initial spheroid area.

4.2.10 Statistical analysis

ANOVA and Tukey HSD test for multiple comparisons were to determine the significance of differences in onset time of membrane disruption by different PAHM concentrations, differences in fluorescence intensity of intracellular DOX, and differences in cell viability between different treatment groups. All analyses were performed using GraphPad prism, version 9.0.0 (GraphPad software Inc., San Diego, California, USA).

4.3 Results

4.3.1 Cell membrane disruption by PAHM

The disruption of EMT6 cell membranes by PAHM was visualized by intracellular staining by PI, a membrane impermeable dye that enters a cell through disrupted membrane and binds to DNA, resulting in a 20- to 30-fold increase in fluorescence intensity [140]. After exposure to 10 – 75 μg/mL of PAHM, PI fluorescence signal appeared inside many EMT6 cells within minutes, indicating that the cell membrane was permeabilized (Figure 4.1A). The percentage of PI+ cells over time was dependent on PAHM concentration. For cells treated with a high dose of PAHM (≥40 μg/mL), 100% became PI+ within 5 min; however, lower PAHM doses (10 – 30 μg/mL) only resulted in 76 – 86% PI+ cells even after 30 min (Figure 4.1B). The onset time of membrane disruption correlated strongly with PAHM concentration. Lower PAHM doses (10 – 30 μg/mL) did not cause membrane disruption until approximately 5 min later, whereas high PAHM doses (≥40 μg/mL) shortened the onset time of membrane disruption to about 1 – 2 min (Figure 4.1C). Similar observation was made on PAHM-treated AsPC-1 cells as well (Figure 4.2).

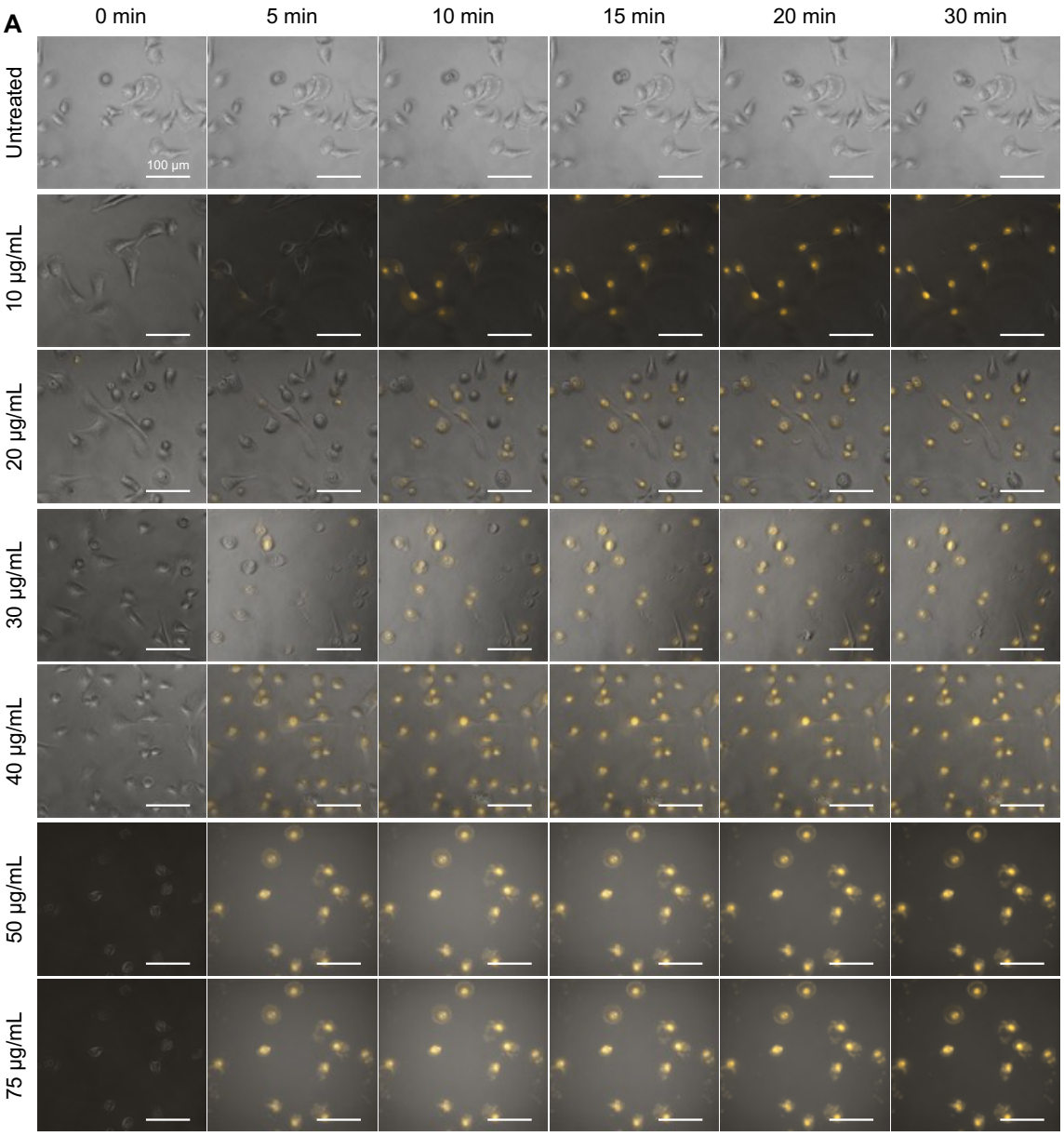
A
0 min
5 min
10 min
15 min
20 min
30 min
Untreated
10 µg/mL
20 µg/mL
30 µg/mL
40 µg/mL
50 µg/mL
75 µg/mL
100 µm

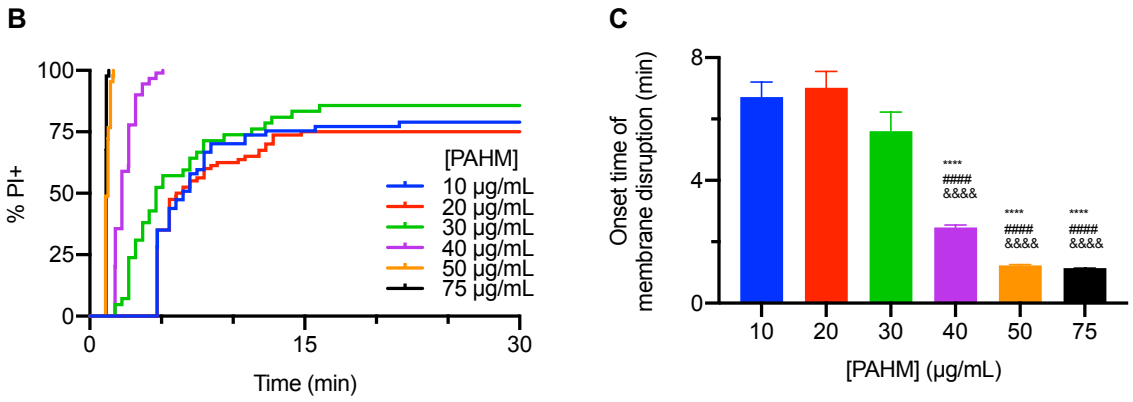

Figure 4.1 Visualization of disruption of EMT6 membranes by PAHM. (A) Representative time-lapse fluorescence microscopy images of PAHM-treated EMT6 cells stained with PI. (B) Percentage of PI+ cells over time (n = 42 – 90). (C) Onset time of membrane disruption. Data are shown as mean ± SEM (n = 36 – 90). ANOVA with Tukey HSD test (**** p <0.0001 vs 10 µg/mL PAHM, #### p <0.0001 vs 20 µg/mL PAHM, &&&& p <0.0001 vs 30 µg/mL PAHM).

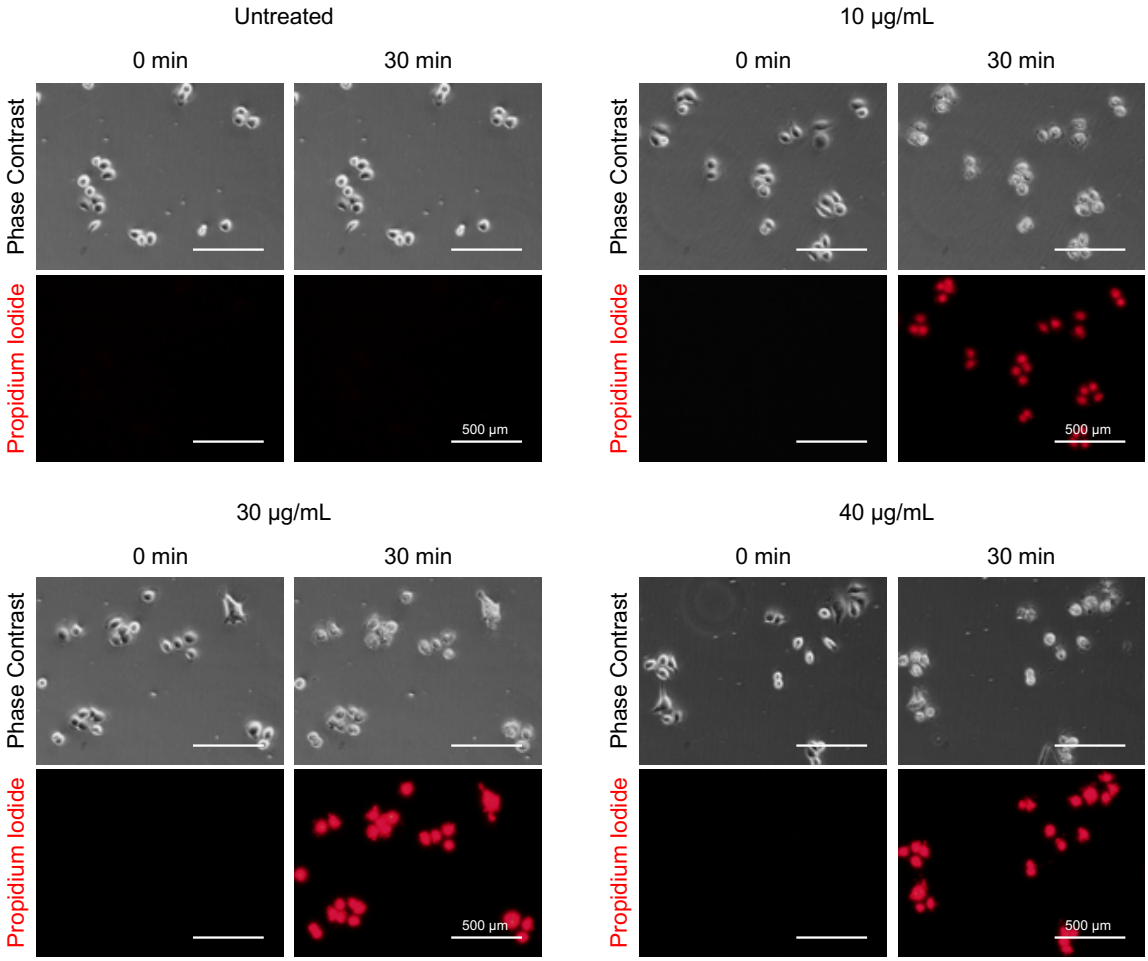

Figure 4.2 Visualization of disruption of AsPC-1 membranes by PAHM. Representative fluorescence images of PAHM-treated AsPC-1 cells stained with PI.

4.3.2 PAHM-mediated membrane disruption leads to enhanced DOX uptake

To examine the impact of PAHM treatment on the intracellular uptake of DOX, EMT6 and AsPC-1 cells were exposed to DOX at 5 and 10 µg/mL in the presence or absence of equal mass concentrations of PAHM and visualized with fluorescence microscopy after 15 min (Figure 4.3A,B).

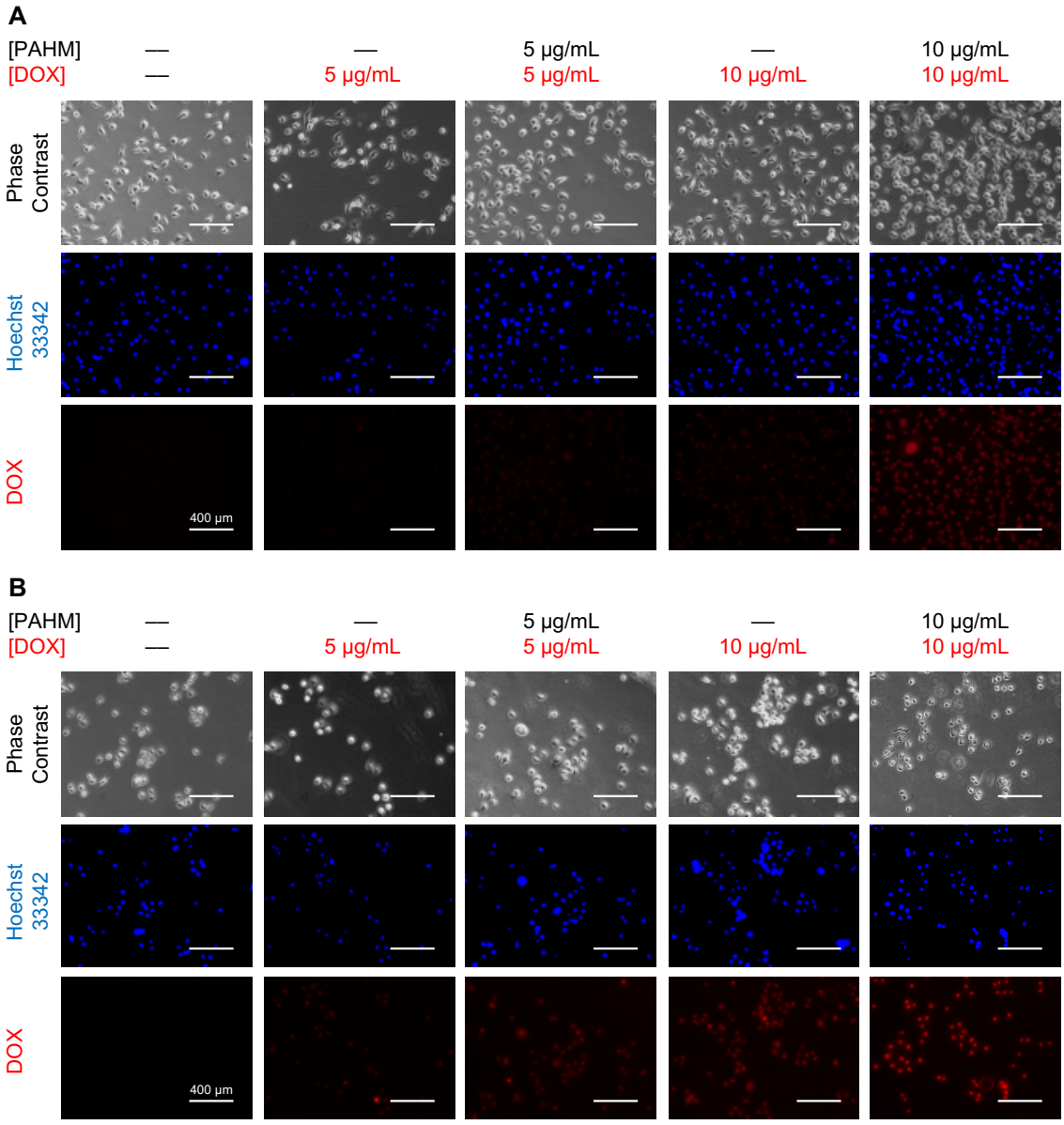

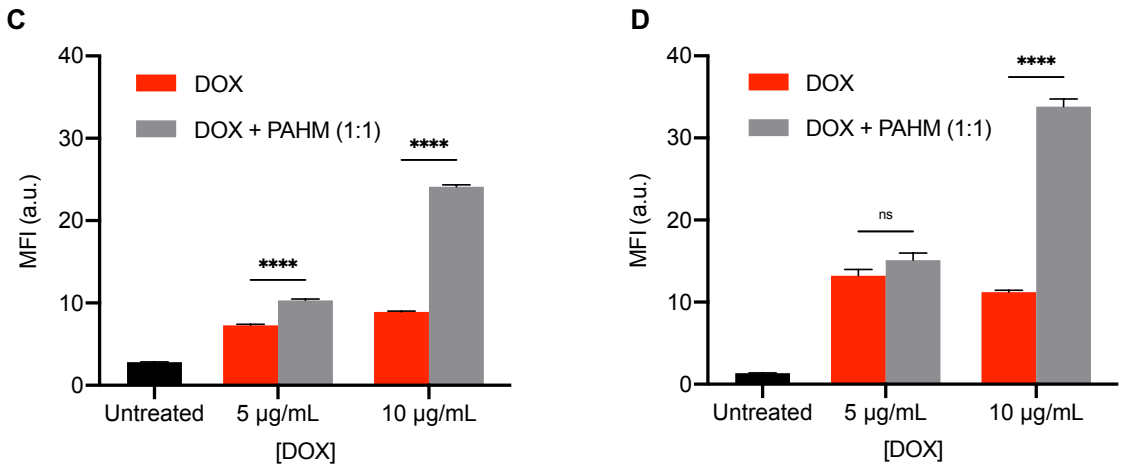

Figure 4.3 Membrane disruption by PAHM leads to increased cellular uptake of DOX. Representative fluorescence microscopy images of (A) EMT6 cells and (B) AsPC-1 cells. Quantification of DOX fluorescence intensity in (C) EMT6 cells and (D) AsPC-1 cells. Data are shown as mean ± SEM (C) (n = 183 – 499) (D) (n = 109 – 160). ANOVA with Tukey HSD test (**** $p < 0.0001$, ns: not significant).

These doses of DOX and PAHM were chosen because they were low enough not to cause massive cell death in 15 min, which would otherwise make observation of DOX uptake impossible. The microscopy images and the quantification of the intracellular DOX fluorescence intensity in both cell lines show that DOX alone at 5 and 10 µg/mL had very low level of intracellular uptake, yet 5 µg/mL of PAHM led to a small but significant increase in DOX uptake in EMT6 cells (Figure 4.3C). Notably, the treatment with 10 µg/mL of PAHM led to a 2.7-fold increase in DOX uptake in EMT6 cells ($p < 0.0001$) (Figure 4.3C) and a 3.0-fold increase in DOX uptake in AsPC-1 cells ($p < 0.0001$) (Figure 4.3D).

4.3.3 Combination of DOX and PAHM kills cells synergistically

To study the synergistic cytotoxicity of DOX and PAHM, EMT6 cells were exposed to DOX or PAHM alone (Figure 4.4A) or DOX and PAHM at constant ratios of 1:100 or 1:50 (Figure 4.4B). The dose-effect curves were fit with the median-effect equation: $fa/fu = (D/Dm)^m$, where D is the dose, Dm is the dose to produce median effect (i.e. IC50), fa

is the fraction affected by dose D, fu is the unaffected fraction, and m depicts the shape of the dose-effect curve: For DOX or PAHM alone, the Dm were 0.3 μg/mL and 11.7 μg/mL, respectively. The 1:100 DOX and PAHM combination displayed a similar dose-effect curve to PAHM alone, with Dm = 13.1 μg/mL. In contrast, the 1:50 DOX and PAHM combination resulted in greater cytotoxicity as indicated by the lower Dm of 3.7 μg/mL. Using these parameters, the CI of both 1:100 and 1:50 combinations were modelled across all Fa (Figure 4.4C,D). At lower Fa (≤0.65) the model of the 1:100 combination of DOX and PAHM appears to be antagonistic, but the CI decreases with Fa (Figure 4.4C). In contrast, at high Fa (≥0.8) the 1:100 combination shows synergism between DOX and PAHM as indicated by the CI ≤0.87. The 1:100 experimentally calculated CI are in good agreement with the model, as all but one of the 1:100 combinations with Fa ≥0.85 had experimentally calculated CI ≤0.89. The 1:50 combination displays much greater synergism between DOX and PAHM. The model shows that only for Fa ≥0.3, the 1:50 combination of DOX and PAHM are synergistic with CI ≤0.88 (Figure 4.4D). At high Fa (≥0.85), the 1:50 combination is strongly synergistic as indicated by CI ≤0.28. The experimentally calculated CI also show that the 1:50 combination of DOX and PAHM is synergistic across a wide range of Fa. All but one of the 1:50 combinations was synergistic with CI ≤0.73. At very high Fa (≥0.97), the 1:50 combination was strongly synergistic with experimentally calculated CI ≤0.27.

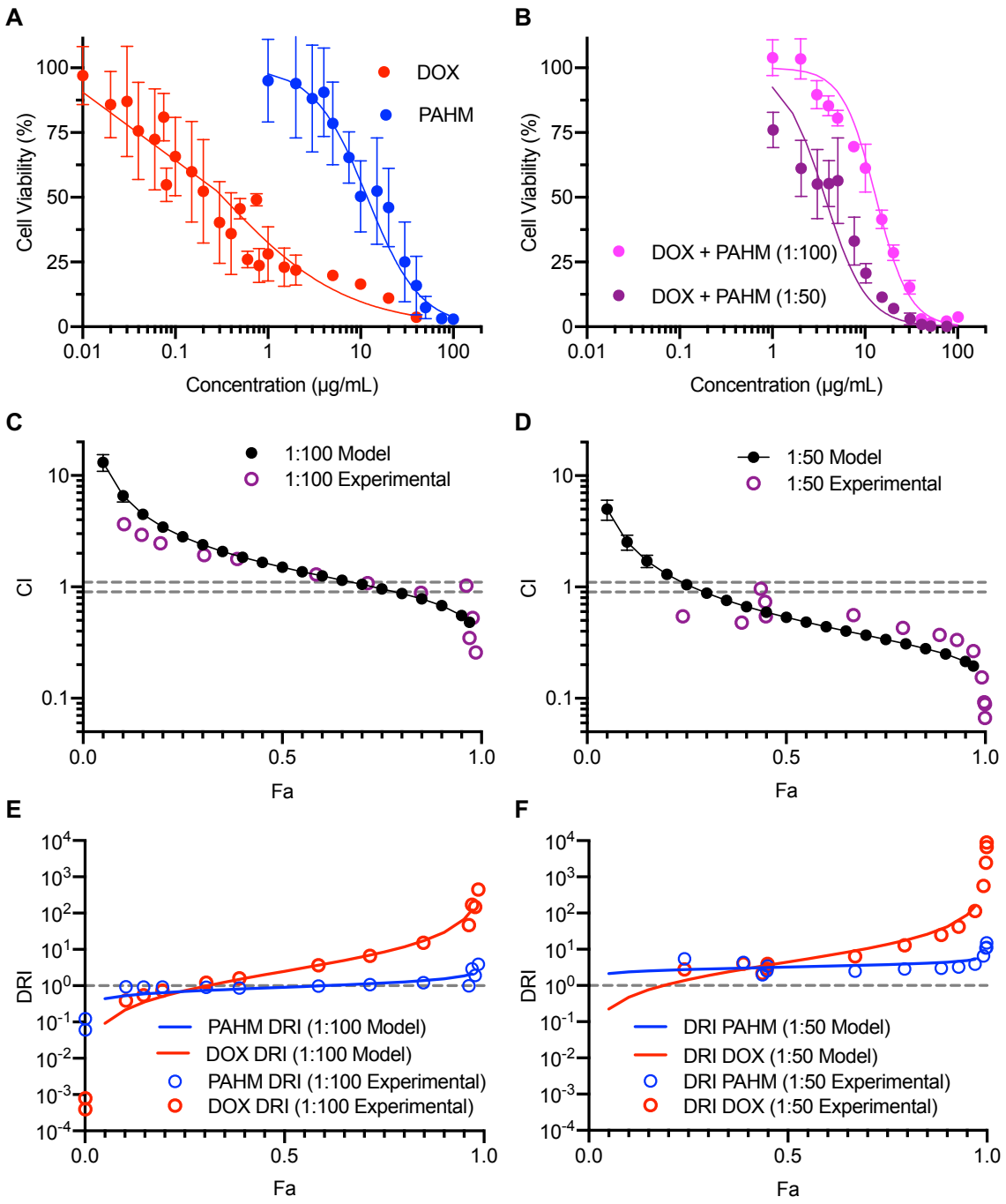

Figure 4.4 DOX and PAHM kill EMT6 cells synergistically. (A) Cell viability of EMT6 cells after 24 h exposure to DOX or PAHM alone. (B) Cell viability of EMT6 cells after 24 h exposure to DOX and PAHM. Data are shown as mean ± SD (A) (n = 6 – 30) (B) (n = 6 – 12). Data fit with median-effect equation [135]. (C,D) Combination index analysis (CI <1, = 0.9 - 1 (dashed lines), >1 indicates synergism, nearly additive effect, and antagonism, respectively). Error bars indicate 95% confidence intervals for CI values based on sequential deletion analysis [135]. (E,F) Dose reduction index analysis (DRI <1, =1 (dashed line), >1 indicates unfavorable dose reduction, no dose reduction, and favorable dose reduction, respectively).

The DRI of both 1:100 and 1:50 combinations were similarly modelled across all Fa (Figure 4.4E,F). For the 1:100 combination, the DOX DRI increases with Fa while the PAHM DRI is approximately 1 for a majority of Fa, suggesting the DOX benefits more from the 1:100 combination with PAHM (Figure 4.4E). At high Fa (≥0.85) the DOX DRI were greater than 17.5 and 15.2 for the model and experimentally calculated DRI, respectively, which indicates that the DOX dose can be significantly reduced when combined with PAHM (1:100) to kill a high percentage of EMT6 cells. The DOX DRI from the 1:50 combination similarly increases with Fa but the PAHM DRI is approximately 2 for most Fa (Figure 4.4F). Thus, PAHM benefits slightly from the combination with DOX. In contrast, the DOX dose can be significantly reduced, especially at high Fa (≥0.85) where the DOX DRI were greater than 26.1 and 24.9 for the model and experimentally calculated DRI, respectively.

The synergistic killing of AsPC-1 cells by DOX and PAHM to AsPC-1 cells was also demonstrated. AsPC-1 were exposed to DOX or PAHM alone (Figure 4.5A) or DOX and PAHM at a constant ratio of 1:1 (Figure 4.5B). For DOX or PAHM alone, the Dm were 22.0 μg/mL and 8.3 μg/mL, respectively. The 1:1 combination of DOX and PAHM was more cytotoxic than either treatment alone, with a Dm of 7.9 μg/mL. The CI and DRI for the 1:1 DOX and PAHM combination were also modelled across all Fa (Figure 4.5C,D). DOX and PAHM appear to be synergistic at Fa ≥0.35 as all CI calculated by the model were ≤0.88 (Figure 4.5C). The model is in good agreement with the experimentally calculated CI, a majority of which were ≤0.86 for Fa ≥0.43. Similar to the EMT6 cells, AsPC-1 cells can be killed by reduced doses of DOX and PAHM when they are used together. Most of the PAHM DRI were approximately 2 and the DOX DRI increases with

Fa (Figure 4.5D). At high Fa (≥0.85), DOX benefits greatly by the combination with PAHM as the DOX DRI were greater than 53.7 and 51.3 for the model and experimentally calculated DRI, respectively.

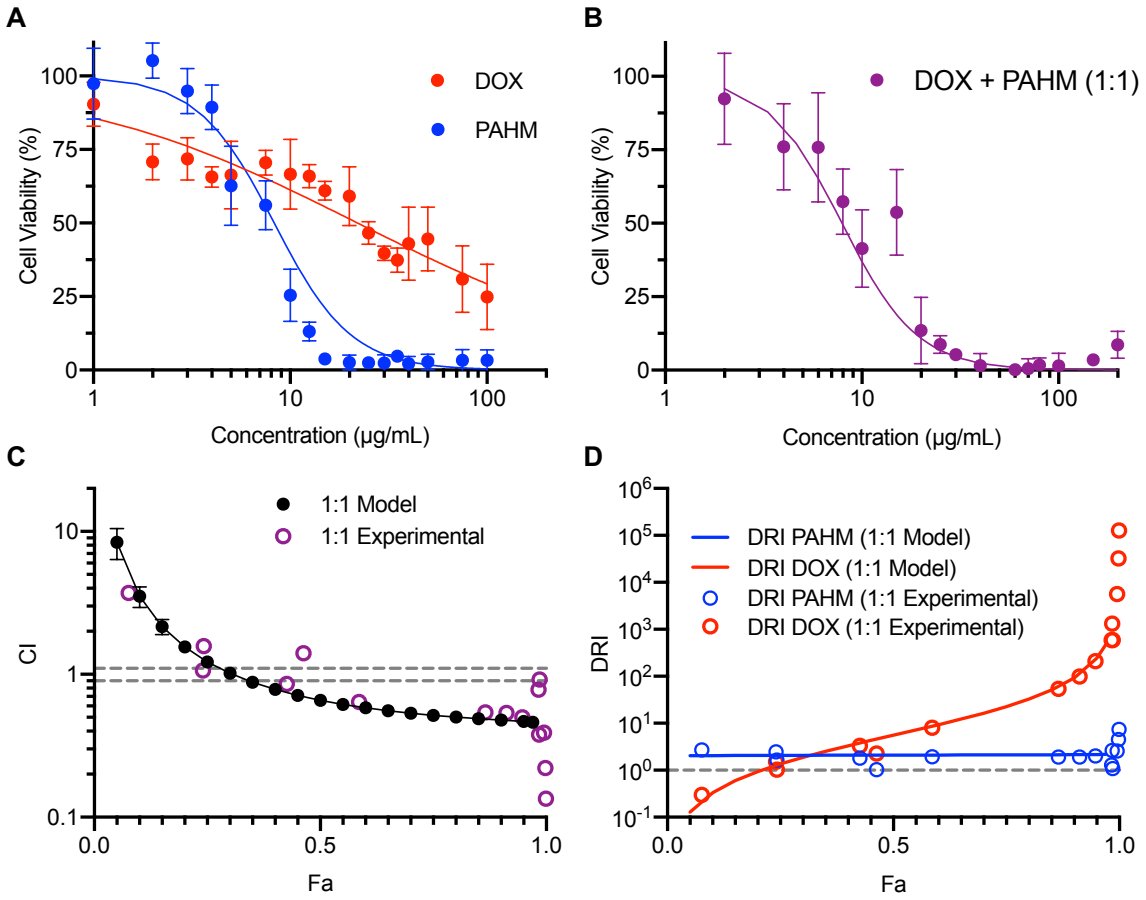

Figure 4.5 DOX and PAHM kill AsPC-1 cells synergistically. (A) Cell viability of AsPC-1 cells after 24 h exposure to DOX or PAHM alone. (B) Cell viability of AsPC-1 cells after 24 h exposure to DOX and PAHM. Data are shown as mean ± SD (A) (n = 6 – 30) (B) (n = 6 – 18), Data fit with median-effect equation [135]. (C) Combination index analysis (CI <1, = 0.9 – 1 (dashed lines), >1 indicates synergism, nearly additive effect, and antagonism, respectively). Error bars indicate 95% confidence intervals for CI values based on sequential deletion analysis [135]. (E) Dose reduction index analysis (DRI <1, =1 (dashed line), >1 indicates unfavorable dose reduction, no dose reduction, and favorable dose reduction, respectively).

4.3.4 Synergistic cytotoxicity dependent on PAHM concentration

To further investigate the synergistic cytotoxicity, EMT6 cells were exposed to non-constant ratios of DOX and PAHM for 24 h. Depending on the dose, combining DOX

with PAHM resulted to increased cell death (Figure 4.6A). At low doses of DOX (0.1 – 1 μg/mL), the addition of low doses of PAHM (1 – 10 μg/mL) led to a slight increase in cell killing over DOX alone. At higher doses of DOX (5 – 40 μg/mL), the addition of 1 – 10 μg/mL PAHM had little effect. However, the addition of 20 – 40 μg/mL PAHM resulted in a much greater reduction in cell viability across all DOX doses.

The CI follow a similar trend to the cell viability data (Figure 4.6B). For combinations of low DOX (0.1 – 1 μg/mL) and low PAHM (1 – 10 μg/mL) doses the CI were near or slightly below 1, indicating that these combinations were nearly additive or slightly synergistic. For high DOX (5 – 40 μg/mL) and low PAHM (1 – 10 μg/mL) doses the CI were all ≥1.16, indicating that these combinations were antagonistic. At high PAHM doses (20 – 40 μg/mL) all but one combination were synergistic with CI ≤0.76.

The DOX DRI follow the same trend as the cell viability and CI data. The majority of the DOX DRI were greater than 1 (Figure 4.6C), indicating that the DOX dose can be reduced when used in combination with PAHM. The DOX DRI were also much greater when 20 – 40 μg/mL PAHM was added. Only the antagonistic combinations of high DOX (5 – 40 μg/mL) and low PAHM (1 – 10 μg/mL) gave DOX DRI <1. The PAHM DRI tends to increase with Fa and all but three of the PAHM DRI were >1 (Figure 4.6D), indicating that the PAHM can also be reduced when used in combination with PAHM. The PAHM DRI tends to decrease with PAHM concentration, suggesting that the lower PAHM doses benefit more from the combination with DOX.

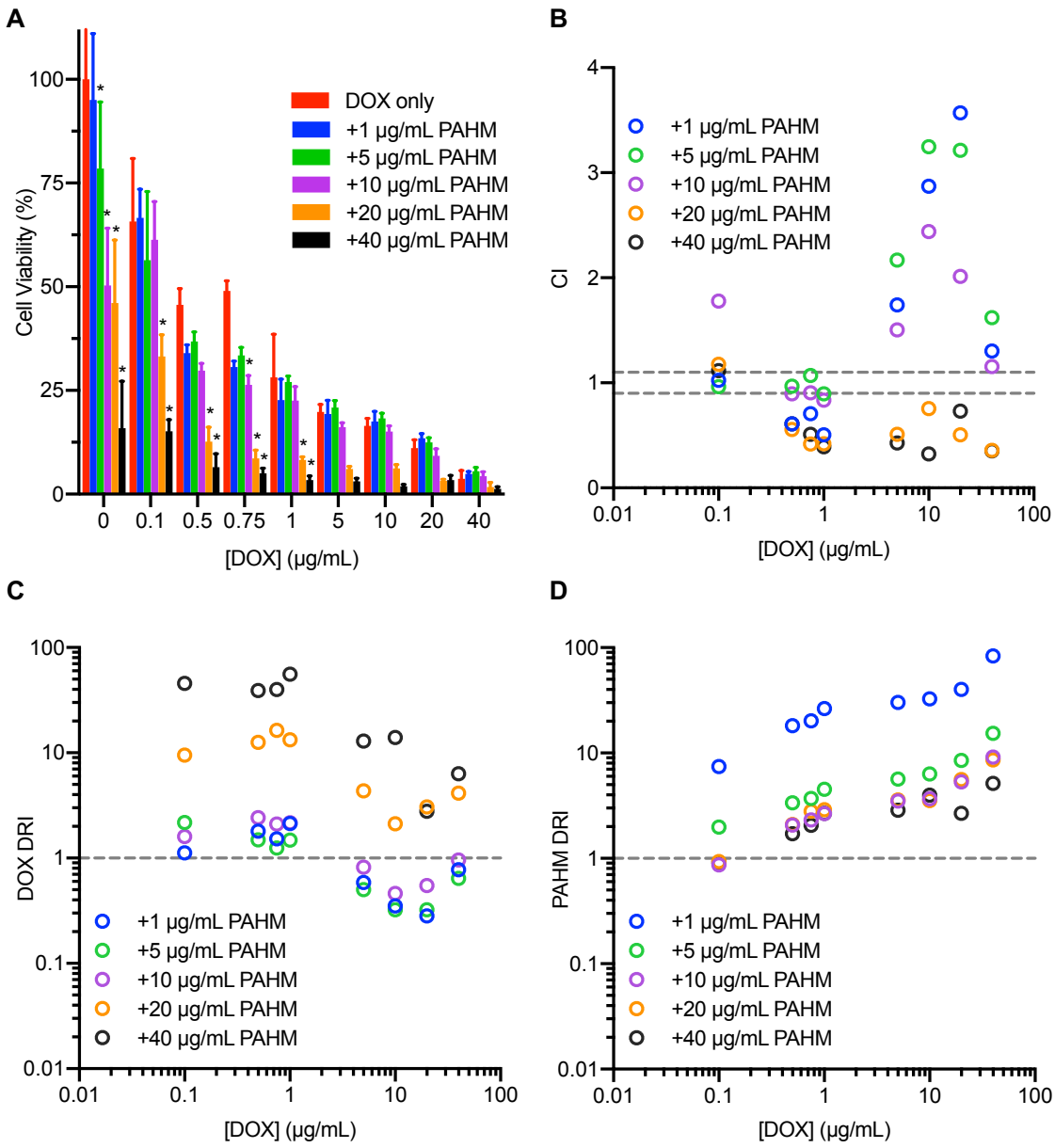

Figure 4.6 Synergistic killing of EMT6 cells is dependent on PAHM concentration. (A) Cell viability of EMT6 cells after 24 h exposure to DOX and PAHM. Data are shown as mean ± SD (n = 6 – 30). ANOVA with Tukey HSD test (* $p < 0.05$ vs DOX only). (B) Combination index analysis (CI <1, = 0.9 – 1 (dashed lines), >1 indicates synergism, nearly additive effect, and antagonism, respectively). Dose reduction index analysis for (C) DOX and (D) PAHM (DRI <1, =1 (dashed line), >1 indicates unfavorable dose reduction, no dose reduction, and favorable dose reduction, respectively).

AsPC-1 cells were also exposed to non-constant ratios of DOX and PAHM for 24 h. Similar to EMT6 cells, the viability of AsPC-1 cells was greatly reduced when combining DOX with 5 – 40 µg/mL PAHM (Figure 4.7A). However, the addition of 1 µg/mL

PAHM did not appear to kill more cells than DOX alone. The CI and DRI for each DOX and PAHM combination were also calculated to examine the synergistic killing of AsPC-1 cells.

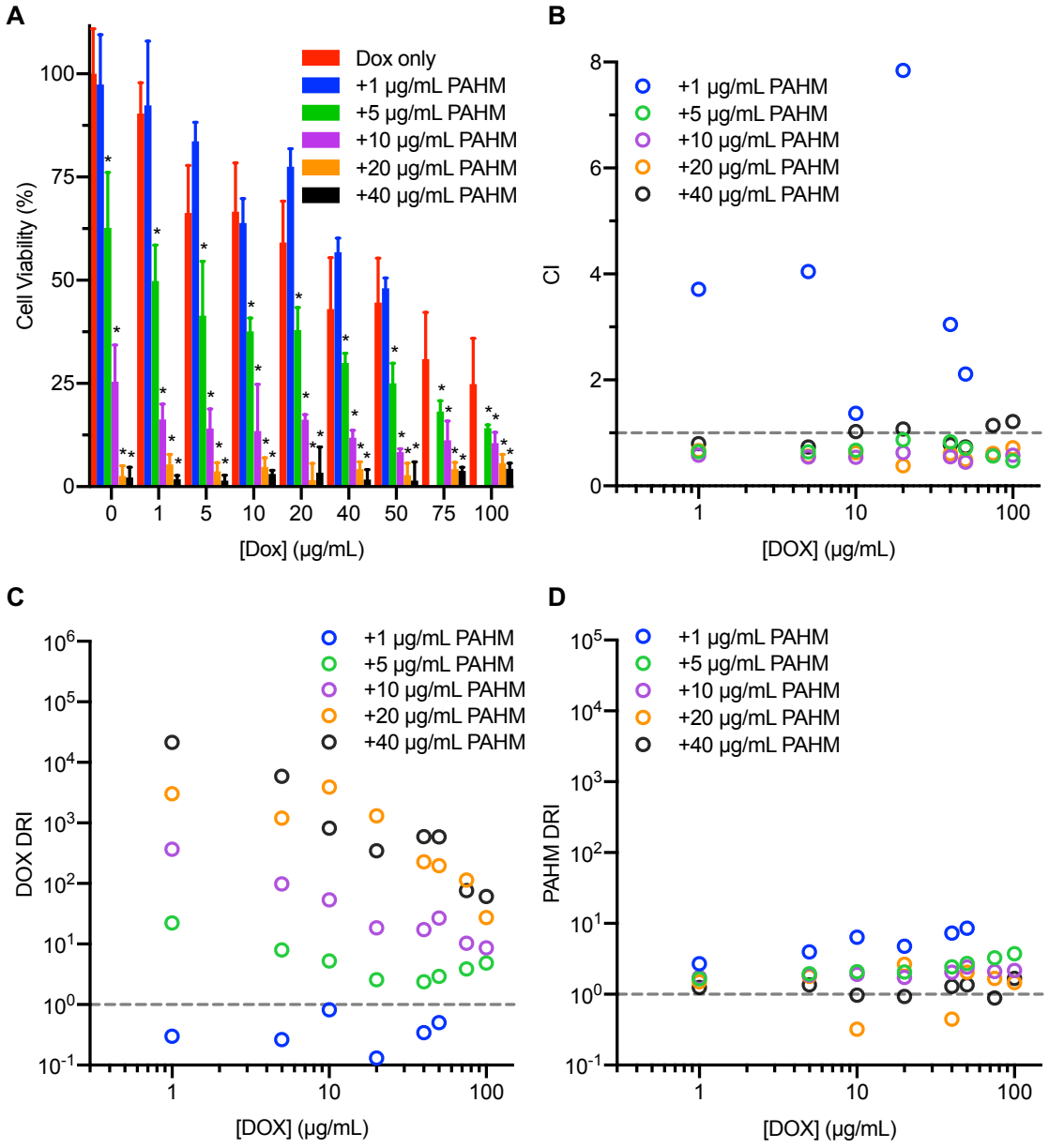

Figure 4.7 Synergistic killing of AsPC-1 cells is dependent on PAHM concentration. (A) Cell viability of AsPC-1 cells after 24 h exposure to DOX and PAHM. Data are shown as mean ± SD (n = 6 – 30). ANOVA with Tukey HSD test (* $p < 0.05$ vs DOX only). (B) Combination index analysis (CI <1, = 0.9 – 1 (dashed lines), >1 indicates synergism, nearly additive effect, and antagonism, respectively). Dose reduction index analysis for (C) DOX and (D) PAHM (DRI <1, =1 (dashed line), >1 indicates unfavorable dose reduction, no dose reduction, and favorable dose reduction, respectively).

As seen in Figure 4.7B, the CI tends to decrease with Fa. While the combinations with 1 μg/mL PAHM were antagonistic with CI ≥1.37, all combinations with 5 – 20 μg/mL PAHM were synergistic with CI ≤0.87. The DOX DRI follows a similar trend to the CI (Figure 4.7C). The DOX DRI tends to increase with Fa. While the DOX DRI are all <1 for 1 μg/mL PAHM, all combinations with 5 – 40 μg/mL PAHM gave DOX DRI >1. For 20 – 40 μg/mL PAHM, the DOX DRI was between 27.5 and 21414, indicating that the DOX dose can greatly be reduced when combined with PAHM. The PAHM DRI tends to decrease with PAHM concentration; however, for all combinations with 1 – 10 μg/mL PAHM and a majority of combinations with 20 – 40 μg/mL PAHM the PAHM DRI was >1 (Figure 4.7D).

4.3.5 Combination of DOX and PAHM shrinks 3D multicellular tumor spheroids

EMT6 multicellular tumor spheroids were exposed to DOX and PAHM separately, or in combination for day. At 1-day intervals, the tumor spheroids were imaged (Fig. 4.8A-C) and their size was measured (Fig 4.8D). The growth of the tumor spheroids was slowed, or in some cases inhibited, by PAHM treatment. Spheroids treated with 30 - 100 μg/mL of PAHM remained the same size over the 3 days. DOX treatment, however, was able to shrink the tumor spheroids. Spheroids treated with 0.6 - 2 μg/mL of DOX decreased in size over the 3 days. Perhaps most encouraging, most combinations of DOX and PAHM were more effective than either treatment alone. The greatest reduction in size was seen in tumor spheroids treated with 0.6 μg/mL of DOX and 30 μg/mL of PAHM, where spheroid size decreased by 26% by day 3.

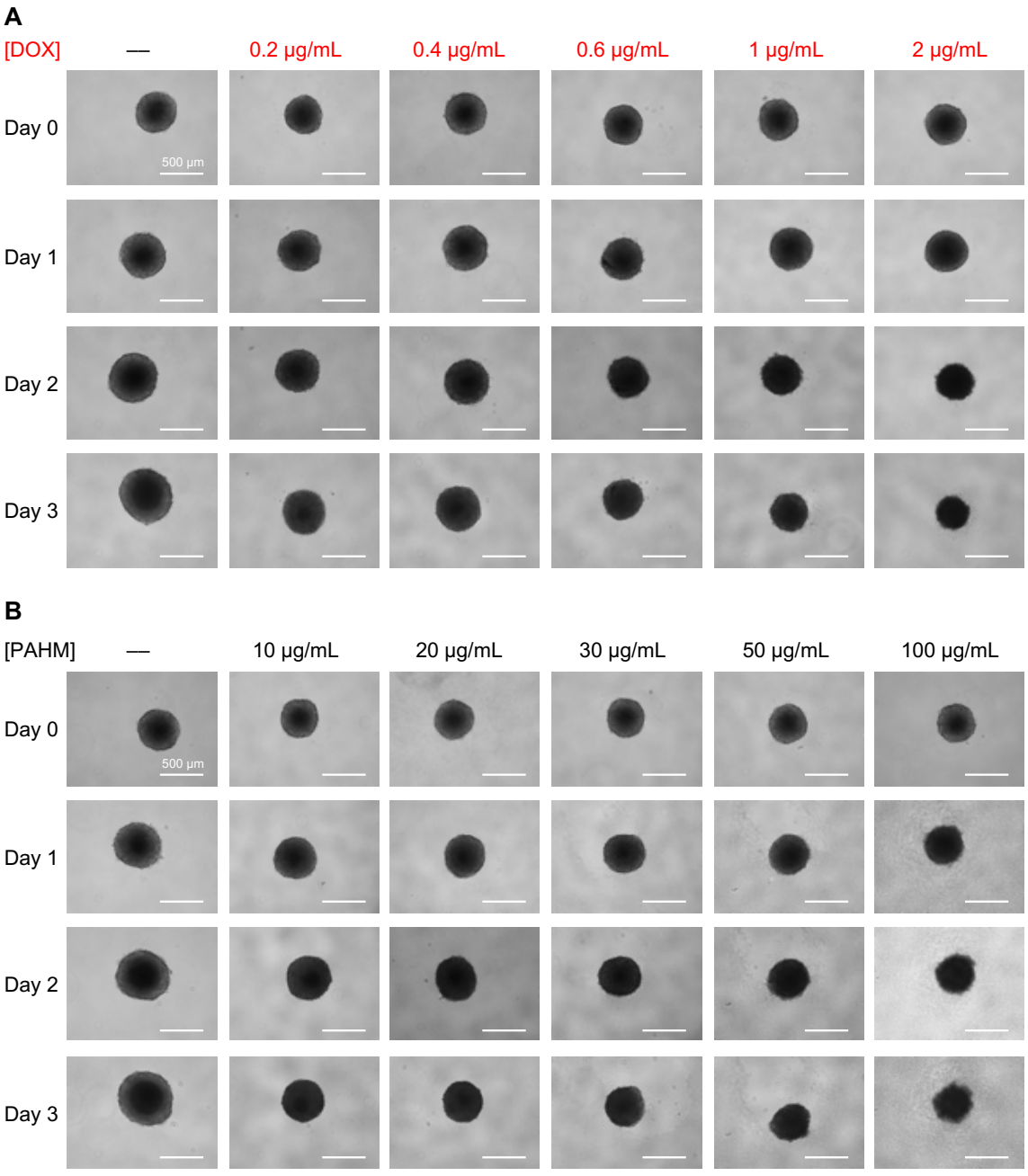
A
[DOX]
—
0.2 μg/mL
0.4 μg/mL
0.6 μg/mL
1 μg/mL
2 μg/mL
Day 0
Day 1
Day 2
Day 3
500 μm
B
[PAHM]
—
10 μg/mL
20 μg/mL
30 μg/mL
50 μg/mL
100 μg/mL
Day 0
Day 1
Day 2
Day 3
500 μm

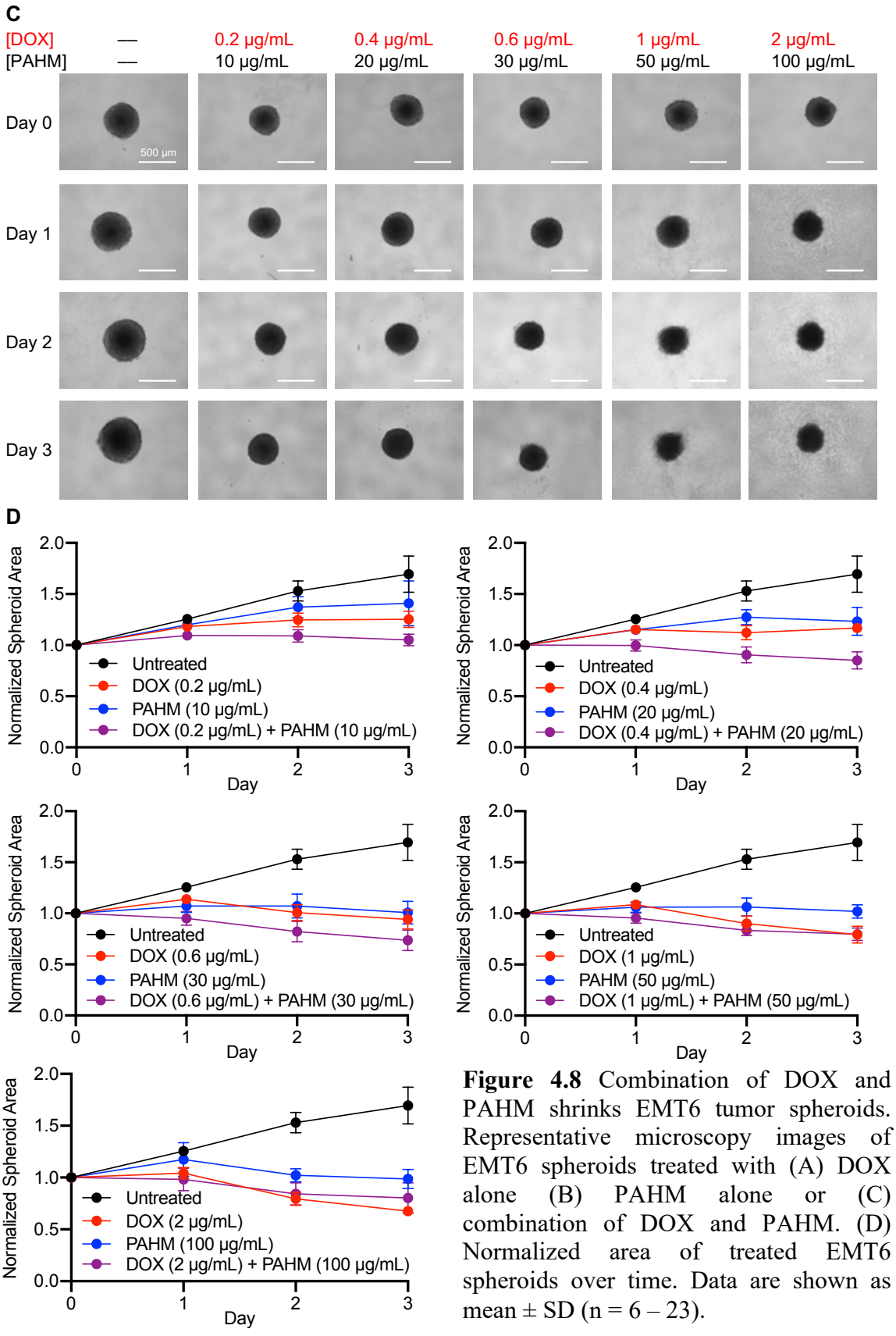

Figure 4.8 Combination of DOX and PAHM shrinks EMT6 tumor spheroids. Representative microscopy images of EMT6 spheroids treated with (A) DOX alone (B) PAHM alone or (C) combination of DOX and PAHM. (D) Normalized area of treated EMT6 spheroids over time. Data are shown as mean ± SD (n = 6 – 23).

4.4 Discussion

Most anticancer polymers (and peptides) are cationic amphipathic molecules that cause death by disrupting the cell membrane integrity [11]. Anticancer polymers first bind to highly negatively charged cancer cell membranes via electrostatic interactions, followed by disruption to the cell membrane by hydrophobic interactions [43]. While the exact mechanism of these hydrophobic interactions is not fully understood, various mechanisms have been proposed to describe the membrane disruption, including the barrel-stave model, toroidal model, carpet model, and detergent model [11]. The cationic amphipathic structure of PAHM is similarly capable of disrupting cancer cell membranes. Cationic primary amines in the side chain allow PAHM to bind to the anionic cell surface and the hydrophobic components can destabilize the membrane. PAHM-mediated membrane disruption occurs very quickly. PI staining revealed that EMT6 cell membranes were disrupted within 2 minutes after treatment with high PAHM concentration (50 - 75 μg/mL) (Figure 4.1). However, membrane disruption was concentration dependent. At lower PAHM concentration (10 - 30 μg/mL), not all EMT6 cells were PI+ and the onset time of membrane disruption was longer (~6 -7 min). This membrane disruption eventually leads to membrane lysis, allowing PAHM alone to effectively kill both EMT6 cells (Figure 4.4A) and AsPC-1 cells (Figure 4.5A).

In addition to its inherent cytotoxicity, PAHM also greatly enhances the anticancer activity of DOX. DOX kills cells by inducing DNA damage through topoisomerase II inhibition and free radical generation [39,126,127]. However, many cancer cells have developed resistance mechanisms that render DOX ineffective, including the overexpression of efflux pumps that pump the drug out of cell. PAHM-mediated

membrane disruption can overcome this resistance mechanism [41]. Pores in the cell membrane allow DOX to freely enter the cell faster than the efflux pumps can remove it, resulting in increased intracellular DOX accumulation (Figure 4.3). Thus, DOX can more effectively kill cells. In fact, DOX and PAHM synergistically kill both EMT6 cells (Figure 4.4C,D, Figure 4.6B) and AsPC-1 cells (Figure 4.5C, Figure 4.7B). However, this synergy was dependent on PAHM concentration. The 1:100 combinations of DOX and PAHM were much less synergistic than the 1:50 combinations, where twice as much PAHM was added (Figure 4.4C,D). This was further examined by combinations with non-constant ratio of DOX and PAHM. At low PAHM dose (≤10 μg/mL), DOX and PAHM did not synergistically kill EMT6 cells; however, higher PAHM doses (20 - 40 μg/mL PAHM) did display synergy (Figure 4.6B). Similar trends were seen in AsPC-1 cells treated by combinations with non-constant ratio of DOX and PAHM (Figure 4.7B). It appears that there is a threshold PAHM concentration that is required to induce enough membrane disruption for enough DOX to accumulate to kill cells synergistically. However, many of the combinations that did not display synergy still induced cell death in a dose-sparing manner. The DRI for nearly all tested combinations were greater than 1 (Figure 4.4E,F, Figure 4.5D, Figure 4.6C,D, Figure 4.7C,D), indicating that lower doses of DOX and PAHM can be used while maintaining the same cytotoxic effect. This dose reduction may also translate into clinical benefits including less toxic side effects, less cost, and higher patient compliance.

Despite the remarkable synergistic cytotoxicity of DOX and PAHM to AsPC-1 and EMT6 cells, monolayer cell culture assays have some limitations in their ability to predict the efficacy of anticancer agents in vivo. More specifically, these assays do not

recapitulate cell-cell and cell-extracellular matrix interactions exhibited in tumors [139]. In contrast, multicellular tumor spheroids are a better in vitro model because cell-cell interactions can be established. Additionally, the multicellular spheroids contain regions of peripheral cell proliferation (outer region) and nutrient deficient hypoxia regions (core), which is more similar to tumor structure in vivo [141]. To further test the toxicity of DOX and PAHM, we formed multicellular tumor spheroids from EMT6 cells. When used separately, both DOX and PAHM reduced the size of the EMT6 spheroids as compared to the untreated controls (Figure 4.8A,B). Although PAHM appears to only slow spheroid growth, spheroids treated with ≥0.6 μg/mL of DOX shrunk in size after 3 days. The combination of DOX and PAHM is even more effective, especially for the lower dose combinations (Figure 4.8D). In addition to differences in size, the mechanism of cell death appears to differ in spheroid treated with DOX or PAHM. Spheroids treated with PAHM alone (especially high concentrations of PAHM) released a lot of cellular debris, indicative of cell lysis (Figure 4.8B); however, spheroid treated with DOX (which induces apoptotic cell death [39]) did not release debris (Figure 4.8A). Spheroids treated with combinations of DOX and PAHM also released a lot of cellular debris (Figure 4.8C). The combination and cell lysis and apoptotic cell death may kill tumor cells more effectively.

Taken together, our results suggest that a synthetic membranolytic polymer, PAHM, can be used in combination with DOX to synergistically kill cancer cells. Future studies will test to ability of PAHM to synergize with other chemotherapy drugs. While the ability of the PAHM/DOX combinations to shrink multicellular tumor spheroids is encouraging, the efficacy of the combination therapy will need to be validated in

appropriate in vivo tumor models. Another future opportunity co-encapsulation and targeted delivery of both PAHM and DOX to tumors.

4.5 Conclusions

We have demonstrated that a synthetic membranolytic polymer, PAHM, when combined with DOX, led to enhanced killing of mouse breast cancer cells and human pancreatic cancer cells. PAHM-mediated membrane disruption led to increased intracellular accumulation of DOX. Nearly all tested combinations of PAHM and DOX caused cancer cell death in a dose-sparing manner, and combinations with sufficient PAHM concentration killed cells synergistically. Combination of PAHM and DOX also shrunk EMT6 multicellular tumor spheroids. These findings PAHM has the potential to improve the ability of chemotherapeutic drugs to treat multidrug resistant cancer cells.

Chapter 5 Combination of Irreversible Electroporation with Sustained Release of a Synthetic Membranolytic Polymer for Enhanced Cancer Cell Killing

5.1 Introduction

Electroporation is the process of delivering a series of short electrical pulses to create tiny defects or "pores" within a cell membrane. If theses pores are transient and the cell membrane is able to recover, the process is referred to as reversible electroporation (RE). On the other hand, irreversible electroporation (IRE) involves the use of high-voltage short electrical pulses to create permanent pores within a cell membrane, leading to cell death by membrane lysis or loss of homeostasis [46].While a common goal of RE is to increase the uptake of membrane-impermeable entities while minimizing cell injury [142], Davalos et al in 2005 proposed to use IRE as a way to kill cancer cells [143].

IRE is used clinically as a focal therapy to ablate tumors in the prostate, liver, pancreas, and kidneys [47,53,54]. In contrast to thermal ablation modalities that rely on extreme heating or cooling [50], IRE can be applied safely near large blood vessels or vital tissue structures [51]. It also spares the extracellular matrix, allowing for faster healing of healthy tissue while minimizing scarring [52]. Despite many advantages, IRE is usually considered a "last resort" for patients who do not respond to, or are not candidates for, other therapies [57]. A critical disadvantage of IRE is the inability to ablate large tumors (e.g. >3 cm in diameter) with an electric field strength that is safe to the patient [58]. IRE relies on two or more needle electrodes to deliver electric pulses. When the electric field intensity decreases sharply with the distance from an electrode [59] to the point below the effective threshold for IRE (500–1000 V/cm, depending on the cell type [46]), the cancer cells will only undergo RE and remain viable, resulting in

incomplete tumor ablation [60]. While it is possible to increase the ablation volume by applying high voltages, doing so carries the risk of damaging adjacent healthy tissue [61,62] and generate excessive heat near the electrodes due to Joule heating [63]. Repeated IRE treatments can be performed, attempting to fully ablate a tumor, but this is impractical under most clinical settings [47,54].

Lowering the electric field threshold for cancer cell killing is an appealing approach to achieving large tumor ablation volume without using dangerously high voltage. Numerous reports show that cells treated with cationic molecules (such as procaine, tetracaine, lidocaine, and polyarginine), sodium dodecyl sulfate (SDS, a small-molecule surfactant) and dimethyl sulfoxide (DMSO, a polar aprotic solvent) can be killed by IRE at moderate electric field strengths [46,58,64–66]. The explanation of this effect is that the cations interact electrostatically with the anionic cell membrane, making it easier for IRE-induced pores to form [64,66], whereas surfactants and DMSO interact with membrane lipids to alter the membrane's edge line and surface tension, making it more difficult for pores to reseal [58]. It is important to note that with the exception of polyarginine, none of these IRE sensitizers are cytotoxic themselves.

Certain cationic peptides and synthetic polymers show membranolytic activity towards mammalian cells and are being investigated as anticancer agents [11,129,133,138]. Synthetic polymers may have advantages over peptides due to their chemical and biological stability, flexibility in structure, and the ease of synthesis on a large scale [11,133]. However, to our knowledge, combining synthetic membranolytic polymers with IRE for cancer treatment has not been attempted. Here we postulate that one such polymer, poly(6-aminohexyl methacrylate) (PAHM), will not only serve as an

IRE sensitizer by lowering the electric field threshold, but also synergizes with IRE to achieve greater cell killing due to its own cytotoxicity through membrane lysis (Figure 5.1). We further recognize the need for localized and sustained delivery of PAHM to maximize cancer cell killing while avoiding damage to healthy cells. To this end, we set out to develop a method of sustained release of PAHM from the surface of polymer microspheres (Figure 5.1), which are already widely used clinically as embolic agents to treat local solid tumors [144]. In this paper, the killing of human pancreatic cancer cells by IRE and the membranolytic PAHM, applied separately or in combination, was evaluated. Embolic microspheres coated with PAHM were prepared and the release of PAHM was demonstrated. Finally, the combined effect of cancer cell killing by IRE and PAHM delivered by the embolic microspheres was analyzed.

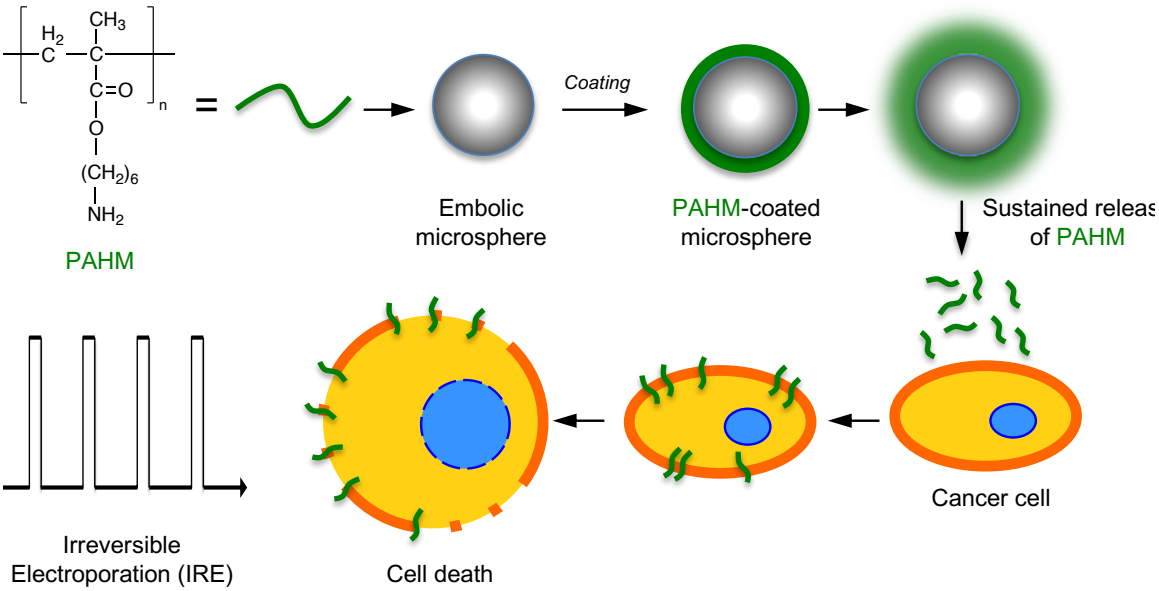

Figure 5.1 Schematic illustration of the combined killing of cancer cells by a synthetic membranolytic polymer (PAHM) and IRE. PAHM is coated onto embolic microspheres and then released to interact with cell membrane and sensitize the cells to IRE-induced membrane disruption and cell death.

5.2 Materials and Methods

5.2.1 Chemicals and reagents

Roswell Park Memorial Institute (RPMI) 1640 medium, fetal bovine serum (FBS), Penicillin-Streptomycin (10,000 U/mL; 10,000 μg/mL), Dulbecco's phosphate buffered saline (DPBS), phosphate buffered saline (PBS, pH 7.4), trypsin-EDTA (0.25%), trypan blue (0.4% solution, 0.85% NaCl), MTT (3-(4,5-dimethylthiazol- 2-yl)-2,5-diphenyltetrazolium bromide) (MTT), dimethyl sulfoxide (DMSO), ethanol (200 proof), Alexa Fluor 488 NHS Ester, sodium bicarbonate, and N,N-dimethylformamide (DMF) were purchased from Thermo Fisher Scientific (Waltham, MA). Hydroxlamine hydrochloride and PD-10 desalting columns (Sephadex G-25 medium; exclusion limit: M_r 5000) were purchased from Millipore Sigma (Burlington, MA). Electroporation cuvettes (4 mm gap) were from Harvard Apparatus (Holliston, MA). UV transparent cuvettes (semi-micro, 1.5 mL) were purchased from USA Scientific (Ocala, FL).

5.2.2 Synthesis of poly (6-amino-1-hexyl methacrylate) (PAHM)

N-(tert-butoxycarbonyl) aminohexyl methacrylate (tBocAHM) was synthesized as described by Zhu et al [136]. PAHM was synthesized via atom transfer radical polymerization (ATRP) of tBocAHM followed by deprotection of the tBoc side chains based on a method reported by Ji et al [137]. The polymer was characterized using ^{1}H NMR and gel permeation chromatography (GPC) as described by Ji [138]. The PAHM used in the subsequent experiments had a number-average molecular weight (M_n) of 2.08 $\times 10^4$, Dispersity (Đ) of 1.26, and average degree of polymerization (DP) of 100.

5.2.3 Fluorescence labeling of PAHM

PAHM was fluorescently labeled with the NHS ester of Alexa Fluor 488 dye ($\lambda_{ex}/\lambda_{em}$: 494/517 nm; extinction coefficient = 71,000 $cm^{-1}M^{-1}$) according to manufacturer's protocol. Briefly, PAHM was dissolved in sodium bicarbonate buffer (0.1 M, pH 8.3) to a concentration of 10 mg/mL. Alexa Fluor 488 was dissolved in DMF to a concentration of 10 mg/mL. In a 1.8 mL amber glass vial, 100 µL Alexa Fluor 488 solution (10 mg/mL) was slowly added to 1 mL PAHM solution (10 mg/mL). Reaction was carried out for 1 h at room temperature (protected from light) with continuous stirring. Reaction was terminated by adding 100 µL hydroxylamine hydrocholoride solution (1.5 M, pH 8.5), followed by stirring for 1 h at room temperature. Theoretical degree of labelling was 1% based on feed ratio and 25-33% labelling efficiency (per manufacturer). Unreacted dye was removed by gel filtration with a PD-10 desalting column (Sephadex G-25 medium; exclusion limit: M_r 5000) equilibrated with deionized water. The purified fluorescently labeled PAHM solution was frozen at -80º C overnight and lyophilized under 0.020 mBar for 4 days in a FreeZone ® Freeze Dry System (Labconco, Kansas City, MO) equipped with a Maxima™ C Plus Vacuum Pump (Model M8c, Themo Fisher Scientific, Waltham, MA). Dried polymer was stored in a vacuum desiccator at room temperature (protected from light) until use.

5.2.4 Optimizing method of coating embolic microspheres with PAHM

PMMA microspheres with average diameter 71 µm or 100 µm were provided by Boston Scientific Corporation (Maple Grove, MN). PMMA microspheres were coated with PAHM by a solvent evaporation method. A mixture of fluorescently labeled and unlabeled PAHM (1:8 ratio of labeled:unlabeled) was dissolved in ethanol at total

concentration of 0.1 mg/mL or 0.5 mg/mL. In 2 dram glass vials, 1 mL PAHM solution was added to 50 mg PMMA microspheres (100 μm in diameter). Vials were placed uncovered on a slowly rotating orbital shaker (Lab-Line Instruments, Melrose Park, IL) at room temperature for 3 days to evaporate the ethanol. Based off the feed ratio, after drying the microspheres were coated with PAHM at a concentration of 2 μg/mg or 10 μg/mg (μg PAHM/mg PMMA). Coated microspheres were stored in a vacuum desiccator (Bel-Art™ Space Saver Vacuum Desiccator 140 mm, Thermo Fisher Scientific, Waltham, MA) until use.

To optimize and speed up the coating process, PMMA microspheres were coated with PAHM by three different solvent evaporation methods. A mixture of fluorescently labeled and unlabeled PAHM (1:8 ratio of labeled:unlabeled) was dissolved in ethanol at total concentration of 0.8 mg/mL. In 2 dram glass vials, 0.5 mL PAHM solution was added to 100 mg PMMA microspheres (100 μm in diameter). For coating method 1, ethanol was evaporated as described above (3 days on a slowly rotating orbital shaker). For coating method 2, uncovered vials were placed within a vacuum desiccator on top of a slowly rotating orbital shaker for 12 h. For coating method 3, ethanol was evaporated with compressed air for 10 min. The glass vials were covered with rubber septa with two puncture holes. A glass Pasteur pipette was pushed through the inlet hole to deliver the compressed air and a needle (21 gauge, 1" length) was pushed through the outlet hole to avoid pressure buildup and allow evaporated ethanol to escape. The compressed air-dried microspheres were then stored overnight in an isotemp vacuum oven (Model 280A, Thermo Fisher Scientific, Waltham, MA) connected to vacuum pump (Maxima D2A Rotary Vane Dual Stage Vacuum Pump, Thermo Fisher Scientific, Waltham, MA) to

evaporate any residual ethanol (room temperature, -29 inHg). Coated microspheres were stored in a vacuum desiccator (Bel-Art™ Space Saver Vacuum Desiccator 140 mm, Thermo Fisher Scientific, Waltham, MA) until use.

To visualize the PAHM coating, coated microspheres were placed on glass slides. Fluorescent and bright-field images of the coated microspheres were acquired with an Olympus IX70 inverted fluorescence microscope equipped with an Olympus DP72 camera and X-Cite 120 Wide-Field Fluorescence Microscope Excitation Light Source (Excelitas Technologies, Waltham, MA). Fluorescently labeled PAHM was visualized using an excitation wavelength of 480 ± 50 nm and emission wavelength of 535 ± 50 nm. An exposure time of 10 ms was selected for image capture to minimize microsphere autofluorescence. The fluorescence intensity of the PAHM on individual coated microspheres was quantified using ImageJ.

All subsequent experiments (PAHM release kinetics and cytotoxicity assays) used microspheres coated with unlabeled PAHM at concentration of 10 μg/mg (μg PAHM/mg PMMA). PAHM was dissolved in ethanol at a concentration of 1 mg/mL. In 4 mL glass vials, 1 mL PAHM solution was added to 100 mg microspheres (71 μm or 100 μm). Ethanol was evaporated using method 1 as described above. Coated microspheres were stored in a vacuum desiccator (Bel-Art™ Space Saver Vacuum Desiccator 140 mm, Thermo Fisher Scientific, Waltham, MA) until use.

5.2.5 In vitro release kinetics from coated microspheres

The release of PAHM from coated microspheres was examined by suspending 25 mg coated microspheres (71 μm or 100 μm in diameter) in 1 mL release medium (cell culture medium without phenol red) in 12-well plates. The coated microspheres were incubated

in a humidified environment at 37ºC with 5% CO_2 for 1 week. At particular time points, 750 µL of the supernatant was sampled and replaced with fresh release medium. The sampled supernatants were then diluted with 0.75 mL release medium (final volume: 1.5 mL) in UV transparent cuvettes. The amount of PAHM in the supernatant was measured by measuring absorbance at 245 nm using a Cary 100 UV-Vis Spectrophotometer (Agilent Technologies, Santa Clara, CA). Release kinetic profiles were expressed as the cumulative percentage released over time.

5.2.6 Cell culture

Human pancreatic adenocarcinoma cell line AsPC-1 were obtained from ATCC. AsPC-1 cells were cultured in a medium consisting of RPMI 1640 medium with 2 g/L glucose, 2 mM L-glutamine, 2 g/L sodium bicarbonate, 10% heat inactivated fetal bovine serum (FBS), 100 U/mL penicillin, and 100 µg/mL streptomycin. AsPC-1 cells were cultured in tissue culture flasks and incubated in a humidified environment at 37ºC with 5% CO_2. When cells reached ~80% confluency the culture medium was removed, cells were rinsed with DPBS, and 0.25% trypsin-EDTA was added for 5 min to detach cells from the flasks. Detached cells were split 1:3 to 1:6 to continue culture or used immediately for cytotoxicity experiments.

5.2.7 Cytotoxicity of IRE in combination with free PAHM or PAHM released from coated microspheres

Harvested cells were centrifuged at 200 x *g* for 5 min and supernatant was discarded. Cell pellets were resuspended in cell culture medium (without phenol red) and a 100 µL aliquot was stained 1:1 with trypan blue 0.4% solution and counted using a hemocytometer (Sigma-Aldrich, St. Louis, MO) and inverted microscope (Thermo Fisher

Scientific, Waltham, MA). Cell suspensions were diluted to density of 675,000 cells/mL in culture medium (without phenol red) and 1 mL aliquots were dispensed into 2 mL microcentrifuge tubes.

Free PAHM was dissolved in cell culture medium (without phenol red) to an initial concentration of 250 μg/mL and diluted to varying concentrations. To the 1 mL cell suspensions, 0.5 mL PAHM dilutions were added to give final concentrations of 0 – 50 μg/mL. Coated microspheres (71 or 100 μm in diameter) were suspended in cell culture medium (without phenol red) to an initial concentration of 25 mg/mL and diluted to varying concentrations. To the 1 mL cell suspensions, 0.5 mL coated microsphere dilutions were added to give final concentrations of 0 – 5 mg/mL (corresponding to of 0 – 50 μg/mL microsphere-coated PAHM).

After 15 min incubation, cells were treated with IRE as described previously [145]. Briefly, 400 μL prepared cell suspension was pipetted into an electroporation cuvette (BTX 45-0126, Harvard Apparatus, Holliston, MA) between the two aluminum plate electrodes (4 mm apart). The cuvette was placed in an external electric field created by an electric pulse generator (BTX ECM Square Wave Electroporation System, BTX Model No. 830, Harvard Apparatus, Holliston, MA) which delivered 50 electrical pulses (100 μs pulse duration, 1 Hz frequency) at 150, 225, 300, 375, or 450 V (corresponding to electric field strengths of 375, 562.5, 750, 937.5, or 1125 V/cm).

For 15 min exposure time samples, 400 μL treated cell suspensions were pipetted into 2 mL microcentrifuge tubes. Cells suspensions were centrifuged at 185 x *g* for 5 min and supernatants were discarded. PAHM was washed away from cells with 1 mL DPBS (twice). Cell pellets were resuspended in 1 mL cell culture medium (without phenol red)

and plated in 12-well plates (180,000 cells/well). For 4 h and 24 h exposure time samples, 400 µL treated cell suspensions were plated into 12-well plates (180,000 cells/well) and 600 µL free PAHM or coated microsphere dilutions were added to maintain free PAHM or microsphere-coated PAHM concentrations of 0 – 50 µg/mL. After 4 h or 24 h incubation in a humidified environment at 37ºC with 5% CO_2 cells were washed with 1 mL DPBS (twice) and given 1 mL fresh cell culture medium (without phenol red).

Cell viability was evaluated using an MTT (3-(4,5-dimethyl-thiazol-2-yl)-2,5-diphenyl tetrazolium bromide) assay [122]. For all exposure time samples, 100 µL MTT solution (5 mg/mL in DPBS) was added to each well. After 4 h incubation in a humidified environment at 37ºC with 5% CO_2, 850 µL medium was removed from each well. Formazan crystals were dissolved in 1 mL DMSO and absorbance was measured at 540 nm using a BioTek Cytation 3 Cell Imaging Multi-Mode Reader (BioTek Instruments, Winooski, VT). Cell viability was determined by normalizing by the absorbance of untreated cells (with the same exposure time).

5.2.8 COMPUSYN modeling of drug synergy

For each combination of IRE and free PAHM or IRE and PAHM released from coated microspheres, the combination index (CI) and dose reduction index (DRI) were calculated by the Chou-Talalay method with the CompuSyn software program (ComboSyn Inc., Paramus, NJ) [135]. Input parameters were the dose of each treatment (alone or in combination) and the corresponding fractional affect (Fa) – the fraction of cell growth inhibited by a particular dose, calculated as Fa = (100% - cell viability / 100%). The dose-effect relationship for IRE, free PAHM, or PAHM released from coated microspheres and their combinations are described by the Median-Effect Equation Fa/Fu

$= (D/D_m)^m$, where Fu is the unaffected fraction of cell growth (Fu = 1 – Fa), D is the dose required to produce Fa, D_m is the median-effect dose (i.e. IC_{50}), and m is the dynamic order of the curve. Using these parameters, the CI and DRI can be calculated. The CI value is dimensionless quantification of drug interaction, calculated as $CI = (D)_1/(D_x)_1 + (D)_2/(D_x)_2$, where $(D_x)_1$ is the dose of single drug D_1 (i.e. IRE electric field strength) "alone" that inhibits cell growth by x%, $(D_x)_2$ is the dose of a second drug D_2 (i.e. PAHM concentration) "alone" that inhibits cell growth by x%, and $(D)_1$ and $(D)_2$ are the doses "in combination" that also inhibit cell growth by x%. CI = 1 indicates an additive effect; CI < 1 indicates a synergistic effect; CI > 1 indicates an antagonistic effect. The DRI is a measure of how much the dose of each drug can be reduced if used in combination at a given Fa as compared to the dose of each drug alone, calculated as $(DRI)_1 = (D_x)_1/(D)_1$ and $(DRI)_2 = (D_x)_2/(D)_2$. DRI = 1 indicates no dose reduction; DRI > 1 indicates favorable dose reduction, DRI < 1 indicates unfavorable dose reduction.

5.2.9 Statistical analysis

ANOVA and Tukey HSD test for multiple comparisons were used to determine the significance of difference in cell viability between different treatment groups. ANOVA and Tukey HSD test for multiple comparisons were used to determine the significance of difference in fluorescence intensity of PAHM on coated microspheres. PAHM release profiles were fit with a two-phase exponential association model. All analyses were performed using GraphPad prism, version 9.0.0 (GraphPad software Inc., San Diego, California, USA).

5.3 Results

5.3.1 Tumor cell killing by IRE and PAHM applied individually

Human pancreatic cancer cells (AsPC-1) were exposed to various doses of IRE or PAHM and cell viability was determined at various time points. As expected, higher electric field strengths led to lower cell viability (Figure 5.2A). For cells exposed to 750 V/cm and below, over 70% of the cells remained viable. Even the highest electric field strength (1125 V/cm) only killed 68% of cells after 24 h. In comparison, PAHM had a more potent dose-dependent cell killing effect (Figure 5.2B). Greater than 85% of cells were killed when exposed continuously to ≥25 μg/mL of PAHM for 24 h. With 40 or 50 μg/mL of PAHM 100% of the cells were dead after 24 h. Incubating the cells for 24 h after IRE treatment had no influence on cell viability with the exception of 1125 V/cm, which caused more cell death at 24 h than 4 h (Figure 5.2A). In contrast, cell killing by PAHM increased with exposure time (Fig. 2B). Interestingly, treating cells with PAHM for 4 h appears to result in lower cell viability than treating cells for 24 h. At PAHM doses ≤20 μg/mL, there was a significant reduction in cell viability after 4 h of exposure, but the cells appeared to recover after 24 h. However, at PAHM doses ≥25 μg/mL, this recovery did not occur, as there was no statistically significant difference in cell viability between 4 h and 24 h of exposure.

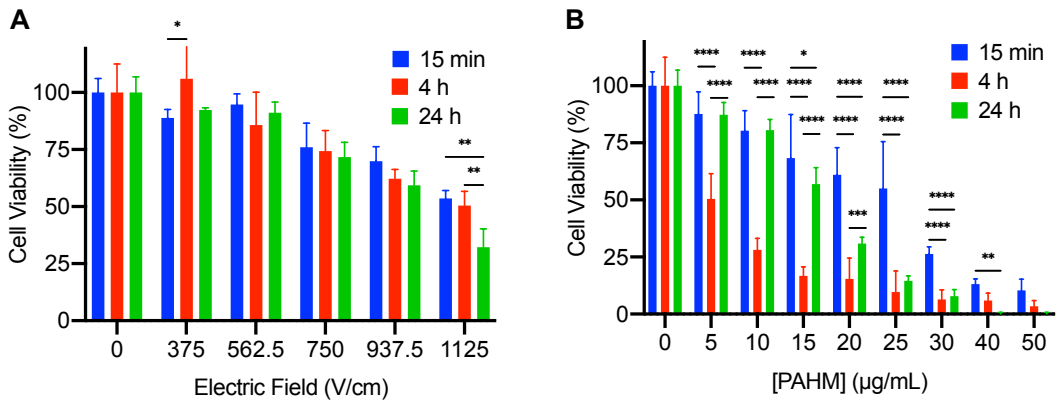

Figure 5.2 Cell viability after (A) IRE or (B) PAHM treatment applied separately. Data are shown as mean ± SD (A) (n = 4 – 6) (B) (n = 9 – 13). ANOVA with Tukey HSD test (* p <0.05, ** p <0.01, *** p<0.001, **** p<0.0001).

5.3.2 Enhanced tumor cell killing by IRE/PAHM combinations

To evaluate the ability of PAHM to enhance the cell killing effect by IRE, two electric field strengths of IRE were combined with three PAHM doses and cell viability was assessed at various time points (Figure 5.3A – C). For all exposure times, combining PAHM with IRE resulted in significantly more cell death. For example, while IRE treatment at 562.5 V/cm alone did not result in any appropriable cell death (95% viability), subsequent exposure to non-lethal doses of 5, 15, and 25 µg/mL of PAHM for 15 min reduced cell viability to 64%, 48%, and 33%, respectively (Figure 5.3A). The trend remained constant and was more pronounced with 4 and 24 h of exposure to PAHM (Figure 5.3B). Notably, despite cell recovery after 24 h, combined treatment of IRE at 562.5 V/cm and non-lethal doses of PAHM (5, 15, and 25 µg/mL) reduced cell viability to 72%, 17%, and 3%, respectively (Figure 5.3C). Similar effect was observed with IRE at the higher 912.5 V/cm (Figure 5.3A – C).

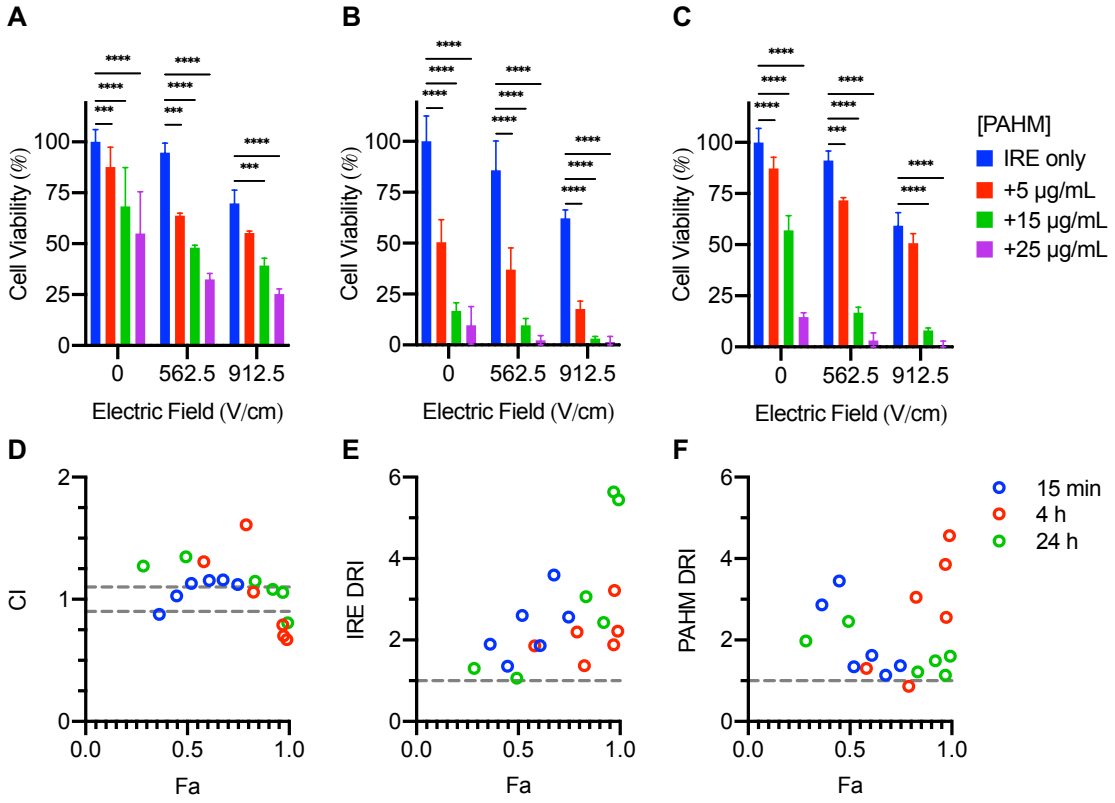

Figure 5.3 Cell viability after IRE treatment combined with PAHM exposure for (A) 15 min (B) 4 h (C) 24 h. Data are shown as mean ± SD (n = 3 - 12). ANOVA with Tukey HSD test (* p <0.05, ** p <0.01, *** p<0.001, **** p<0.0001). (D) Combination index analysis (CI <1, = 0.9 - 1 (dashed lines), >1 indicates synergism, nearly additive effect, and antagonism, respectively). Dose reduction index analysis for (E) IRE and (F) PAHM (DRI <1, =1 (dashed line), >1 indicates unfavorable dose reduction, no dose reduction, and favorable dose reduction, respectively).

5.3.3 PAHM sensitizes tumor cells for destruction by low-dose IRE

To further examine the enhancement of IRE by PAHM, the Combination Index (CI) and Dose Reduction Index (DRI) for each IRE/PAHM combination were calculated by the Chou-Talalay method [135]. The CI is plotted against the fractional affect (Fa), the fraction of cell growth inhibited by a particular combination of IRE and PAHM (Figure 5.3D). For 15 min PAHM exposure, the combination of IRE and PAHM appears to be slightly antagonistic as a majority of the CI are greater than 1.12. At longer PAHM exposure, the CI tends to decrease at higher Fa. For 4 h PAHM exposure, the combinations with the three highest Fa appear to be synergistic. For 24 h PAHM

exposure, combinations with lower Fa displayed slight to moderate antagonism; however, combinations with higher Fa are nearly additive or display moderate synergy. The DRI of IRE tends to increase with Fa for all three exposure times and all DRI are greater than 1 (Figure 5.3E). This indicates that for any combination with PAHM, a lower electric field strength can kill an equivalent fraction of cells as a higher electric field strength alone. The DRI of PAHM for all but one combination are greater than 1 (Figure 5.3F), indicating the PAHM dose can also be reduced when used in combination. For 15 min and 24 h exposure the DRI tends to decrease with Fa; however, the DRI tends to increase with Fa for 4 h exposure to PAHM.

5.3.4 Coating PAHM onto embolic microspheres

Embolic PMMA microspheres (100 μm in diameter) were coated with fluorescently labeled PAHM by a solvent evaporation method. Representative fluorescent micrographs (Figure 5.4A) show that increasing the concentration of PAHM resulted in a thicker coating as microspheres coated with 10 μg PAHM/mg PMMA showed 10.5-fold brighter fluorescence than microspheres coated with 2 μg/mg (μg PAHM/mg PMMA) (Figure 5.4B).

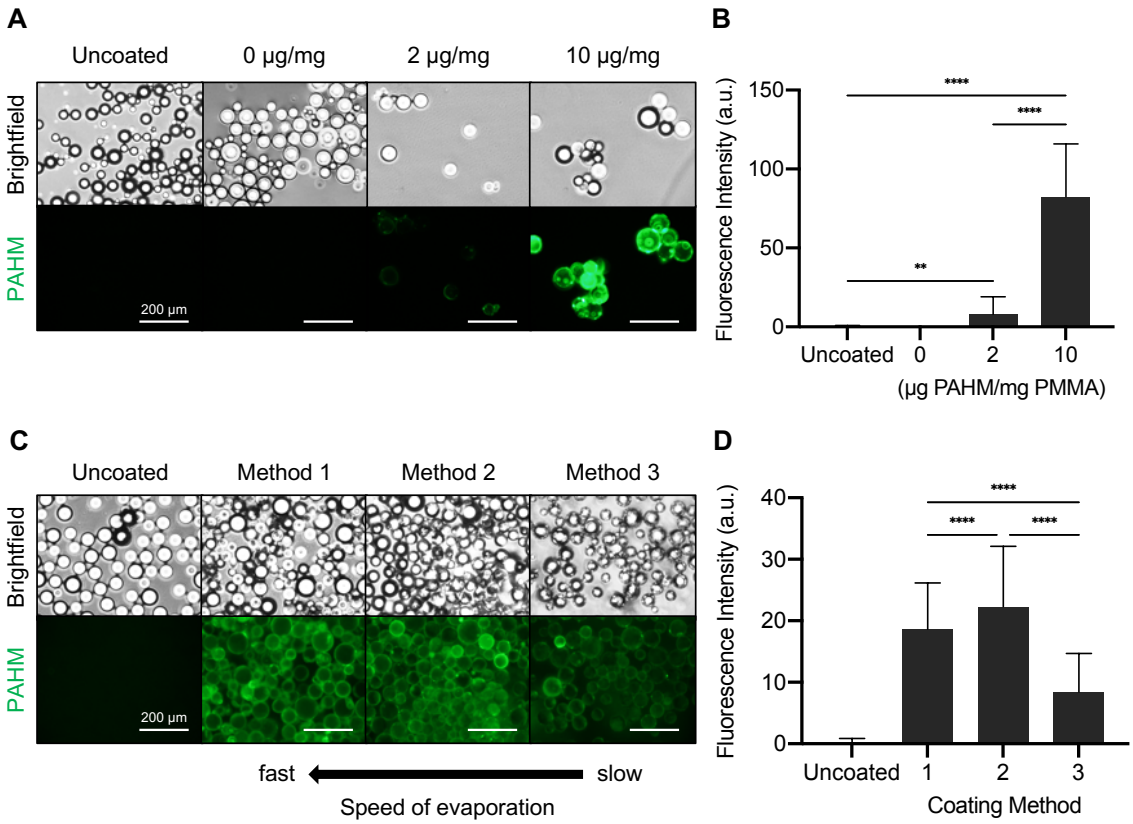

Figure 5.4 Characterization of embolic microspheres coated with fluorescently labeled PAHM. (A) Representative fluorescence microscopy images of microspheres coated with different amounts of PAHM (µg PAHM/mg PMMA). (B) Fluorescence intensity of PAHM coating on individual microspheres. (C) Representative fluorescence microscopy images of microspheres coated with PAHM by different solvent evaporation methods. (D) Fluorescence intensity of PAHM on individual microspheres after coating by different methods. Data are shown as mean ± SD (A) (n = 16 – 63) (B) (n = 165 – 186). ANOVA with Tukey HSD test (* $p < 0.05$, ** $p < 0.01$, *** $p < 0.001$, **** $p < 0.0001$).

To optimize the coating process, embolic microspheres were coated with 4 µg PAHM/mg PMMA fluorescently labeled PAHM by three different solvent evaporation methods. Representative fluorescent micrographs of microspheres after coating are shown in Figure 5.4C and quantification of the fluorescence intensity is shown in Figure 5.4D. In method 1, ethanol was quickly evaporated within 10 min which resulted in a bright, relatively uniform coating (Figure 5.4C). In method 2, the slower evaporation of ethanol over 12 h seemed to slightly increase the amount of PAHM coated on the microspheres, as indicated by the 1.2-fold brighter fluorescence as compared to method 1

(Figure 5.4D). However, further slowing the evaporation to 3 days (method 3) resulted in a much dimmer coating (Figure 5.4C,D). We chose to use method 1 to coat microspheres for all subsequent experiments because it was fast while still generating a good coating.

5.3.5 Sustained release of PAHM from microspheres

Microspheres (71 µm or 100 µm in diameter) coated with 10 µg PAHM/mg PMMA were submerged in cell culture medium to evaluate the release kinetics of coated PAHM (Figure 5.5). PAHM release was quantified by UV-Vis absorption (Figure 5.6). PAHM was released slightly faster from 71 µm PMMA microspheres than 100 µm. After an initial burst within the first 4 h, 69% and 59% of coated PAHM was released from 71 µm and 100 µm PMMA microspheres. Subsequently a sustained release of over 20% of coated PAHM continued over the course of 1 week (between days 2 and 7).

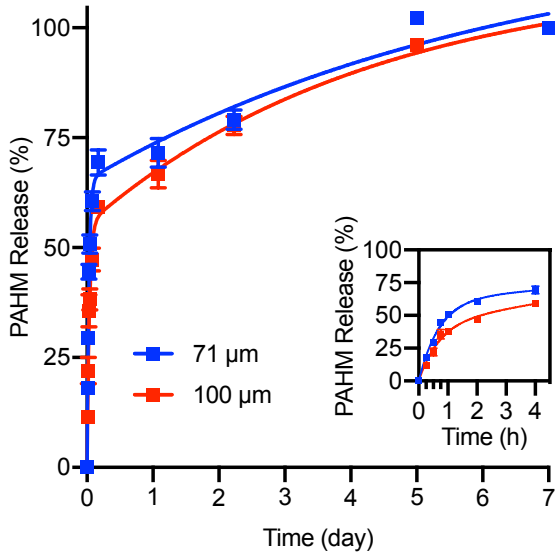

Figure 5.5 Release kinetics of PAHM from coated embolic microspheres in cell culture medium at 37ºC. Data are shown as mean ± SD (n = 4) and are fit with a two-phase exponential association model.

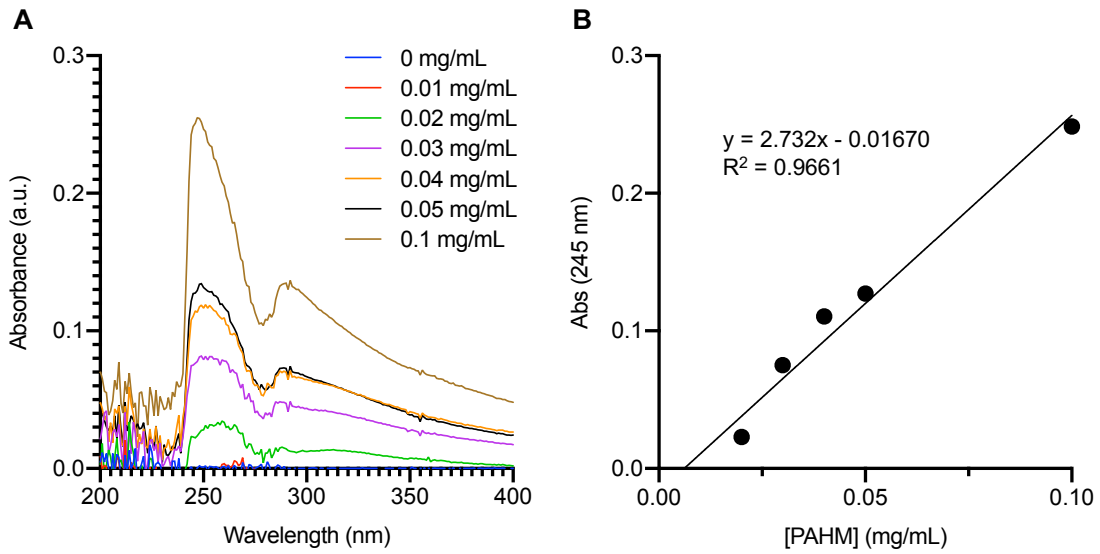

Figure 5.6 Quantification of PAHM in cell culture medium. (A) UV-Vis absorption spectra of aqueous PAHM solution of various polymer concentrations. (B) Standard curve showing absorbance at 245 nm vs. PAHM concentration.

5.3.6 Tumor cell killing by PAHM released from microspheres

The viability of AsPC-1 cells after exposure to microspheres coated with 10 µg PAHM/mg PMMA is shown in Figure 5.7. PMMA microspheres alone show little to no toxicity (Figure 5.8). Similar to free PAHM, the exposure time to PAHM released from 71 µm microspheres had a significant effect on cell viability (Figure 5.7A). Fifteen minutes of exposure to the highest dose (50 µg/mL) of microsphere-coated PAHM killed 47% of cells. Exposure for 4 h, however, greatly reduced cell viability – less than 13% of the cells were alive after treatment with ≥20 µg/mL microsphere-coated PAHM. The cells recovered much of their viability after 24 h, thus only the highest dose (50 µg/mL) of microsphere-coated PAHM achieved more cell killing than at shorter time frames. Similar dose-dependent cell killing was observed for 100 µm microspheres, although the time dependence of killing was not as prominent as compared to 71 µm microspheres (Figure 5.7B).

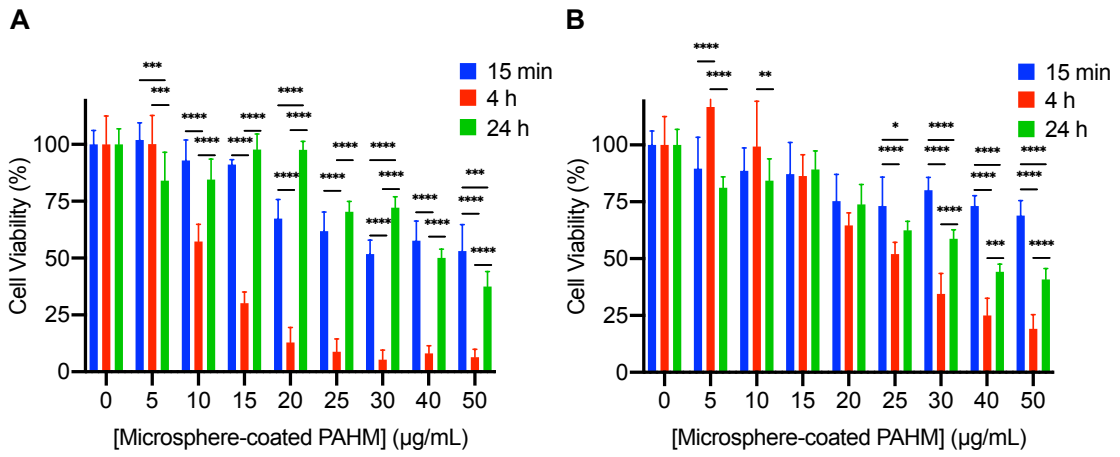

Figure 5.7 Cell viability after exposure to PAHM released from coated embolic microspheres with average diameter (A) 71 µm (B) 100 µm. Data are shown as mean ± SD (n = 6 – 12), ANOVA with Tukey HSD test (* p <0.05, ** p <0.01, *** p<0.001, **** p<0.0001).

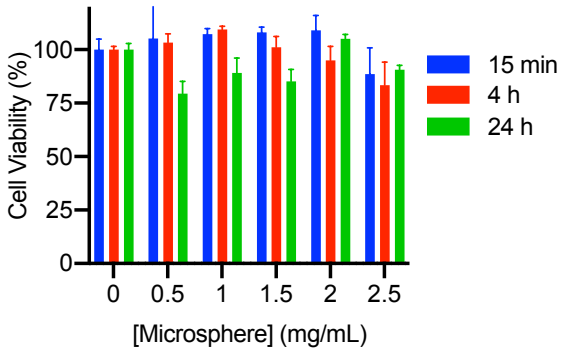

Figure 5.8 Cell viability after exposure to uncoated embolic microspheres. Mean are shown as mean ± SD (n = 2).

5.3.7 Time and dose-dependence of cell killing by combination of PAHM-coated microspheres and IRE

Due to the slower release of PAHM and the much smaller differences in cell viability between 4 h and 24 h exposure times, 100 µm microspheres were chosen over 71 µm ones to examine the ability of PAHM-coated microspheres to enhance IRE (Figure 5.9). Released PAHM did enhance the cell killing effect of IRE after 15 min and especially 4 h, but did not achieve significant enhancement after 24 h. For 15 min exposure, the viability of cells exposed to 912.5 V/cm decreased from 95% down to 40 – 54% when coated microspheres were added; however, there were no statistically significant

differences among the three microsphere doses (Figure 5.9A). The most substantial IRE enhancement was seen at 4 h exposure to PAHM-coated microspheres, as the viability of cells exposed to 562.5 V/cm was reduced from 86% to 65%, 56%, and 19% for 5 µg/mL, 15 µg/mL, and 25 µg/mL microsphere-coated PAHM (Figure 5.9B). This enhancement largely disappeared after 24 h exposure with the exception of combining 562.5 V/cm of IRE and 25 µg/mL of PAHM, which reduced cell viability to 75% from 91% by IRE alone (Figure 5.9C).

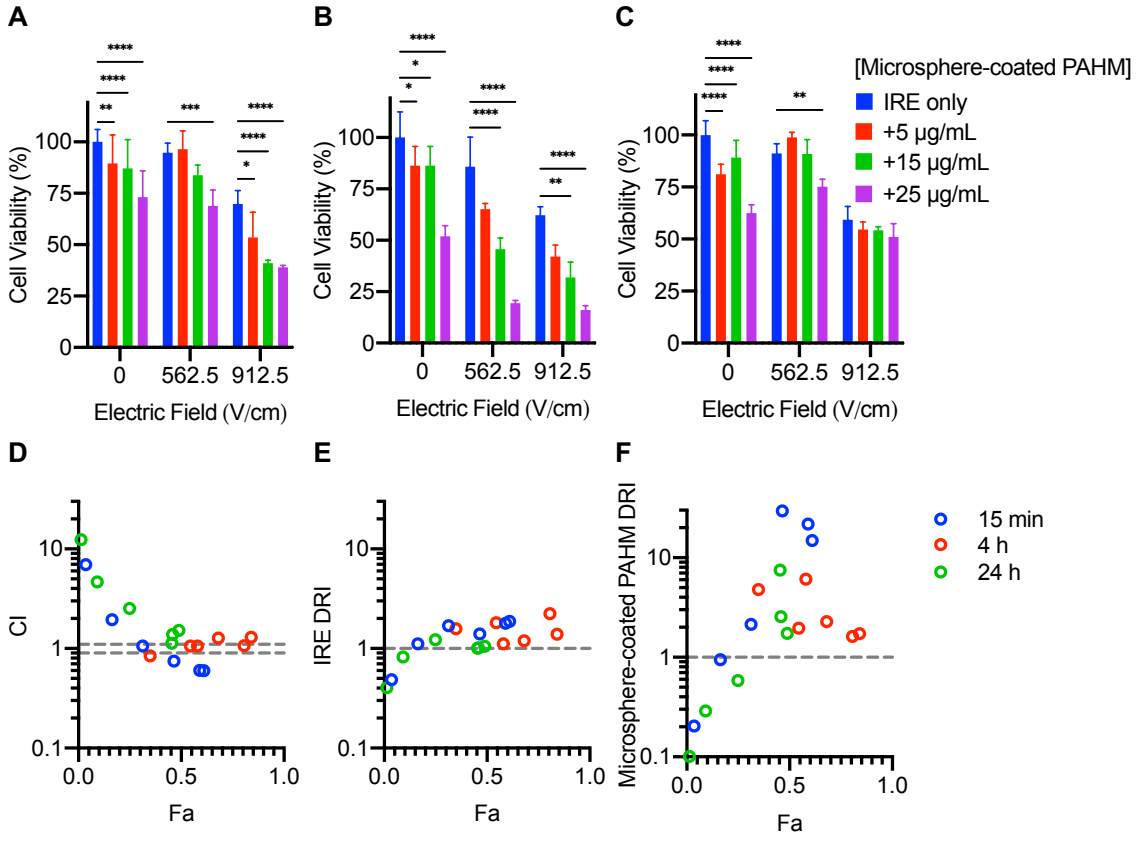

Figure 5.9 Cell viability after IRE treatment combined with exposure to PAHM released from coated embolic microspheres for (A) 15 min (B) 4 h (C) 24 h. Data are shown as mean ± SD (n = 3 – 9). ANOVA with Tukey HSD test (* p <0.05, ** p <0.01, *** p<0.001, **** p<0.0001). (D) Combination index analysis (CI <1, = 0.9 – 1 (dashed lines), >1 indicates synergism, nearly additive effect, and antagonism, respectively). Dose reduction index analysis for (E) IRE and (F) microsphere-coated PAHM (DRI <1, =1 (dashed line), >1 indicates unfavorable dose reduction, no dose reduction, and favorable dose reduction, respectively).

5.3.8 Dose reduction by combining PAHM-coated microspheres with IRE

Calculation of CI shows that combining IRE with exposure to PAHM-coated microspheres for 15 min is antagonistic at low Fa, but the combination becomes synergistic at intermediate Fa (Figure 5.9D). With 4 h exposure, most of the CI are within (or close to) the 0.9 – 1.1 range which indicates a nearly additive effect. All combinations with 24 h exposure displayed CI greater than 1.1. At low Fa the combinations are antagonistic but tend to become additive or synergistic at medium and high Fa. The DRI for IRE tend to increase with Fa and for Fa >0.1, the DRI for IRE is greater than 1 for all three exposure times (Figure 5.9E). The DRI for microsphere-coated PAHM also trends upward with Fa with values greater than 1 for Fa >0.2 (Figure 5.9F).

5.4 Discussion

One proposed mechanism to explain the physicochemical basis of electroporation is the nucleation theory, where a transmembrane potential can reduce the energy barrier for critical pore formation in the membrane. The probability of critical pore formation is related to membrane physical properties such as surface tension, edge line tension, and transmembrane voltage [146]. The application of pulsed electric fields during electroporation raises the transmembrane potential to overcome the energy barrier. Initially a hydrophobic pore forms in the membrane but if the pore radius exceeds a critical size (0.3 to 0.5 nm) it transitions into a hydrophilic one, allowing water to rush into the cell. Pore formation does not always induce cell death. When low electric field strengths are applied, as is the case during RE, cells are able to repair the cell membrane [47]. In contrast, when high electric field strengths are applied during IRE, cells are unable to repair the membrane and die due to various consequences, such as rupture from

osmotic stress, loss of critical organelles, or influx of cytotoxic molecules [46]. While IRE has been used to ablate tumors in a number of different organs, the tumor volume that can be treated is limited by the high electric field strength required to induce cancer cell death [58].

IRE will be much improved if the electric field threshold required to induce cell death can be lowered. One way to achieve this is by sensitizing the cell membrane to make it more susceptible to IRE [60]. SDS (a surfactant) and DMSO (a nonpolar protic solvent) can interact with membrane lipids to alter the membrane's edge line tension and surface tension, which inhibits the resealing of pores formed by electroporation, thereby enhancing the efficacy of IRE [46,58]. Cations can interact with the negatively charged cell membrane and enhance the transmembrane potential locally, lowering the electric field intensity required to induce cell death by IRE. A number of cations have also been shown to enhance IRE, including cationic anesthetics (such as procaine, tetracaine, and lidocaine [64,65]) and a cationic peptide (polyarginine) [66]. Drugs that indirectly alter the transmembrane potential have also been shown to enhance IRE [147,148].

In this study, we have shown that a synthetic membranolytic polymer, PAHM, can enhance the ability of IRE to kill human pancreatic cancer cells, and that combining IRE with PAHM reduces the doses of both IRE and PAHM needed for effecting cell killing (Figure 2 and 3). We speculate that the mechanism of PAHM sensitizing cell membranes to IRE resembles those of cations [64,66], surfactants and DMSO [58]. With cationic side chain, PAHM may electrostatically interact with anionic cell membrane to alter the transmembrane potential and make the membrane more susceptible to form pores at low electric field strengths [66]. Furthermore, the amphipathic properties of PAHM may

make it more difficult for the IRE-induced membrane pores to heal [58]. With the capacity of sensitizing tumor cells to low-field-strength IRE, increased volume of tumor ablation could potentially be achieved through combined use of PAHM and IRE.

The effect of cell killing by low doses (≤20 μg/mL) of PAHM (alone and in combination with IRE) is dependent on the duration of treatment. Unexpectedly, cell viability measured by the MTT assay was higher at 24 h than 4 h despite continued exposure to PAHM or combination with IRE (Figure 5.2B, Figure 5.3A-C). The MTT assay measures cellular metabolic activity as a proxy for cell viability [149]. If the cell membrane damage due to low doses of PAHM is not too extensive, the cells will be able to repair the membrane, which can take tens of minutes. During this time the cells may become temporarily less metabolically active [149]. The leaking of ATP from the damaged cell membrane can further reduce cell metabolism [150]. These phenomena may account for the apparent higher degree of cell death at 4 h. After 24 h, cells that survive PAHM treatment will have likely recovered full metabolic activity. Interestingly, such time-dependence of cell viability was not observed for IRE treatment alone (Figure 5.2A). The unique and disparate temporal dynamics of IRE and PAHM treatments can be exploited further (for example, continuous exposure of low-dose PAHM accompanied by multiple, properly timed pulses of IRE), in order to achieve even greater therapeutic benefit.

A potential limitation of PAHM is its nonspecific cytotoxicity. To avoid systemic dissemination, PAHM was coated onto embolic microspheres to allow for targeted delivery to a tumor. Embolization is an established cancer therapy, in which local blood vessels are deliberately occluded to starve a tumor of its blood supply [144]. Embolic

agents can be delivered simultaneously with chemotherapeutics via catheters in a process known as transcatheter arterial chemoembolization (TACE), currently under preclinical investigation [151–153]. Analogous to TACE, our PAHM-coated microspheres could also be delivered via catheter infusion to occlude tumor blood vessels and concentrate the PAHM within the tumor. The PAHM would slowly elute from the coated microspheres to accumulate locally within a tumor to sensitize the cancer cells to IRE and directly killing them. We chose to use PMMA microspheres over other types of embolic agents, such as liquids or metallic coils [144], because conductive materials have been shown to distort the ablation zone during IRE [154]. PMMA microspheres can be produced with consistent and well-defined diameters, allowing them to embolize deep, distal microvasculature of the tumors [155]. Therefore, we envision a "triple threat" strategy, where tumors can be attacked by embolic microspheres, which also release cytotoxic PAHM, which kills tumor cells either directly or through sensitization of IRE. The mutual enhancement among different therapeutic modalities and the in vivo antitumor efficacy of this strategy will be the subject of future investigation.

We developed a simple, effective method of coating PAHM onto PMMA microspheres by controlling the rate of solvent evaporation [156,157] (Figure 5.4). When submerged in cell culture medium, PAHM releases from coated microspheres over the course of 1 week (Figure 5.5). PAHM releases slightly faster from 71 μm microspheres than 100 μm microspheres, presumably due to the greater surface area of the smaller particles. An initial burst release of approximately 70% of the total PAHM is seen over the first day, followed by a more sustained release in the next 6 days. This release profile could be attractive in vivo, where a high dose of PAHM is initially delivered for effective

tumor cell killing followed by sustained release to sensitize any surviving cells for destruction by IRE.

Microspheres coated with PAHM were capable of killing tumor cells, although the effect was less prominent than free PAHM at equivalent doses (Figure 5.7). This is expected because the sustained release profile dictates that only a fraction of PAHM was released from the microspheres at any given time (Figure 5.5). Similarly, the higher percentage of cell killing by 71 μm microspheres at 4 h compared with 100 μm microspheres can be explained by the higher amount of PAHM released from the smaller size microspheres over the course of 4 h. Despite the low-level gradual release of PAHM from microspheres, significant enhancement of the efficacy of IRE was observed at 15-min and 4-h time points (Figure 5.9A,B). Judging by the CI values, the nature of the enhancement is either synergistic or additive over a wide range of cell death rates (Fa = 0.3 ~ 1) (Figure 5.9D). More importantly, the DRI for nearly all treatment combinations are greater than 1 (Figure 5.9E,F). This suggests that lower doses of IRE/PAHM in combination have the same potency of killing cells as higher doses of the two modalities used separately. Dose reduction of IRE and/or PAHM may translate into clinical benefits including less toxic side effects, less cost and higher patient compliance.

Some have argued that the chemical sensitizers for IRE should not be inherently cytotoxic [58,66]. However, due to the stochastic nature of IRE, even high electric fields do not guarantee complete cell death. Local electrical heterogeneity within the tumor tissue can leave patches of live cells within the ablation zone. These live patches are unique to IRE ablation and often lead to tumor recurrence [46,59]. By using a cytotoxic

sensitizer, PAHM, there is the possibility of eliminating these live patches for a more robust tumor ablation.

Certain IRE-related parameters, such as the number, duration, and frequency of pulses, can be optimized to improve the efficacy of IRE [46]; however, all IRE protocols would benefit from lowering the electric field threshold in the tumor tissue. IRE has also been shown to release tumor antigens [52,158–160], which can be damaged by high electric field strengths [161]. Using PAHM to lower the electric field strength used during IRE, it may be possible to preserve a greater percentage of tumor antigens in their native form and generate a more robust antitumor immune response.

Taken together, our results suggest that a synthetic membranolytic polymer, PAHM, can be coated onto and released from embolic microspheres to reduce the electric field strength required for killing human pancreatic cancer cells by IRE. Future studies will focus on elucidating the mechanism of PAHM-modulated sensitization of cells to IRE. The timing, frequency, and duration of the treatment combinations could be optimized to achieve better cell killing. Efficacy of the combination therapy will need to be validated in appropriate in vivo tumor models.

5.5 Conclusions

We have demonstrated that a synthetic membranolytic polymer, PAHM, when combined with IRE, led to enhanced killing of human pancreatic cancer cells. We have further developed a simple process of coating PAHM onto embolic microspheres, which provided for sustained release of PAHM. Nearly all tested combinations of PAHM and IRE caused cancer cell death in a dose-sparing manner, and some combinations achieved

cell killing synergistically. These findings established that sustained release of PAHM from embolic microspheres have the potential to improve IRE-mediated tumor ablation.

Chapter 6 Conclusions and Future Directions

6.1 Improving the Mucoadhesive Wafer Formulation

Varying the ratio between CMC and ALG resulted in wafers with different microstructure, mechanical properties, disintegration time, and release kinetics of model compounds. Wafers with high CMC content were highly mucoadhesive to sublingual mucosal tissue and could withstand extensive washing, leading to improved protein permeation into the tissue. On the other hand, wafers with high ALG content were not only mechanically robust, but also able to protect a model enzyme (β-galactosidase) against lyophilization and heat challenge. HIV gp140 protein loaded in wafers of the optimal composition could be stored and transported without cold chain, while maintaining antigen-specific immunogenicity after sublingual vaccination in mice. These findings established that the CMC/ALG binary blend polymer wafers have the potential to improve the sublingual delivery and storage stability of protein-based vaccines.

Although the current CMC/ALG binary blend has shown desirable properties, the wafer formulation could be improved. While wafers maintained the immunogenicity of the protein vaccine for ~2 weeks without cold chain storage, the long-term storage stability has not yet been investigated. To further enhance the preservation of the protein vaccines, additional stabilizers can be added to the wafer formulations. A number of chemicals have a history of use as protein-stabilizing compounds, including polyols (e.g., glycerol, mannitol, sorbitol), sugars (e.g., sucrose and trehalose), and amino acids (e.g., glycine, proline) [82]. One, or more, of these stabilizing compounds could be added to the wafer formulation to protect that protein vaccines.

Another opportunity for improvement is the co-encapsulation and controlled release of both antigen and immunostimulatory adjuvant using the same wafer formulation. For the sublingual immunization of mice with the current CMC/ALG binary blend, the adjuvant (αGalCer) had to be delivered separately in liquid solution. While αGalCer is soluble in DMSO, it is not soluble in water. While the current formulation method cannot load poorly soluble cargo into the wafers, αGalCer could be first encapsulated in amphiphilic liquid polymer nano-droplets and then loaded into the wafers. Our lab has previously designed a biodegradable amphiphilic liquid polymer composed of multiple short blocks of polyethylene glycol (PEG) and polycaprolactone (PCL) connected through acid-labile acetal linkages. This polymer forms self-emulsifying nano-droplets in water for delivering poorly soluble drugs [162]. Preliminary results have shown that these nano-droplets can be incorporated into the CMC/ALG binary blend polymer wafers. In addition to αGalCer, these nano-droplet loaded wafers are a promising material system for the encapsulation and delivery of other poorly soluble cargos to the sublingual mucosal.

6.2 PVA Wafers for Sublingual Delivery and Stabilization of DNA Vaccines

Polymer wafers were also effective delivery systems of PEI/DNA polyplexes for nonviral gene delivery. While wafers composed of CMC and ALG were ineffective polyplex carriers, due to their anionic charges disrupting the polyplex attraction to cell membranes, wafers composed of PVA greatly enhanced the in vitro transfection efficiency of polyplex-mediated gene delivery in 10% serum containing medium. The physical form of the PVA wafers was crucial for this enhancement. Like CMC, PVA also has mucoadhesive properties and has been used as an excipient for oral mucosal drug

delivery [84]. The polyplex-loaded PVA wafers may exceptionally suited for sublingual delivery of DNA vaccines. Sublingual delivery of PEI/DNA polyplexes, followed by a mucosal protein boost, have been shown to generate antigen-specific antibodies [163]. However, similar to protein vaccines, polyplexes are subject to saliva washout. Mucoadhesive PVA wafers could enhance permeation into the sublingual tissue and transfection efficiency of DNA vaccines.

In addition to poor transfection efficiency in the presence of serum, poor storage stability of polyplexes limits their clinical practicability. Due to the tendency of polyplexes to aggregate in solution, freshly prepared formulations are required prior to administration [164]. While PEI/DNA polyplexes have been previously lyophilized, this is often associated with loss of activity [37]. Our PVA wafers may be able to stabilize the polyplexes during lyophilization and storage. Currently, polyplex-loaded PVA wafers are used to transfect NIH/3T3 cells within 1 day of preparation. However, preliminary results indicate that even after storage for 2 weeks at room temperature without desiccation, the polyplex-loaded PVA wafers could still transfect cells. Although the mechanisms of polyplex stabilization are not fully understood [164], the PVA wafers may be able to stabilize polyplexes similar to the CMC/ALG wafer protection of protein vaccines.

6.3 Optimizing Anticancer Therapy Combinations and Potential Immunological Implications

The membranolytic synthetic polymer, PAHM, displayed high levels of cytotoxicity to multiple cancer cell cells. In addition, PAHM enhanced the cytotoxicity of other cancer therapies. The membrane disruption by PAHM led to increased cellular uptake of DOX. When used in combination, PAHM and DOX killed cancer cells synergistically.

This synergy allowed far lower DOX doses to be used for to kill cancer cells, which could potentially minimize negative side effects. We also demonstrated that PAHM enhances the cytotoxicity of IRE. The combination of PAHM and IRE allowed the use of lower electric field strengths to kill cancer cells, which could potentially improve IRE-mediated tumor ablation. PAHM was also coated onto embolic microspheres to provide for sustained release and targeted tumor delivery. While nearly all tested combinations of PAHM and DOX or PAHM and IRE killed cancer cells in a dose-sparing manner, treatment combinations could be optimized to achieve better cell killing. Like PAHM, IRE-induced membrane disruption could lead to increased cellular uptake of DOX. In addition, DOX could be loaded into an embolic carrier for target tumor delivery. How the hypoxia due to embolization effects the cytotoxicity of the treatment combinations is also yet to be explored.

In addition to the immediate cytotoxicity, the ability of these treatment combinations to induce an anticancer immune response is another point of interest. IRE has been shown to release tumor antigens capable of stimulating an antitumor immunity. However, the use of adjuvant immunostimulants is often necessary to generate a robust immune response [52]. One explanation is IRE-induced cell death may not release sufficient damage-associated molecular patterns (DAMPs), danger signals that induce the maturation of dendritic cells that mediate anticancer immunity [165]. We have previously shown that cancer cells treated with PAHM release ATP and HMGB1, two such DAMPs [166]. PAHM-mediated membrane lysis is also expected to release tumor antigens. Thus, the combination of PAHM and IRE (or DOX) could not only effectively kill cancer cells

but could also release sufficient tumor antigens and DAMPs to induce a prolonged antitumor immunity.

Bibliography

[1] W.B. Liechty, D.R. Kryscio, B. V. Slaughter, N.A. Peppas, Polymers for Drug Delivery Systems, Annu. Rev. Chem. Biomol. Eng. 1 (2010) 149–173. https://doi.org/10.1146/annurev-chembioeng-073009-100847.

[2] A. Tabet, C. Wang, Gels without Vapor Pressure: Soft, Nonaqueous, and Solvent-Free Supramolecular Biomaterials for Prospective Parenteral Drug Delivery Applications, Adv. Healthc. Mater. 8 (2019) 1800908. https://doi.org/10.1002/adhm.201800908.

[3] J. Li, D.J. Mooney, Designing hydrogels for controlled drug delivery, Nat. Rev. Mater. 1 (2016) 16071. https://doi.org/10.1038/natrevmats.2016.71.

[4] N. Nishiyama, K. Kataoka, Current state, achievements, and future prospects of polymeric micelles as nanocarriers for drug and gene delivery, Pharmacol. Ther. 112 (2006) 630–648. https://doi.org/10.1016/j.pharmthera.2006.05.006.

[5] O. Pillai, R. Panchagnula, Polymers in drug delivery, Curr. Opin. Chem. Biol. (2001). https://doi.org/10.1016/S1367-5931(00)00227-1.

[6] R.F. Donnelly, A.D. Woolfson, Bioadhesive drug delivery systems, CRC Press, 2013. https://doi.org/10.1201/b13758.

[7] R. Duncan, Polymer conjugates as anticancer nanomedicines, Nat. Rev. Cancer. 6 (2006) 688–701. https://doi.org/10.1038/nrc1958.

[8] J.M. Harris, R.B. Chess, Effect of pegylation on pharmaceuticals, Nat. Rev. Drug Discov. 2 (2003) 214–221. https://doi.org/10.1038/nrd1033.

[9] A.H. Faraji, P. Wipf, Nanoparticles in cellular drug delivery, Bioorg. Med. Chem. 17 (2009) 2950–2962. https://doi.org/10.1016/j.bmc.2009.02.043.

[10] M. Murakami, H. Cabral, Y. Matsumoto, S. Wu, M.R. Kano, T. Yamori, N. Nishiyama, K. Kataoka, Improving Drug Potency and Efficacy by Nanocarrier-Mediated Subcellular Targeting, Sci. Transl. Med. 3 (2011) 64ra2-64ra2. https://doi.org/10.1126/scitranslmed.3001385.

[11] J. Tan, J. Tay, J. Hedrick, Y.Y. Yang, Synthetic macromolecules as therapeutics that overcome resistance in cancer and microbial infection, Biomaterials. 252 (2020) 120078. https://doi.org/10.1016/j.biomaterials.2020.120078.

[12] H. Kraan, H. Vrieling, C. Czerkinsky, W. Jiskoot, G. Kersten, J.-P. Amorij, Buccal and sublingual vaccine delivery, J. Control. Release. 190 (2014) 580–92. https://doi.org/10.1016/j.jconrel.2014.05.060.

[13] J. Holmgren, C. Czerkinsky, Mucosal immunity and vaccines., Nat. Med. 11 (2005) S45-53. https://doi.org/10.1038/nm1213.

[14] P. Brandtzaeg, Mucosal immunity: induction, dissemination, and effector functions, Scand. J. Immunol. 70 (2009) 505–15. https://doi.org/10.1111/j.1365-3083.2009.02319.x.

[15] S. Singh, G. Yang, S.N. Byrareddy, M.A. Barry, K.J. Sastry, Natural killer T cell and TLR9 agonists as mucosal adjuvants for sublingual vaccination with clade C HIV-1 envelope protein, Vaccine. 32 (2014) 6934–6940. https://doi.org/10.1016/j.vaccine.2014.10.051.

[16] J. Wang, T. Murakami, S. Yoshida, H. Matsuoka, A. Ishii, T. Tanaka, K. Tobita, M. Ohtsuki, H. Nakagawa, M. Kusama, E. Kobayashi, Predominant cell-mediated

immunity in the oral mucosa: gene gun-based vaccination against infectious diseases., J. Dermatol. Sci. 31 (2003) 203–10. https://doi.org/10.1016/s0923-1811(03)00027-6.
[17] J.H. Choi, S.C. Schafer, L. Zhang, G.P. Kobinger, T. Juelich, A.N. Freiberg, M.A. Croyle, A Single Sublingual Dose of an Adenovirus-Based Vaccine Protects against Lethal Ebola Challenge in Mice and Guinea Pigs, Mol. Pharm. 9 (2012) 156–167. https://doi.org/10.1021/mp200392g.
[18] P. Xiao, L.J. Patterson, S. Kuate, E. Brocca-Cofano, M.A. Thomas, D. Venzon, J. Zhao, J. DiPasquale, C. Fenizia, E.M. Lee, I. Kalisz, V.S. Kalyanaraman, R. Pal, D. Montefiori, B.F. Keele, M. Robert-Guroff, Replicating Adenovirus-Simian Immunodeficiency Virus (SIV) Recombinant Priming and Envelope Protein Boosting Elicits Localized, Mucosal IgA Immunity in Rhesus Macaques Correlated with Delayed Acquisition following a Repeated Low-Dose Rectal SIV mac251 Cha, J. Virol. 86 (2012) 4644–4657. https://doi.org/10.1128/JVI.06812-11.
[19] Z. Cui, R.J. Mumper, Bilayer films for mucosal (genetic) immunization via the buccal route in rabbits, Pharm. Res. 19 (2002) 947–53. https://doi.org/10.1023/a:1016454003450.
[20] H. Zhang, J. Zhang, J.B. Streisand, Oral Mucosal Drug Delivery, Clin. Pharmacokinet. 41 (2002) 661–680. https://doi.org/10.2165/00003088-200241090-00003.
[21] J.S. Boateng, J.C. Mitchell, H. Pawar, I. Ayensu, Functional characterisation and permeation studies of lyophilised thiolated chitosan xerogels for buccal delivery of insulin, Protein Pept. Lett. 21 (2014) 1163–75. https://doi.org/10.2174/09298665216661408051244O3.
[22] H.S. Oberoi, Y.M. Yorgensen, A. Morasse, J.T. Evans, D.J. Burkhart, PEG modified liposomes containing CRX-601 adjuvant in combination with methylglycol chitosan enhance the murine sublingual immune response to influenza vaccination, J. Control. Release. 223 (2016) 64–74. https://doi.org/10.1016/j.jconrel.2015.11.006.
[23] A. Borde, A. Ekman, J. Holmgren, A. Larsson, Effect of protein release rates from tablet formulations on the immune response after sublingual immunization., Eur. J. Pharm. Sci. 47 (2012) 695–700. https://doi.org/10.1016/j.ejps.2012.08.014.
[24] J.G. Edmans, C. Murdoch, M.E. Santocildes-Romero, P. V. Hatton, H.E. Colley, S.G. Spain, Incorporation of lysozyme into a mucoadhesive electrospun patch for rapid protein delivery to the oral mucosa, Mater. Sci. Eng. C. Mater. Biol. Appl. 112 (2020) 110917. https://doi.org/10.1016/j.msec.2020.110917.
[25] N.H. Patil, P. V. Devarajan, Insulin-loaded alginic acid nanoparticles for sublingual delivery, Drug Deliv. 23 (2016) 429–36. https://doi.org/10.3109/10717544.2014.916769.
[26] A. Borde, A. Larsson, J. Holmgren, E. Nygren, Preparation and evaluation of a freeze-dried oral killed cholera vaccine formulation., Eur. J. Pharm. Biopharm. 79 (2011) 508–18. https://doi.org/10.1016/j.ejpb.2011.06.009.
[27] S. Murugappan, H.P. Patil, H.W. Frijlink, A. Huckriede, W.L.J. Hinrichs, Simplifying influenza vaccination during pandemics: sublingual priming and intramuscular boosting of immune responses with heterologous whole inactivated

influenza vaccine, AAPS J. 16 (2014) 342–9. https://doi.org/10.1208/s12248-014-9565-z.
[28] V. Busignies, G. Simon, G. Mollereau, O. Bourry, V. Mazel, M. Rosa-Calatrava, P. Tchoreloff, Development and pre-clinical evaluation in the swine model of a mucosal vaccine tablet for human influenza viruses: A proof-of-concept study, Int. J. Pharm. 538 (2018) 87–96. https://doi.org/10.1016/j.ijpharm.2018.01.021.
[29] C.H. Jones, C.-K. Chen, A. Ravikrishnan, S. Rane, B.A. Pfeifer, Overcoming Nonviral Gene Delivery Barriers: Perspective and Future, Mol. Pharm. 10 (2013) 4082–4098. https://doi.org/10.1021/mp400467x.
[30] C.M. Wiethoff, C.R. Middaugh, Barriers to Nonviral Gene Delivery, J. Pharm. Sci. 92 (2003) 203–217. https://doi.org/10.1002/jps.10286.
[31] L. Vannucci, M. Lai, F. Chiuppesi, L. Ceccherini-Nelli, M. Pistello, Viral vectors: a look back and ahead on gene transfer technology., New Microbiol. 36 (2013) 1–22. http://www.ncbi.nlm.nih.gov/pubmed/23435812.
[32] T. Kimura, Y. Nibe, S. Funamoto, M. Okada, T. Furuzono, T. Ono, H. Yoshizawa, T. Fujisato, K. Nam, A. Kishida, Preparation of a Nanoscaled Poly(vinyl alcohol)/Hydroxyapatite/DNA Complex Using High Hydrostatic Pressure Technology for In Vitro and In Vivo Gene Delivery, J. Drug Deliv. 2011 (2011) 1–8. https://doi.org/10.1155/2011/962743.
[33] U. Lungwitz, M. Breunig, T. Blunk, A. Göpferich, Polyethylenimine-based non-viral gene delivery systems, Eur. J. Pharm. Biopharm. 60 (2005) 247–266. https://doi.org/10.1016/j.ejpb.2004.11.011.
[34] R.S. Burke, S.H. Pun, Extracellular barriers to in Vivo PEI and PEGylated PEI polyplex-mediated gene delivery to the liver., Bioconjug. Chem. 19 (2008) 693–704. https://doi.org/10.1021/bc700388u.
[35] R. Goyal, S.K. Tripathi, E. Vazquez, P. Kumar, K.C. Gupta, Biodegradable poly(vinyl alcohol)-polyethylenimine nanocomposites for enhanced gene expression in vitro and in vivo., Biomacromolecules. 13 (2012) 73–83. https://doi.org/10.1021/bm201157f.
[36] L.W. Warriner, J.R. Duke, D.W. Pack, J.E. DeRouchey, Succinylated Polyethylenimine Derivatives Greatly Enhance Polyplex Serum Stability and Gene Delivery In Vitro, Biomacromolecules. 19 (2018) 4348–4357. https://doi.org/10.1021/acs.biomac.8b01248.
[37] J. Schulze, S. Hendrikx, M. Schulz-Siegmund, A. Aigner, Microparticulate poly(vinyl alcohol) hydrogel formulations for embedding and controlled release of polyethylenimine (PEI)-based nanoparticles, Acta Biomater. 45 (2016) 210–222. https://doi.org/10.1016/j.actbio.2016.08.056.
[38] J. Schulze, S. Kuhn, S. Hendrikx, M. Schulz-Siegmund, T. Polte, A. Aigner, Spray-Dried Nanoparticle-in-Microparticle Delivery Systems (NiMDS) for Gene Delivery, Comprising Polyethylenimine (PEI)-Based Nanoparticles in a Poly(Vinyl Alcohol) Matrix, Small. 14 (2018) 1701810. https://doi.org/10.1002/smll.201701810.
[39] S. Rivankar, An overview of doxorubicin formulations in cancer therapy, J. Cancer Res. Ther. 10 (2014) 853–8. https://doi.org/10.4103/0973-1482.139267.
[40] N.H. Park, W. Cheng, F. Lai, C. Yang, P. Florez de Sessions, B. Periaswamy, C. Wenhan Chu, S. Bianco, S. Liu, S. Venkataraman, Q. Chen, Y.Y. Yang, J.L.

Hedrick, Addressing Drug Resistance in Cancer with Macromolecular Chemotherapeutic Agents, J. Am. Chem. Soc. 140 (2018) 4244–4252. https://doi.org/10.1021/jacs.7b11468.
[41] H. Zahreddine, K.L.B. Borden, Mechanisms and insights into drug resistance in cancer, Front. Pharmacol. (2013). https://doi.org/10.3389/fphar.2013.00028.
[42] X. Huang, J. Cao, Y. Zhang, T. Liu, H. Yan, Polyethylenimine modified with 2,3-dimethylmaleic anhydride potentiates the antitumor efficacy of conventional chemotherapy, Mater. Sci. Eng. C. Mater. Biol. Appl. 102 (2019) 558–568. https://doi.org/10.1016/j.msec.2019.04.081.
[43] L. Nyström, M. Malmsten, Membrane interactions and cell selectivity of amphiphilic anticancer peptides, Curr. Opin. Colloid Interface Sci. 38 (2018) 1–17. https://doi.org/10.1016/j.cocis.2018.06.009.
[44] A. Gabizon, R. Catane, B. Uziely, B. Kaufman, T. Safra, R. Cohen, F. Martin, A. Huang, Y. Barenholz, Prolonged circulation time and enhanced accumulation in malignant exudates of doxorubicin encapsulated in polyethylene-glycol coated liposomes., Cancer Res. 54 (1994) 987–92. http://www.ncbi.nlm.nih.gov/pubmed/8313389.
[45] J.G. Piao, F. Gao, L. Yang, Acid-Responsive Therapeutic Polymer for Prolonging Nanoparticle Circulation Lifetime and Destroying Drug-Resistant Tumors, ACS Appl. Mater. Interfaces. (2016). https://doi.org/10.1021/acsami.5b10550.
[46] C. Jiang, R. V. Davalos, J.C. Bischof, A review of basic to clinical studies of irreversible electroporation therapy, IEEE Trans. Biomed. Eng. 62 (2015) 4–20. https://doi.org/10.1109/TBME.2014.2367543.
[47] A.R. Deipolyi, A. Golberg, M.L. Yarmush, R.S. Arellano, R. Oklu, Irreversible electroporation: evolution of a laboratory technique in interventional oncology, Diagn. Interv. Radiol. 20 (2014) 147–54. https://doi.org/10.5152/dir.2013.13304.
[48] R. Lencioni, D. Cioni, C. Della Pina, L. Crocetti, Hepatocellular carcinoma: new options for image-guided ablation, J. Hepatobiliary. Pancreat. Sci. 17 (2010) 399–403. https://doi.org/10.1007/s00534-009-0233-0.
[49] P. Wagstaff, M. Buijs, W. van den Bos, D. de Bruin, P. Zondervan, J. de la Rosette, P. Laguna, Irreversible electroporation: state of the art, Onco. Targets. Ther. (2016) 2437. https://doi.org/10.2147/OTT.S88086.
[50] M. Bower, L. Sherwood, Y. Li, R. Martin, Irreversible electroporation of the pancreas: Definitive local therapy without systemic effects, J. Surg. Oncol. (2011). https://doi.org/10.1002/jso.21899.
[51] R.C.G. Martin, Irreversible electroporation of locally advanced pancreatic head adenocarcinoma, J. Gastrointest. Surg. 17 (2013) 1850–6. https://doi.org/10.1007/s11605-013-2309-z.
[52] R.E. Neal, J.H. Rossmeisl, J.L. Robertson, C.B. Arena, E.M. Davis, R.N. Singh, J. Stallings, R. V. Davalos, Improved local and systemic anti-tumor efficacy for irreversible electroporation in immunocompetent versus immunodeficient mice, PLoS One. 8 (2013) e64559. https://doi.org/10.1371/journal.pone.0064559.
[53] G. Onik, B. Rubinsky, Irreversible Electroporation: First Patient Experience Focal Therapy of Prostate Cancer, in: 2010. https://doi.org/10.1007/978-3-642-05420-4_10.
[54] H.J. Scheffer, K. Nielsen, M.C. de Jong, A.A.J.M. van Tilborg, J.M. Vieveen,

A.R.A. Bouwman, S. Meijer, C. van Kuijk, P.M.P. van den Tol, M.R. Meijerink, Irreversible electroporation for nonthermal tumor ablation in the clinical setting: a systematic review of safety and efficacy., J. Vasc. Interv. Radiol. 25 (2014) 997–1011; quiz 1011. https://doi.org/10.1016/j.jvir.2014.01.028.

[55] K.R. Thomson, W. Cheung, S.J. Ellis, D. Federman, H. Kavnoudias, D. Loader-Oliver, S. Roberts, P. Evans, C. Ball, A. Haydon, Investigation of the Safety of Irreversible Electroporation in Humans, J. Vasc. Interv. Radiol. 22 (2011) 611–621. https://doi.org/10.1016/j.jvir.2010.12.014.

[56] K.R. Thomson, H. Kavnoudias, R.E. Neal, Introduction to Irreversible Electroporation—Principles and Techniques, Tech. Vasc. Interv. Radiol. 18 (2015) 128–134. https://doi.org/10.1053/j.tvir.2015.06.002.

[57] C. Niessen, S. Thumann, L. Beyer, B. Pregler, J. Kramer, S. Lang, A. Teufel, E.M. Jung, C. Stroszczynski, P. Wiggermann, Percutaneous Irreversible Electroporation: Long-term survival analysis of 71 patients with inoperable malignant hepatic tumors, Sci. Rep. 7 (2017) 43687. https://doi.org/10.1038/srep43687.

[58] C. Jiang, Z. Qin, J. Bischof, Membrane-targeting approaches for enhanced cancer cell destruction with irreversible electroporation, Ann. Biomed. Eng. 42 (2014) 193–204. https://doi.org/10.1007/s10439-013-0882-7.

[59] Z. Qin, J. Jiang, G. Long, B. Lindgren, J.C. Bischof, Irreversible electroporation: An in vivo study with dorsal skin fold chamber, Ann. Biomed. Eng. (2013). https://doi.org/10.1007/s10439-012-0686-1.

[60] Y. Chen, M.A.J. Moser, Y. Luo, W. Zhang, B. Zhang, Chemical Enhancement of Irreversible Electroporation: A Review and Future Suggestions, Technol. Cancer Res. Treat. 18 (2019) 1533033819874128. https://doi.org/10.1177/1533033819874128.

[61] R.C. Lee, Physical mechanisms of tissue injury in electrical trauma, IEEE Trans. Educ. 34 (1991) 223–230. https://doi.org/10.1109/13.85080.

[62] V. V. Fedorov, V.P. Nikolski, I.R. Efimov, Effect of Electroporation on Cardiac Electrophysiology, in: Methods Mol. Biol., 2008: pp. 433–448. https://doi.org/10.1007/978-1-59745-194-9_34.

[63] M. Faroja, M. Ahmed, L. Appelbaum, E. Ben-David, M. Moussa, J. Sosna, I. Nissenbaum, S.N. Goldberg, Irreversible Electroporation Ablation: Is All the Damage Nonthermal?, Radiology. 266 (2013) 462–470. https://doi.org/10.1148/radiol.12120609.

[64] M. Grys, Z. Madeja, W. Korohoda, Decreasing the thresholds for electroporation by sensitizing cells with local cationic anesthetics and substances that decrease the surface negative electric charge, Cell. Mol. Biol. Lett. 19 (2014) 65–76. https://doi.org/10.2478/s11658-013-0114-z.

[65] F. Pan, D.F. Vollherbst, T. Do, D.A. Ridder, P.L. Pereira, H.U. Kauczor, S. Macher-Göppinger, C.M. Sommer, Intra-arterial Injection of Lidocaine as a Cell Sensitizer during Irreversible Electroporation, J. Vasc. Interv. Radiol. 31 (2020) 831-839.e2. https://doi.org/10.1016/j.jvir.2019.09.029.

[66] S.M. Kennedy, E.J. Aiken, K.A. Beres, A.R. Hahn, S.J. Kamin, S.C. Hagness, J.H. Booske, W.L. Murphy, Cationic peptide exposure enhances pulsed-electric-field-mediated membrane disruption., PLoS One. 9 (2014) e92528. https://doi.org/10.1371/journal.pone.0092528.

[67] J.O. Morales, J.T. McConville, Novel strategies for the buccal delivery of macromolecules, Drug Dev. Ind. Pharm. 40 (2014) 579–90. https://doi.org/10.3109/03639045.2014.892960.
[68] B.-S. Shim, Y. Choi, I.S. Cheon, M.K. Song, Sublingual delivery of vaccines for the induction of mucosal immunity., Immune Netw. 13 (2013) 81–5. https://doi.org/10.4110/in.2013.13.3.81.
[69] D.I. Bernstein, M.F. Pasetti, R. Brady, A.D. Buskirk, R. Wahid, M. Dickey, M. Cohen, H. Baughman, J. El-Khorazaty, N. Maier, M.B. Sztein, S. Baqar, A.L. Bourgeois, A Phase 1 dose escalating study of double mutant heat-labile toxin LTR192G/L211A (dmLT) from Enterotoxigenic Escherichia coli (ETEC) by sublingual or oral immunization, Vaccine. 37 (2019) 602–611. https://doi.org/10.1016/j.vaccine.2018.12.011.
[70] V.F. Patel, F. Liu, M.B. Brown, Advances in oral transmucosal drug delivery, J. Control. Release. 153 (2011) 106–16. https://doi.org/10.1016/j.jconrel.2011.01.027.
[71] M. Montenegro-Nicolini, J.O. Morales, Overview and Future Potential of Buccal Mucoadhesive Films as Drug Delivery Systems for Biologics, AAPS PharmSciTech. (2017). https://doi.org/10.1208/s12249-016-0525-z.
[72] T. Caon, L. Jin, C.M.O. Simões, R.S. Norton, J.A. Nicolazzo, Enhancing the buccal mucosal delivery of peptide and protein therapeutics, Pharm. Res. 32 (2015) 1–21. https://doi.org/10.1007/s11095-014-1485-1.
[73] F. Cui, C. He, M. He, C. Tang, L. Yin, F. Qian, C. Yin, Preparation and evaluation of chitosan-ethylenediaminetetraacetic acid hydrogel films for the mucoadhesive transbuccal delivery of insulin., J. Biomed. Mater. Res. A. 89 (2009) 1063–71. https://doi.org/10.1002/jbm.a.32071.
[74] C. Colonna, I. Genta, P. Perugini, F. Pavanetto, T. Modena, M. Valli, C. Muzzarelli, B. Conti, 5-methyl-pyrrolidinone chitosan films as carriers for buccal administration of proteins, AAPS PharmSciTech. 7 (2006) 70. https://doi.org/10.1208/pt70370.
[75] I. Ayensu, J. Boateng, Development and Evaluation of Lyophilized Thiolated-Chitosan Wafers for Buccal Delivery of Protein, J. Sci. Technol. 32 (2012) 46–55. https://doi.org/10.4314/just.v32i2.7.
[76] I. Ayensu, J.C. Mitchell, J.S. Boateng, In vitro characterisation of chitosan based xerogels for potential buccal delivery of proteins, Carbohydr. Polym. 89 (2012) 935–941. https://doi.org/10.1016/j.carbpol.2012.04.039.
[77] I. Ayensu, J.C. Mitchell, J.S. Boateng, Development and physico-mechanical characterisation of lyophilised chitosan wafers as potential protein drug delivery systems via the buccal mucosa, Colloids Surf. B. Biointerfaces. 91 (2012) 258–65. https://doi.org/10.1016/j.colsurfb.2011.11.004.
[78] I. Ayensu, J.C. Mitchell, J.S. Boateng, Effect of membrane dialysis on characteristics of lyophilised chitosan wafers for potential buccal delivery of proteins, Int. J. Biol. Macromol. 50 (2012) 905–9. https://doi.org/10.1016/j.ijbiomac.2012.02.014.
[79] J.S. Boateng, I. Ayensu, Preparation and characterization of laminated thiolated chitosan-based freeze-dried wafers for potential buccal delivery of macromolecules, Drug Dev. Ind. Pharm. 40 (2014) 611–8.

https://doi.org/10.3109/03639045.2014.884126.
[80] D. Chen, D. Kristensen, Opportunities and challenges of developing thermostable vaccines, Expert Rev. Vaccines. 8 (2009) 547–57. https://doi.org/10.1586/erv.09.20.
[81] O.S. Kumru, S.B. Joshi, D.E. Smith, C.R. Middaugh, T. Prusik, D.B. Volkin, Vaccine instability in the cold chain: mechanisms, analysis and formulation strategies, Biologicals. 42 (2014) 237–59. https://doi.org/10.1016/j.biologicals.2014.05.007.
[82] S. Ohtake, Y. Kita, T. Arakawa, Interactions of formulation excipients with proteins in solution and in the dried state, Adv. Drug Deliv. Rev. 63 (2011) 1053–73. https://doi.org/10.1016/j.addr.2011.06.011.
[83] L.J.J. Hansen, R. Daoussi, C. Vervaet, J.-P. Remon, T.R.M. De Beer, Freeze-drying of live virus vaccines: A review, Vaccine. 33 (2015) 5507–5519. https://doi.org/10.1016/j.vaccine.2015.08.085.
[84] G. Sandri, S. Rossi, F. Ferrari, M.C. Bonferoni, C.M. Caramella, Mucoadhesive Polymers as Enabling Excipients for Oral Mucosal Drug Delivery, in: M.J. Rathbone, S. Şenel, I. Pather (Eds.), Oral Mucosal Drug Deliv. Ther., Springer, Boston, MA, 2015: pp. 53–88.
[85] W. Wang, Lyophilization and development of solid protein pharmaceuticals, Int. J. Pharm. 203 (2000) 1–60. https://doi.org/10.1016/s0378-5173(00)00423-3.
[86] T.J. Kamerzell, R. Esfandiary, S.B. Joshi, C.R. Middaugh, D.B. Volkin, Protein-excipient interactions: mechanisms and biophysical characterization applied to protein formulation development, Adv. Drug Deliv. Rev. 63 (2011) 1118–59. https://doi.org/10.1016/j.addr.2011.07.006.
[87] M.R.C. Marques, R. Loebenberg, M. Almukainzi, Simulated Biological Fluids with Possible Application in Dissolution Testing, Dissolution Technol. 18 (2011) 15–28. https://doi.org/10.14227/DT180311P15.
[88] G.R. Craven, E. Steers Jr., C.B. Anfinsen, Purification, Composition, and Molecular Weight of the β-Galactosidase of Escherichia coli K12, J. Biol. Chem. 240 (1965) 2468–77. http://www.ncbi.nlm.nih.gov/pubmed/14304855.
[89] A.N. Courtney, P.N. Nehete, B.P. Nehete, P. Thapa, D. Zhou, K.J. Sastry, Alpha-galactosylceramide is an effective mucosal adjuvant for repeated intranasal or oral delivery of HIV peptide antigens, Vaccine. 27 (2009) 3335–41. https://doi.org/10.1016/j.vaccine.2009.01.083.
[90] A.N. Courtney, P. Thapa, S. Singh, A.M. Wishahy, D. Zhou, J. Sastry, Intranasal but not intravenous delivery of the adjuvant α-galactosylceramide permits repeated stimulation of natural killer T cells in the lung, Eur. J. Immunol. 41 (2011) 3312–3322. https://doi.org/10.1002/eji.201041359.
[91] N. Cuburu, M.-N. Kweon, J.-H. Song, C. Hervouet, C. Luci, J.-B. Sun, P. Hofman, J. Holmgren, F. Anjuère, C. Czerkinsky, Sublingual immunization induces broad-based systemic and mucosal immune responses in mice, Vaccine. 25 (2007) 8598–610. https://doi.org/10.1016/j.vaccine.2007.09.073.
[92] S. Dash, P.N. Murthy, L. Nath, P. Chowdhury, Kinetic modeling on drug release from controlled drug delivery systems, Acta Pol. Pharm. 67 (2010) 217–23. http://www.ncbi.nlm.nih.gov/pubmed/20524422.
[93] P.W. Wertz, C.A. Squier, Cellular and molecular basis of barrier function in oral

epithelium., Crit. Rev. Ther. Drug Carrier Syst. 8 (1991) 237–69. http://www.ncbi.nlm.nih.gov/pubmed/1954652.
[94] E. Ahlfors, C. Czerkinsky, Contact sensitivity in the murine oral mucosa. I. An experimental model of delayed-type hypersensitivity reactions at mucosal surfaces, Clin. Exp. Immunol. 86 (1991) 449–56. https://doi.org/10.1111/j.1365-2249.1991.tb02952.x.
[95] A.W. Barrett, A.T. Cruchley, D.M. Williams, Oral mucosal Langerhans' cells, Crit. Rev. Oral Biol. Med. 7 (1996) 36–58. https://doi.org/10.1177/10454411960070010301.
[96] J.R. McGhee, Mucosal immune responses. An overview, Mucosal Immunol. (1999) 485–505.
[97] J.O. Morales, J.T. McConville, Manufacture and characterization of mucoadhesive buccal films, Eur. J. Pharm. Biopharm. 77 (2011) 187–99. https://doi.org/10.1016/j.ejpb.2010.11.023.
[98] A. Kaundal, P. Kumar, A. Chaudhary, A review on mucoadhesive buccal tablets prepared using natural and synthetic polymers, World J. Pharm. Pharm. Sci. 4 (2015) 475–500.
[99] V. Kumar, G.S. Banker, Chemically-Modified Cellulosic Polymers, Drug Dev. Ind. Pharm. 19 (1993) 1–31. https://doi.org/10.3109/03639049309038760.
[100] H. Li, B. Wu, C. Mu, W. Lin, Concomitant degradation in periodate oxidation of carboxymethyl cellulose, Carbohydr. Polym. 84 (2011) 881–886. https://doi.org/10.1016/j.carbpol.2010.12.026.
[101] L. Xiquan, Q. Tingzhu, Q. Shaoqui, Kinetics of the carboxymethylation of cellulose in the isopropyl alcohol system, Acta Polym. 41 (1990) 200–222. https://doi.org/10.1002/actp.1990.010410406.
[102] C. Valenta, The use of mucoadhesive polymers in vaginal delivery, Adv. Drug Deliv. Rev. 57 (2005) 1692–712. https://doi.org/10.1016/j.addr.2005.07.004.
[103] A. Ludwig, The use of mucoadhesive polymers in ocular drug delivery, Adv. Drug Deliv. Rev. 57 (2005) 1595–639. https://doi.org/10.1016/j.addr.2005.07.005.
[104] V. Grabovac, D. Guggi, A. Bernkop-Schnürch, Comparison of the mucoadhesive properties of various polymers, Adv. Drug Deliv. Rev. 57 (2005) 1713–23. https://doi.org/10.1016/j.addr.2005.07.006.
[105] B. Campbell, Biochemical and Functional Aspects of Mucus and Mucin-Type Glycoproteins, in: E. Mathiowitz, D.E. Chickering III, C.-M. Lehr (Eds.), Bioadhesive Drug Deliv. Syst. Fundam. Nov. Approaches, Dev., CRC Press, Boca Raton, FL, 1999: pp. 85–130. https://doi.org/10.1201/b14099-6.
[106] Wee, Gombotz, Protein release from alginate matrices, Adv. Drug Deliv. Rev. 31 (1998) 267–285. https://doi.org/10.1016/s0169-409x(97)00124-5.
[107] Helmiyati, M. Aprilliza, Characterization and properties of sodium alginate from brown algae used as an ecofriendly superabsorbent, IOP Conf. Ser. Mater. Sci. Eng. 188 (2017) 012019. https://doi.org/10.1088/1757-899X/188/1/012019.
[108] S. Galus, A. Lenart, Development and characterization of composite edible films based on sodium alginate and pectin, J. Food Eng. 115 (2013) 459–465. https://doi.org/10.1016/j.jfoodeng.2012.03.006.
[109] M.A. Ghalia, Y. Dahman, Advanced nanobiomaterials in tissue engineering: synthesis, properties, and applications, in: Nanobiomaterials Soft Tissue Eng.,

Elsevier, 2016: pp. 141–172. https://doi.org/10.1016/B978-0-323-42865-1.00006-4.
[110] P.J. Mills, Film formation, in: Struct. Prop. Oriented Polym., Springer Netherlands, Dordrecht, 1997: pp. 423–446. https://doi.org/10.1007/978-94-011-5844-2_9.
[111] T. Goswami, B.R. Jasti, X. Li, Estimation of the theoretical pore sizes of the porcine oral mucosa for permeation of hydrophilic permeants, Arch. Oral Biol. 54 (2009) 577–82. https://doi.org/10.1016/j.archoralbio.2009.03.001.
[112] J.W. Anderegg, W.W. Beeman, S. Shulman, P. Kaesberg, An Investigation of the Size, Shape and Hydration of Serum Albumin by Small-angle X-Ray Scattering, J. Am. Chem. Soc. 77 (1955) 2927–2937. https://doi.org/10.1021/ja01616a002.
[113] M. Guttman, K.K. Lee, A functional interaction between gp41 and gp120 is observed for monomeric but not oligomeric, uncleaved HIV-1 Env gp140, J. Virol. 87 (2013) 11462–75. https://doi.org/10.1128/JVI.01681-13.
[114] J.F. Carpenter, M.J. Pikal, B.S. Chang, T.W. Randolph, Rational design of stable lyophilized protein formulations: some practical advice, Pharm. Res. 14 (1997) 969–75. https://doi.org/10.1023/a:1012180707283.
[115] S.L. Ginn, I.E. Alexander, M.L. Edelstein, M.R. Abedi, J. Wixon, Gene therapy clinical trials worldwide to 2012 - an update, J. Gene Med. 15 (2013) 65–77. https://doi.org/10.1002/jgm.2698.
[116] C.E. Thomas, A. Ehrhardt, M.A. Kay, Progress and problems with the use of viral vectors for gene therapy, Nat. Rev. Genet. 4 (2003) 346–358. https://doi.org/10.1038/nrg1066.
[117] N. Clément, J.C. Grieger, Manufacturing of recombinant adeno-associated viral vectors for clinical trials, Mol. Ther. - Methods Clin. Dev. 3 (2016) 16002. https://doi.org/10.1038/mtm.2016.2.
[118] M.S. Al-Dosari, X. Gao, Nonviral Gene Delivery: Principle, Limitations, and Recent Progress, AAPS J. 11 (2009) 671. https://doi.org/10.1208/s12248-009-9143-y.
[119] C.-W. Chang, D. Choi, W.J. Kim, J.W. Yockman, L. V. Christensen, Y.-H. Kim, S.W. Kim, Non-ionic amphiphilic biodegradable PEG–PLGA–PEG copolymer enhances gene delivery efficiency in rat skeletal muscle, J. Control. Release. 118 (2007) 245–253. https://doi.org/10.1016/j.jconrel.2006.11.025.
[120] R.J. Mumper, J. Wang, S. L. Klakamp, H. Nitta, K. Anwer, F. Tagliaferri, A.P. Rolland, Protective interactive noncondensing (PINC) polymers for enhanced plasmid distribution and expression in rat skeletal muscle, J. Control. Release. 52 (1998) 191–203. https://doi.org/10.1016/S0168-3659(97)00215-0.
[121] J.P. Behr, The proton sponge: A trick to enter cells the viruses did not exploit, in: Chimia (Aarau)., 1997.
[122] T. Mosmann, Rapid colorimetric assay for cellular growth and survival: Application to proliferation and cytotoxicity assays, J. Immunol. Methods. 65 (1983) 55–63. https://doi.org/10.1016/0022-1759(83)90303-4.
[123] M.-H. Alves, B.E.B. Jensen, A.A.A. Smith, A.N. Zelikin, Poly(Vinyl Alcohol) Physical Hydrogels: New Vista on a Long Serving Biomaterial, Macromol. Biosci. 11 (2011) 1293–1313. https://doi.org/10.1002/mabi.201100145.
[124] D. Fischer, Y. Li, B. Ahlemeyer, J. Krieglstein, T. Kissel, In vitro cytotoxicity

testing of polycations: influence of polymer structure on cell viability and hemolysis., Biomaterials. 24 (2003) 1121–31. https://doi.org/10.1016/s0142-9612(02)00445-3.
[125] F. Bray, J. Ferlay, I. Soerjomataram, R.L. Siegel, L.A. Torre, A. Jemal, Global cancer statistics 2018: GLOBOCAN estimates of incidence and mortality worldwide for 36 cancers in 185 countries, CA. Cancer J. Clin. (2018). https://doi.org/10.3322/caac.21492.
[126] C.F. Thorn, C. Oshiro, S. Marsh, T. Hernandez-Boussard, H. McLeod, T.E. Klein, R.B. Altman, Doxorubicin pathways: Pharmacodynamics and adverse effects, Pharmacogenet. Genomics. (2011). https://doi.org/10.1097/FPC.0b013e32833ffb56.
[127] K. Tewey, T. Rowe, L. Yang, B. Halligan, L. Liu, Adriamycin-induced DNA damage mediated by mammalian DNA topoisomerase II, Science (80-.). 226 (1984) 466–468. https://doi.org/10.1126/science.6093249.
[128] M. Cagel, E. Grotz, E. Bernabeu, M.A. Moretton, D.A. Chiappetta, Doxorubicin: nanotechnological overviews from bench to bedside, Drug Discov. Today. 22 (2017) 270–281. https://doi.org/10.1016/j.drudis.2016.11.005.
[129] S.A. Johnstone, K. Gelmon, L.D. Mayer, R.E. Hancock, M.B. Bally, In vitro characterization of the anticancer activity of membrane-active cationic peptides. I. Peptide-mediated cytotoxicity and peptide-enhanced cytotoxic activity of doxorubicin against wild-type and p-glycoprotein over-expressing tumor cell lines, Anticancer. Drug Des. 15 (2000) 151–60. http://www.ncbi.nlm.nih.gov/pubmed/10901303.
[130] L. Hui, K. Leung, H.M. Chen, The combined effects of antibacterial peptide cecropin A and anti-cancer agents on leukemia cells, Anticancer Res. (2002).
[131] K.N. Sugahara, T. Teesalu, P.P. Karmali, V.R. Kotamraju, L. Agemy, D.R. Greenwald, E. Ruoslahti, Coadministration of a Tumor-Penetrating Peptide Enhances the Efficacy of Cancer Drugs, Science (80-.). 328 (2010) 1031–1035. https://doi.org/10.1126/science.1183057.
[132] J. Zhao, Y. Huang, D. Liu, Y. Chen, Two hits are better than one: Synergistic anticancer activity of α-helical peptides and doxorubicin/epirubicin, Oncotarget. (2015). https://doi.org/10.18632/oncotarget.2754.
[133] H. Takahashi, K. Yumoto, K. Yasuhara, E.T. Nadres, Y. Kikuchi, L. Buttitta, R.S. Taichman, K. Kuroda, Anticancer polymers designed for killing dormant prostate cancer cells, Sci. Rep. 9 (2019) 1096. https://doi.org/10.1038/s41598-018-36608-5.
[134] J. Cao, C. Wang, L. Guo, Z. Xiao, K. Liu, H. Yan, Co-administration of a charge-conversional dendrimer enhances antitumor efficacy of conventional chemotherapy, Eur. J. Pharm. Biopharm. 127 (2018) 371–377. https://doi.org/10.1016/j.ejpb.2018.02.035.
[135] T.-C. Chou, Theoretical Basis, Experimental Design, and Computerized Simulation of Synergism and Antagonism in Drug Combination Studies, Pharmacol. Rev. 58 (2006) 621–681. https://doi.org/10.1124/pr.58.3.10.
[136] C. Zhu, S. Jung, G. Si, R.U. Cheng, F. Meng, X. Zhu, T.G. Park, Z. Zhong, Cationic methacrylate copolymers containing primary and tertiary amino side groups: Controlled synthesis via RAFT polymerization, DNA condensation, and in vitro gene transfection, J. Polym. Sci. Part A Polym. Chem. (2010).

https://doi.org/10.1002/pola.24064.
[137] W. Ji, D. Panus, R.N. Palumbo, R. Tang, C. Wang, Poly(2-aminoethyl methacrylate) with Well-Defined Chain Length for DNA Vaccine Delivery to Dendritic Cells, Biomacromolecules. 12 (2011) 4373–4385. https://doi.org/10.1021/bm201360v.
[138] W. Ji, Synthetic polymers with well-defined structures for DNA vaccine delivery and cancer therapy, University of Minnesota, 2013.
[139] J. Friedrich, C. Seidel, R. Ebner, L.A. Kunz-Schughart, Spheroid-based drug screen: considerations and practical approach, Nat. Protoc. 4 (2009) 309–324. https://doi.org/10.1038/nprot.2008.226.
[140] D.J. Arndt-Jovin, T.M. Jovin, Chapter 16 Fluorescence Labeling and Microscopy of DNA, in: Methods Cell Biol., 1989: pp. 417–448. https://doi.org/10.1016/S0091-679X(08)60989-9.
[141] I. Padmalayam, M.J. Suto, 3D Cell Cultures. Mimicking In Vivo Tissues for Improved Predictability in Drug Discovery, in: Annu. Rep. Med. Chem., 2012. https://doi.org/10.1016/B978-0-12-396492-2.00024-2.
[142] J. Gehl, Electroporation: theory and methods, perspectives for drug delivery, gene therapy and research, Acta Physiol. Scand. 177 (2003) 437–447. https://doi.org/10.1046/j.1365-201X.2003.01093.x.
[143] R. V. Davalos, L.M. Mir, B. Rubinsky, Tissue Ablation with Irreversible Electroporation, Ann. Biomed. Eng. 33 (2005) 223–231. https://doi.org/10.1007/s10439-005-8981-8.
[144] J. Hu, H. Albadawi, B.W. Chong, A.R. Deipolyi, R.A. Sheth, A. Khademhosseini, R. Oklu, Advances in Biomaterials and Technologies for Vascular Embolization, Adv. Mater. 31 (2019) e1901071. https://doi.org/10.1002/adma.201901071.
[145] Q. Shao, F. Liu, C. Chung, K. Elahi-Gedwillo, P.P. Provenzano, B. Forsyth, J.C. Bischof, Physical and Chemical Enhancement of and Adaptive Resistance to Irreversible Electroporation of Pancreatic Cancer, Ann. Biomed. Eng. 46 (2018) 25–36. https://doi.org/10.1007/s10439-017-1932-3.
[146] G.C. Troiano, L. Tung, V. Sharma, K.J. Stebe, The reduction in electroporation voltages by the addition of a surfactant to planar lipid bilayers, Biophys. J. 75 (1998) 880–8. https://doi.org/10.1016/S0006-3495(98)77576-9.
[147] E.J. Aiken, B.G. Kilberg, S. Yu, S.C. Hagness, J.H. Booske, Ionomycin-Induced Changes in Membrane Potential Alter Electroporation Outcomes in HL-60 Cells, Biophys. J. 114 (2018) 2875–2886. https://doi.org/10.1016/j.bpj.2018.05.018.
[148] H.B. Kim, S. Lee, J.H. Chung, S.N. Kim, C.K. Sung, K.Y. Baik, Effects of Actin Cytoskeleton Disruption on Electroporation In Vitro, Appl. Biochem. Biotechnol. 191 (2020) 1545–1561. https://doi.org/10.1007/s12010-020-03271-4.
[149] S. Šatkauskas, B. Jakštys, P. Ruzgys, M. Jakutavičiūtė, Different Cell Viability Assays Following Electroporation In Vitro, in: Handb. Electroporation, Springer International Publishing, Cham, 2017: pp. 1411–1424. https://doi.org/10.1007/978-3-319-32886-7_140.
[150] M.P. Rols, J. Teissié, Electropermeabilization of mammalian cells. Quantitative analysis of the phenomenon, Biophys. J. 58 (1990) 1089–1098. https://doi.org/10.1016/S0006-3495(90)82451-6.
[151] Y. Guo, Y. Zhang, N. Jin, R. Klein, J. Nicolai, R.J. Lewandowski, R.K. Ryu, R.A.

Omary, A.C. Larson, Electroporation-mediated transcatheter arterial chemoembolization in the rabbit VX2 liver tumor model, Invest. Radiol. 47 (2012) 116–20. https://doi.org/10.1097/RLI.0b013e31822e57cc.
[152] D. Vollherbst, R.C. Bertheau, S. Fritz, C. Mogler, H.-U. Kauczor, E. Ryschich, B.A. Radeleff, P.L. Pereira, C.M. Sommer, Electrochemical Effects after Transarterial Chemoembolization in Combination with Percutaneous Irreversible Electroporation: Observations in an Acute Porcine Liver Model, J. Vasc. Interv. Radiol. 27 (2016) 913-921.e2. https://doi.org/10.1016/j.jvir.2016.02.001.
[153] P. Isfort, P. Rauen, H.-S. Na, N. Ito, S. von Stillfried, C. Kuhl, P. Bruners, Does Drug-Eluting Bead TACE Enhance the Local Effect of IRE? Imaging and Histopathological Evaluation in a Porcine Model., Cardiovasc. Intervent. Radiol. 42 (2019) 880–885. https://doi.org/10.1007/s00270-019-02181-1.
[154] P. Chan, C. McLean, S. Chan, G.S. Goh, The interaction between irreversible electroporation therapy (IRE) and embolization material using a validated vegetal model: an experimental study, Diagn. Interv. Radiol. 25 (2019) 304–309. https://doi.org/10.5152/dir.2019.18361.
[155] M.A. Lazzaro, A. Badruddin, O.O. Zaidat, Z. Darkhabani, D.J. Pandya, J.R. Lynch, Endovascular Embolization of Head and Neck Tumors, Front. Neurol. 2 (2011). https://doi.org/10.3389/fneur.2011.00064.
[156] R.L. Stout, Solvents in Today's Coatings, in: Appl. Polym. Sci. 21st Century, Elsevier, 2000: pp. 527–543. https://doi.org/10.1016/B978-008043417-9/50030-1.
[157] C.-S. Kim, D.M. Saylor, M.K. McDermott, D. V. Patwardhan, J.A. Warren, Modeling solvent evaporation during the manufacture of controlled drug-release coatings and the impact on release kinetics, J. Biomed. Mater. Res. Part B Appl. Biomater. 90B (2009) 688–699. https://doi.org/10.1002/jbm.b.31336.
[158] J. Zhao, X. Wen, L. Tian, T. Li, C. Xu, X. Wen, M.P. Melancon, S. Gupta, B. Shen, W. Peng, C. Li, Irreversible electroporation reverses resistance to immune checkpoint blockade in pancreatic cancer., Nat. Commun. 10 (2019) 899. https://doi.org/10.1038/s41467-019-08782-1.
[159] V.M. Ringel-Scaia, N. Beitel-White, M.F. Lorenzo, R.M. Brock, K.E. Huie, S. Coutermarsh-Ott, K. Eden, D.K. McDaniel, S.S. Verbridge, J.H. Rossmeisl, K.J. Oestreich, R. V. Davalos, I.C. Allen, High-frequency irreversible electroporation is an effective tumor ablation strategy that induces immunologic cell death and promotes systemic anti-tumor immunity, EBioMedicine. 44 (2019) 112–125. https://doi.org/10.1016/j.ebiom.2019.05.036.
[160] I. Vivas, K. Iribarren, T. Lozano, D. Cano, A. Lasarte-Cia, S. Chocarro, M. Gorraiz, P. Sarobe, S. Hervás-Stubbs, J.I. Bilbao, N. Casares, J.J. Lasarte, Therapeutic Effect of Irreversible Electroporation in Combination with Poly-ICLC Adjuvant in Preclinical Models of Hepatocellular Carcinoma, J. Vasc. Interv. Radiol. 30 (2019) 1098–1105. https://doi.org/10.1016/j.jvir.2019.02.023.
[161] Q. Shao, S. O'Flanagan, T. Lam, P. Roy, F. Pelaez, B.J. Burbach, S.M. Azarin, Y. Shimizu, J.C. Bischof, Engineering T cell response to cancer antigens by choice of focal therapeutic conditions, Int. J. Hyperthermia. 36 (2019) 130–138. https://doi.org/10.1080/02656736.2018.1539253.
[162] L. Zhang, Z. Zhang, W. Wang, A. Tabet, S. Hanson, L. Zhang, D. Zhu, C. Wang, Polymer-based dual-responsive self-emulsifying nano-droplets as potential carriers

for poorly soluble drugs (In revision), (2020).
[163] J.F.S. Mann, P.F. McKay, S. Arokiasamy, R.K. Patel, J.S. Tregoning, R.J. Shattock, Mucosal application of gp140 encoding DNA polyplexes to different tissues results in altered immunological outcomes in mice, PLoS One. 8 (2013) e67412.
[164] J.C. Kasper, D. Schaffert, M. Ogris, E. Wagner, W. Friess, Development of a lyophilized plasmid/LPEI polyplex formulation with long-term stability-A step closer from promising technology to application, J. Control. Release. (2011). https://doi.org/10.1016/j.jconrel.2011.01.003.
[165] P. Vandenabeele, K. Vandecasteele, C. Bachert, O. Krysko, D. V. Krysko, Immunogenic Apoptotic Cell Death and Anticancer Immunity., Adv. Exp. Med. Biol. 930 (2016) 133–49. https://doi.org/10.1007/978-3-319-39406-0_6.
[166] L. Novik, Cellular Mechanism of a Synthetic Oncolytic Polymer, University of Minnesota, 2020.